# INTERFEROMETRIC OBSERVATIONS OF PLANETARY NEBULAE

by

Paul David Atherton

Astronomy Group
Blackett Laboratory
Imperial College
London SW7 2BZ

Submitted to the University of London
for the degree of Doctor of Philosophy

1 9 7 8

## ABSTRACT

Studies of the velocity field of planetary nebulae can be used to derive important information concerning their structure and dynamics.

A description is given of the design, construction and operation of a servo-controlled Fabry Perot Interferometer, for the Cassegrain focus, which was built to perform these studies. New evidence is presented concerning the structure and internal motions of NGC 3242, NGC 6720 and NGC 7027.

A technique is described which uses the velocity field to map variations in the electron temperature and density along the line of sight as well as across the face of the nebula. It is shown how a Fabry Perot may be used in conjunction with multi-element array detectors to facilitate this technique.

Finally some extensions to the technique of capacitance micrometry are discussed which allow the operation of a single air-spaced etalon over a wide range of capacitor gaps.

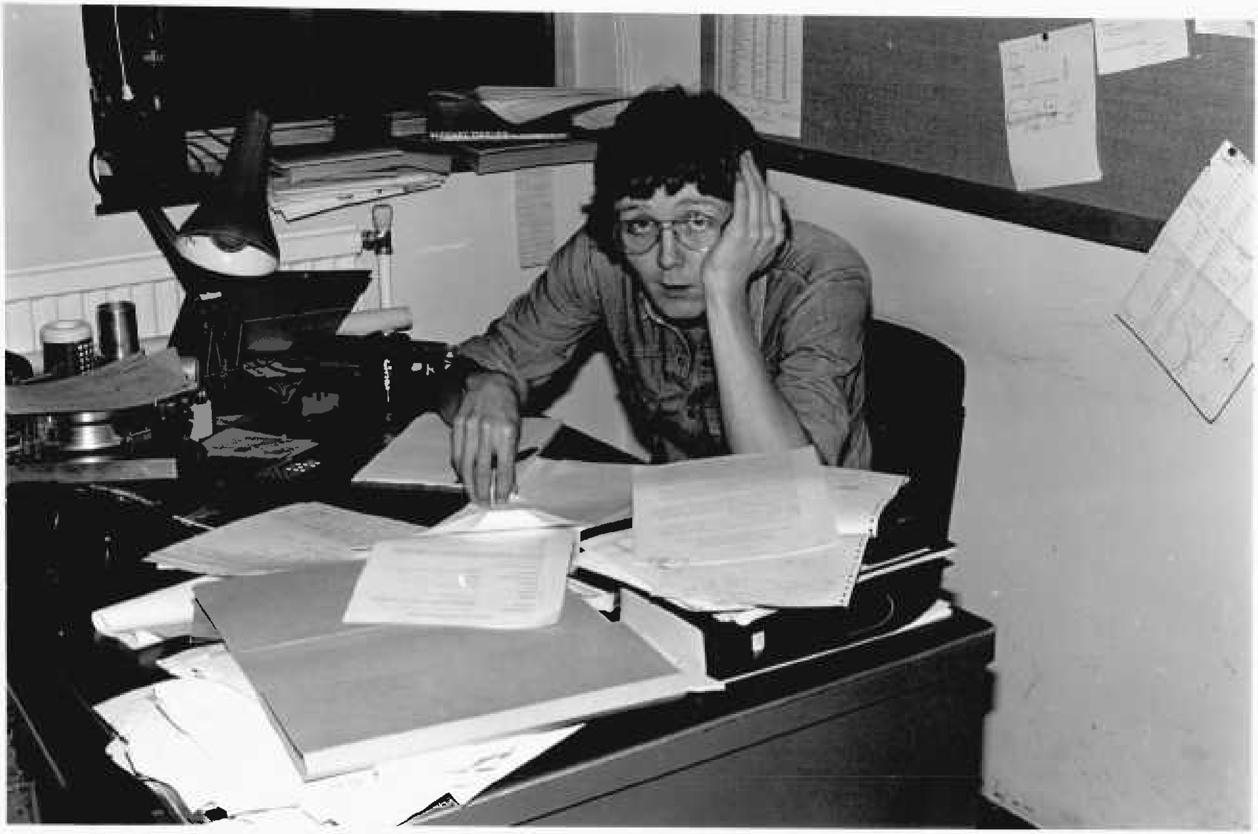

## PREFACE

During the past three and a half years, I have been responsible for the design and construction of a servo-controlled Fabry Perot Interferometer for use at the Cassegrain focus, and for the reduction and interpretation of the data obtained with it.

The observational work has been concerned with an investigation of the dynamics of planetary nebulae using the Doppler shift of the spectral lines to map out variations in the radial velocity.

I am indebted to Dr. T.R. Hicks for the design of the servo-electronics and for instilling in me some of the finer points of capacitance micrometry and servo-control systems. I would like to thank Dr. N.K. Reay for his active help, encouragement and guidance, and Professor J. Ring for his constant support of this project.

I would like to thank Mr. M. Wells and Dr. S.P. Worswick for some stimulating and interesting discussions concerning the subtleties of Fabry Perots and planetary nebulae, for their help on various observing trips, and for the computer programs for the Interdata 70 and numerous electronographs respectively. I am especially grateful to Mr Roy Barr

and Mr Jack Crabtree for their excellent advice on mechanical design and for the professional manner of the construction. I would like to thank my parents whose constant help and guidance have assisted me throughout my studies.

Finally I would like to dedicate this thesis to my wife, Cathy, for her support and encouragement over the past three and a half years.

# INTERFEROMETRIC OBSERVATIONS OF PLANETARY NEBULAE

## CONTENTS

page

## CHAPTER 1: The Characteristics of Planetary Nebulae Spectral, Structural and Dynamical Considerations

/..

contents (contd..) page

CHAPTER 2: Instrumentation: Instrument Design and Construction

/..

contents (Chapter 2) contd.. page

CHAPTER 3: Data Acquisition and Reduction

/..

contents (contd..) page

## CHAPTER 4: Astronomical Observations

## CHAPTER 5: The Use of a Fabry Perot Interferometer with Multi-Point Detectors

/..

contents (Chapter 5) contd.. page

CHAPTER 6: Further Developments

APPENDIX: Modelling of the Nebular Envelope

## ILLUSTRATIONS

/..

Illustrations (contd..)

# CHAPTER 1: THE CHARACTERISTICS OF PLANETARY NEBULAE: SPECTRAL, STRUCTURAL AND DYNAMIC CONSIDERATIONS

In this chapter, the salient characteristics of planetary nebulae are discussed. It is shown how an investigation of the spatial variation of the spectral line profiles emitted from these objects can supply valuable information concerning their morphology and dynamics and also provide relative temperature and density measurements.

## 1.1 Introduction

In general, planetary nebulae are low surface brightness, extended objects, ranging in apparent size from about 12 arc minutes diameter down to unresolved 'stellar' like nebulae. They are thought to evolve from giant stars which eject an envelope of gas. The star then contracts and its temperature increases to $\sim 10^5$ °K. At this stage, the star emits mainly hard U-V photons which ionize the surrounding gas creating a Strömgren sphere. The lifetime of the nebula is thought to be around $5 \times 10^4$ years, after which the central star evolves into a white dwarf and the gaseous envelope returns to the inter-stellar medium.

Because planetaries are relatively faint, their study demands the use of large telescopes and efficient instrumentation. Visually, they have a greenish appearance due to two [OIII] green lines at $\lambda$5007A° and $\lambda$4959A° which were initially attributed to the hypothetical element 'Nebulium'. These lines were first identified as the forbidden lines of doubly-ionized oxygen by Bowen (1927, 1928) since when they have been studied in detail by many observers, largely because of their brightness and their comparatively small amount of thermal broadening.

## 1.2 Formation

Statistical arguments have been advanced to demonstrate that a large fraction of stars with masses comparable to that of the sun become planetary nebulae (Miller, 1974).

The central stars, believed to be incipient white dwarfs, are hydrogen deficient and it seems likely that they are burning Helium or Carbon in the core. It also seems probable that the ejection of the shell surrounding the star takes place before the central stars evolve into their highly luminous, compact state, as the observed expansion velocity ($\sim$20 km sec$^{-1}$) is low compared to the escape velocity (1000 km sec$^{-1}$) of these stars.

Menzel (1946) was the first to suggest that planetaries are closely connected with cool red giants, supergiants and long period variables, which have degenerate cores surrounded by extensive and tenuous gaseous envelopes. This idea of red giants as possible progenitors of planetaries was strengthened when dust was found in some planetary envelopes (Gillett et al 1967), suggesting that the material in the shell originated in a cool stellar atmosphere.

Various mechanisms have been advanced whereby this envelope may be ejected from the giant star:-
Krishna Swamy and Stecher (1969) have suggested a slow mass loss due to radiation pressure on dust grains; Faulkner (1970) has shown that sufficient momentum for ejection can

be transferred to the shell by radiation pressure acting through the electron scattering opacity; Lucy (1967), Roxburgh (1967) and Pacynski and Ziolkowski (1968) have postulated a dynamical instability against pulsations. This relies on the energy stored in the Hydrogen and Helium ionization - recombination zones being sufficiently large that the total energy of the outer envelope is positive. If this energy can be converted into a motion of the outer envelope, by some means, then the pulsation amplitude may increase without limit, lifting off the entire outer envelope of the star and leaving it with a terminal velocity of around the escape velocity: 30 km $sec^{-1}$.

Rose (1968) and Smith and Rose (1972) have proposed that thermal instabilities, caused by the inability of convection to transport sufficient energy across the large dimensions of the shell, may serve to increase the amplitude of the relaxation oscillations until the envelope is completely lost. More recent work on dynamical instabilities has been undertaken by Härm and Schwarzschild (1975) and Kutter and Sparks (1974).

Thus, although the consensus of opinion seems to support red giant or Mira-like stars as progenitors, no satisfactory theory of the formation has yet been put forward. One of the more fundamental difficulties with shell ejection models of the type just described is the way in which the angular momentum of the rotating red giant is shared between the shell and the central star. As the central star collapses, conservation of angular momentum requires that it rotate faster. Any realistic division of the initial angular momentum between the ejected shell and the residual core results in the star spinning so fast it disintegrates (Melnick, 1977).

## 1.3 Emitted Spectrum

The visible spectrum of planetary nebulae is dominated by emission lines superimposed on a background continuum. The energy balance of the nebula is dictated largely by the efficiency of these processes in disposing of the energy supplied to the nebula, by degrading ultra violet photons down to wavelengths to which the nebula is effectively transparent. There are three distinct processes contributing to the emission line spectrum.

### 1.3.1 Recombination

Electrons recombine with atoms or ions to an excited level from which they cascade down to lower levels. The strength of these emission lines is heavily dependent upon the abundance of the element, and for this reason they are predominantly the lines of Hydrogen and Helium, which between them form over 99% of the mass of the nebula.

### 1.3.2 Forbidden Line Emission

Free electrons liberated by the photoionization of Hydrogen atoms, undergo inelastic collisions with various atoms and ions, exciting them to low lying metastable states.

The most important of these ions in terms of the radiative cooling of the nebula are $O^{++}$($^3P_2$-$^1D_2$, λ5007A$^o$), ($^3P_1$-$^1D_2$, λ4959A$^o$); $O^+$($^4S_{3/2}$-$^2D_{5/2}$, λ3729A$^o$), ($^4S_{3/2}$-$^2D_{3/2}$, λ3726A$^o$), $N^{++}$($^3P_2$-$^1D_2$ λ6583A$^o$), ($^3P_1$-$^1D_2$, λ6548A$^o$).

These ions make a significant contribution, despite their low relative abundances compared to H and He, because they possess energy levels with excitation potentials of the order of $k.T_e$ where $T_e$ is the electron temperature and k is Boltzmann's constant.

The metastable states have long lifetimes compared to non-metastable states and would, under normal conditions, be collisionally deactivated before any radiation could take place. However the densities found in gaseous nebulae are sufficiently low that the time between collisions may be long enough for the atom or ion to radiate. Collisional deactivation is still an important factor in the determination of the line strength and in the thermal equilibrium of the nebula, as changes in the amount of energy lost through forbidden line radiation, to which the nebula is transparent, changes the effective cooling of the nebula.

### 1.3.3 Bowen Resonance Fluorescence

This is a mechanism which changes the relative intensities of certain forbidden lines due to a near coincidence between the wavelength of the HeII Ly$\alpha$ line at 303.78 A$^o$ and the OIII at 303.80 A$^o$, the latter being the beginning of the transition scheme producing all the OIII lines.

In a nebula surrounding a high temperature star, there will be a region containing He$^{++}$ and a certain amount of residual He$^+$. Thus HeII Ly$\alpha$ lines are scattered many times before they escape, building up a high energy density in $\lambda$303.80Å . This serves to pump energy into the OIII lines due to the absorption of some of these photons by O$^{++}$ sitting at the $2p^2\ {}^3P_2$ level, exciting them to the $3d^3P_2{}^o$ level.

A similar coincidence of the $\lambda$374.436 Å line, which is one of the end products of the fluorescent cycle in OIII, with a resonance line of NIII, can lead to the initiation of a resonance-fluorescence cycle in NIII.

### 1.3.4 Continuum Emission

In addition to the discreteline emission discussed in the preceding section, planetary and diffuse nebulae exhibit a continuous emission in the optical region which arises principally from the following processes:

i) Free-bound emission of $H^+$ and $He^+$
ii) Free-free transitions of electrons in the Coulomb field of Hydrogen and Helium ions. This source of continuum dominates at infra-red and radio wavelengths.
iii) Two-photon emission (Mayer, 1931, Spitzer and Greenstein, 1951) produced by hydrogen atoms decaying from the metastable $2^2S_{1/2}$ level via a virtual P-state. This may become important under low density conditions. The two emitted photons may have any frequency subject to the condition:

$$E_1 + E_2 = E(2s - 1s) \qquad (1.1)$$

Under high density conditions collisional de-excitation of the 2s level renders this process insignificant.

The energy emitted isotropically in a time dt from a volume element dV, in the frequency interval of $\nu$, in these continua, is given by Brown and Matthews (1970):

$$E = N_e N_p \delta \, d\nu \, dt \, dV \qquad (1.2)$$

where $\delta$ is the emission coefficient
$N_p$ is the proton number density
$N_e$ is the electron number density

The emission coefficient $\delta_n(\nu)$ for continuous emission at a frequency $\nu$ due to the recombinations to the $n^{th}$ excited state of $H^o$ (or $He^+$) is

$$\delta_n(\nu) = \left[ \left(\frac{2}{\Pi}\right)^{\frac{1}{2}} \frac{\exp(I_n/kT)}{c^2 (mhT)^{3/2}} \right] Z_n{}^2 h (h\nu)^3 a_n(\nu) \exp(-h\nu/_{kT}) \tag{1.3}$$

where $T$ is the electron temperature
$I_n$ is the ionization potential for the $n^{th}$ state
$a_n(\nu)$ is the photoionization cross section for this state.

and $\dfrac{I_n = Z^2 I_H}{n^2}$ where $Z$ is the atomic number
where $I_H$ is the Rydberg energy

$a_n(\nu)$ has been evaluated by Seaton (1960) and later with more accuracy by Burgess (1964).

In addition to the recombination continuum radiation a Maxwellian distribution of electrons encountering $H^+$, $He^+$ or $He^{++}$ ions will emit a bremsstrahlung emission spectrum with a continuous emission coefficient given by:

$$\delta_b(\nu) = \frac{2^5 Z^2 e^4 h}{3m^2 c^3} \left(\frac{\Pi I_H}{3kT}\right)^{\frac{1}{2}} \exp(-h\nu/kT) <gIII> (T,Z,\nu) \qquad (1.4)$$

Where $<gIII>$ is an expansion of the mean free-free Gaunt factor (Seaton, 1960).

### 1.3.5 Dust Emission

A further source of continuum radiation, particularly in the infra-red, is thought to arise from dust particles heated by absorption of stellar radiation, Lyman continuum and nebular resonance line radiation.

Krishna Swamy and O'Dell (1968) have estimated the dust particles in NGC 7027 to have a temperature of $\sim 200^{\circ}$K from the excess IR continuum.

## 1.4 Morphology

The term 'planetary nebula' describes a group of objects of an extremely diverse nature. The variety of observed forms has led various workers to attempt to classify them.

Wright (1918) proposed their classification on the basis of the observed spectrum; Thackeray and Evans (1950) proposed a scheme based on the apparent symmetry of the objects; Vorontzov-Velyaminov (1934) put forward a system based on their division into elliptical, ring, bipolar or peculiar nebulae. This scheme was extended by Westerland and Henize (1967) who divided some of the classes into further sub-groups. Hromov (1962) has argued that all planetaries have the same form: essentially a high-density torus forming the equator of a spherical or spheroidal shell of lower density. On this basis Hromov and Kohoutek (1968) devised a scheme in which the classification is dependent on the degree of deviation of the main structure from this regular, ring-like shape. This scheme has the disadvantage that two objects with the same classification do not necessarily look alike.

Weedman (1968) has argued that most planetaries are prolate spheroids of axial ratio (ie Major axis/ Minor axis) 1.5. In some cases it is by no means clear that the apparent form can be accounted for by the proposed formation mechanism: Scott (1973) has interpreted the radio structure of NGC 7027 as a cylinder, whilst Münch (1968) has shown that it is possible to interpret NGC6543 in terms of a spiral. However the appearance of these nebulae varies considerably depending upon the observed emission line due to the differing levels of ionization through the nebula.

### 1.4.1 Ionization Structure

The ionization of a region of gas surrounding a hot star was first treated by Strömgren (1939) who computed the ionization of a mass of hydrogen of uniform density exposed to dilute, high temperature radiation. The results of these computations showed that in the immediate vicinity of a hot star the hydrogen is completely ionized and remains so for a distance from the star determined by both the density of the gas and the amount of ionizing radiation present. The transition region between the HII and HI region is very narrow, the ionization decreasing sharply in a distance comparable to the mean free path of an ionizing photon. For a density $N_H = 10^3$ atoms $^{-3}$ this distance is $\sim 10^{-3}$ parsecs which compares with a typical nebular diameter of 0.1 parsecs.

### 1.4.2 Central Stars

Clearly the ionization structure is strongly dependent on the characteristics of the exciting star. The study of the central stars is hampered by the surrounding nebulosity as the nebular H and He lines tend to fill in the cores of the stellar absorption lines.

Generally, they are found to be O-type stars with either emission and/or absorption features, continuous spectra, Wolf Rayet type spectra or a high excitation type spectra characterized by a strong blue continuum with weak H, ionized He and O VI features. Wolf-Rayet type stars have broad emission lines which have been interpreted as arising from material flowing outwards from the star. This would be consistent with a star which is still losing mass to the nebular envelope.

The central star temperatures are usually between $4.10^4$ °K and $10^5$ °K and they have a radius $R_*$ between $R_\odot$ and $10^{-2}$ $R_\odot$.

O'Dell (1962) has noted a correlation between the size of the nebular shell and the Zanstra temperature and hence the radius of the exciting star. Large nebular shells seem to be associated with high temperature and thus small radius stars. This would seem to indicate that after the ejection of the envelope the star gradually contracts and increases in temperature, resulting in a massive increase in U-V emission. Thus well-evolved nebulae will have large shells and very small hot central stars.

### 1.4.3 Stratification

Monochromatic images of planetaries in the lines of different ions indicate a relationship between the size of the image and the ionization potential of the emitting ion (Bowen, 1928; Wilson, 1950). This phenomenon, known as the 'stratification' of the radiation, is a function of the energy distribution of the photons emitted by the exciting star.

In the central regions of the nebula, ions are found in high states of ionization: HeII, OIV, OV, NeV etc. Outside these central regions only the 'softer' less energetic radiation passes through and species with lower ionization potentials are found e.g. OIII, HeI, HII whilst in the extreme outer regions, where the ionizing radiation is very soft , the low excitation lines of OII, OI, NII are found.

Thus the study of the light emanating from an ion of a particular ionization potential allows the investigation of a particular region of the ionized nebula.

### 1.4.4 Dynamics

A correlation between the monochromatic image size and the corresponding spectral line splitting was first recognized by Wilson (1950) from slitless spectograph data.

This was developed further by Weedman (1968) who found strong evidence for velocity gradients through the shells of a number of planetaries. These velocity variations were of the general form:

$$V = kR + C \tag{1.5}$$

Where V is the velocity

R is the distance from the centre of the nebula

k is a constant

C is a constant

Theoretical models (Mathews, 1966 ; Hunter and Sofia 1971; Finzi and Wolf 1970) indicate that the velocity gradient is established as the shell evolves and the material is redistributed by thermal and radiative forces.

Weedman (1968) found that in the case of several planetaries the velocity gradient extrapolated to zero at a point in the nebula between the shell and the central star. This was interpreted as showing that the mechanism responsible for imparting momentum to the shell did so over a period of time significant to the age of the nebula, modifying the relative expansion velocities. The shape of the shell is thought to describe the initial directional distribution of momentum.

This dynamical picture presents a powerful diagnostic tool, enabling the investigation not only of the innermost regions, but also of the far side of the nebula as well, by observing the Doppler shifted profile, arising from that region, of a line in which the nebula is optically thin. It may even be possible to assess, roughly, the amounts of dust that may be present in the nebula, by comparing the relative heights of red and blue shifted spectral components.

### 1.4.5 Discussion

Clearly, the morphology of planetary nebulae is not well understood. Its investigation has, hitherto, been conducted using electronographic or photographic detectors with narrow-band interference filters to isolate the particular spectral line of interest. However, the intensity at any point in the image corresponds to the sum of the intensities emitted along the line of sight. Effectively, these techniques present a 'static' picture of the nebula.

The velocity field, however, has important implications concerning the origin and development of the nebular envelope. The directional variation in the initial ejection velocity, and hence momentum, is reflected in the shape of the nebular shell, and thus deductions can be made, from data on the velocity field, which allows the investigation of the shell in three dimensions. Using these data, it is possible to distinguish between the various structures proposed for nebulae - prolate or oblate spheriods, cylinders, barrels, toroids, spirals etc - to calculate the angle of any axis of symmetry to the line of sight, and , in conjunction with electronographic data, to build three dimensional structural and dynamical models. It is the purpose of this thesis to indicate the optimum manner in which this may be accomplished.

## 1.5 The Velocity Field

The change in wavelength of a spectral line, due to a relative motion between the source and the observer, compared to the case where the relative velocity is zero, is given by the well known relativistic Doppler effect:

$$\lambda^1 = \frac{\lambda\sqrt{1-v^2/c^2}}{1-v/c} \qquad (1.6)$$

Typically, in planetary nebulae, expansion velocities are less than 100 km $\sec^{-1}$. Thus $^{v^2}/_{c^2} \sim 10^{-7}$ which allows the approximation:

$$\lambda^1 = \frac{\lambda}{1-v/c} \qquad (1.7)$$

which leads to:

$$\Delta\lambda = \lambda\frac{v}{c} \qquad (1.8)$$

High resolution studies of planetary nebulae have shown that in many cases the spectral line profiles are split into two components (Wilson, 1950; Campbell and Moore, 1918).

The magnitude of this line splitting can vary quite drastically across the nebula, as do the relative heights and halfwidths of the components (Weedman, 1968). This has led to the idea that planetaries are shells of gas in radial expansion from the central star, the spectral lines being split due to the different relative velocities of the front and back surfaces of the nebular shell relative to the observer.

This hypothesis has been partially confirmed by proper motion measurements (Liller et al, 1966; Liller and Liller, 1968) made using long focal length telescopes and baselines of several years.

## 1.6 Information from Optical Spectra

A great deal of further information concerning the conditions prevailing in planetary nebulae can be gathered from a careful study of the emitted spectrum. The following techniques for the determination of temperature and density have important implications as it is possible to use the velocity field to map out three dimensional variations in these parameters.

The density and temperature ratio mapping techniques developed by Reay and Worswick (1978), and the extension of them, using velocity field information, to allow three dimensional information to be built up, will be discussed further in Chapter 5. Meanwhile, it will suffice to show the general methods employed to calculate temperatures and densities in planetary nebulae.

### 1.6.1 Temperature Measurements

#### a) From Emission Lines

If an ion has an energy level structure such that two different upper levels have different excitation energies, and both levels are responsible for emission lines, then the relative strengths of these emission lines will depend upon the energy distribution of the exciting electron and on their cross-sections for collisional excitation, assuming that collisional deactivation of these levels can be ignored.

$O^{++}$ is a good example of an ion of this kind and its transition scheme is shown in Fig 1.1. Thus the ratio:

$$\frac{\lambda 4363 A^{o}}{\lambda 4959 A^{o} + \lambda 5007 A^{o}}$$

is temperature sensitive. This method was first suggested by Menzel et al (1941). Much work has been carried out on the exact form of this temperature dependence, especially by Eissner et al (1969).

FIG. 1.1 TRANSITION SCHEME: FORBIDDEN LINES

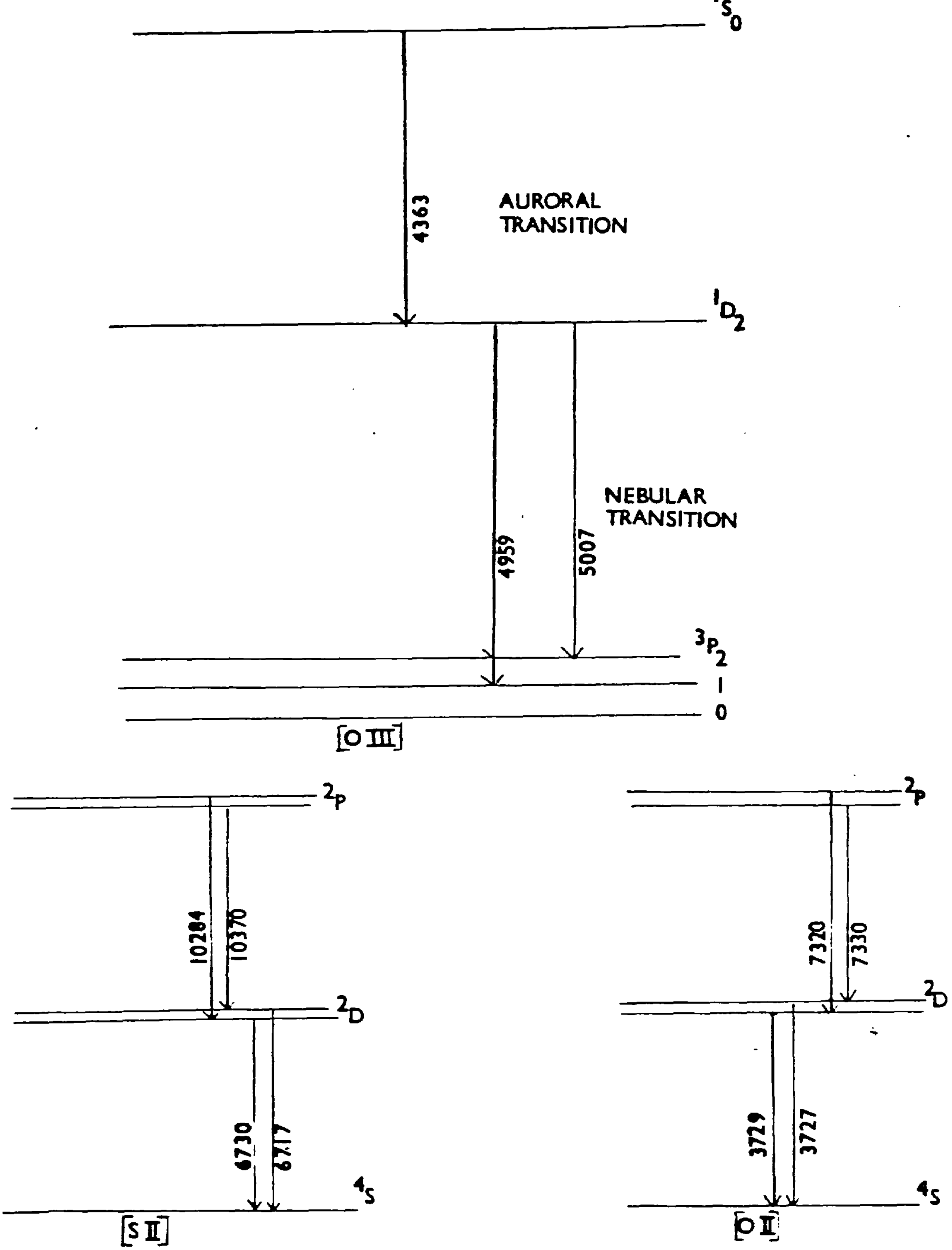

### b) From Continuum Measurements

Another ratio which is temperature sensitive is the relative strength of the recombination continuum with respect to a recombination line. This is because the emission in the continuum per unit frequency interval depends upon the width of the free-electron velocity distribution function. This method is much less accurate than the previous one because the continuum is both weak and contaminated by weak lines and stellar continuum.

### c) From Line Widths

The Doppler width ($\Delta\lambda_D$) of a line is sensitive to both the temperature (T) and the mass (m) of the ion. If the mass is low, then $\Delta\lambda_D$ will be large and the line width will be dominated by the Doppler broadening. If the other broadening effects can be estimated and removed then the residual width is a direct measure of the temperature. The exact shape of the Doppler profile is derived in Section 2.2.3. It is convenient to use the results of this derivation in advance:

$$T = \left[\frac{c}{\lambda}\,\Delta\lambda_{RES}\right]^2 \frac{m}{2k} \qquad (1.9)$$

Where $\Delta\lambda_{RES}$ is the residual $^1/_e$ width due to the Doppler broadening.

However, small errors in $\Delta\lambda_{RES}$ are magnified by the second power and hence lead to large errors in the estimate of T. This method is useful though for obtaining rough estimates and upper limits, and it has the advantage that it can be used on any line and therefore in many different regions of a stratified nebulae.

### 1.6.2 Electron Density Measurements

If an ion possesses two different levels with approximately the same excitation energy, then the relative excitation rates to the two levels will depend only upon the ratio of the collision strengths. If these levels have different radiative transition probabilities then one will be more liable to collisional de excitation that the other. In this case the relative strengths of the two lines will be dependent upon the electron density. OII and SII are the most prominent examples of ions of this nature and the relevant energy levels are shown in Fig 1.2. The density sensitive ratios are:

$$\frac{\lambda 3729}{\lambda 3727} \quad \text{for } [\text{OII}]$$

and

$$\frac{\lambda 6730}{\lambda 6717} \quad \text{for } [\text{SII}]$$

## 1.7 Previous Spectographic Work

The earliest study of the spectrum of planetary nebulae seems to have been performed by Huggins (1864) who used a prism spectroscope, and succeeded in identifying the lines of Nitrogen. Later Lockyer (1894) and Campbell (1894) took measurements on several lines at low dispersion. Wilson (1946, 1950), used a high resolution coudé grating spectrograph to obtain data on a large number of lines. Data was also obtained using a slitless spectrograph to produce a series of monochromatic images of a nebula providing invaluable information on stratification. Wilson (1958) also used a multi-slit grating spectrograph to obtain radial velocity data at several thousand points on the Orion nebula. However, difficulties were encountered in the reduction of this data due to the varying line widths and overlapping line images from the multi-slit.

Dopita and Gibbons (1975) have used a cassegrain image tube spectrograph whilst Gull (1978) has used an echelle spectrograph to obtain both spatial and spectral information.

Fabry Perots have been used in the pressure scanning mode, notably by Smith and Weedman (1970), studying the kinematics of HII regions, and by Elliott and Meaburn (1975) studying radial velocity variations in M17.

A later development is the servo-controlled FP developed by Hicks et al (1974) data from which has been used in the construction of a model for NGC7027.

The advantage in Resolution-Luminosity product enjoyed by the Fabry Perot over the grating spectrograph can be more than offset by the ability of the grating to record all the spectral elements simultaneously from a number of positions on the slit.

The Fabry Perot, however, recovers its advantage when used with multi element detector arrays which enable the study of many spatial positions simultaneously. The use of a Fabry Perot with detectors of this type is discussed in Chapter 5.

## 1.8 Conclusions

It seems clear then that an investigation of the spatial variation of the spectral line profile, its intensity and any associated velocity splitting, can yield valuable information concerning its internal motions, its structure and the electron temperature and density prevalent in various regions.

# CHAPTER 2: INSTRUMENTATION: INSTRUMENTAL DESIGN AND CONSTRUCTION

## 2.1 Introduction

This Chapter is devoted to a consideration of the various factors influencing the shape of the spectral line profile, followed by a discussion of the instrumental considerations and a description of the instrumentation constructed by the author in order to conduct the investigation outlined in the previous Chapter.

## 2.2 Spectral Line Shape

In this section, the effects which govern the shape of the spectral lines emitted from planetary nebulae are considered in order that we may define the basic parameters of a spectrograph to study them.

### 2.2.1 Intrinsic Width

An atom which is losing energy to the radiation field, ie is in the process of emitting a photon and making a downward transition to another state, cannot be considered as a conservative system. The discrete energy levels are replaced by maxima of probability in a continuous energy spectrum.

The halfwidth of the energy distribution $\Delta E$ is related to the lifetime $\Delta\zeta$ of the excited state according to Heisenberg's uncertainty principle:

$$\Delta E \, \Delta\zeta \approx h \qquad (2.1)$$

$\Delta\zeta$ is evaluated by considering the transition probabilities of all possible transitions to lower levels, such that:

$$\frac{1}{\Delta\zeta_i} = \sum_j A_{ij} \qquad (2.2)$$

## Table 2.1

| ION | Line (Angstroms) | Natural Line Width (Angstroms) |
|---|---|---|
| [OIII] | 4363 | $3.10^{-13}$ |
| | 4959 | $5.8.10^{-15}$ |
| | 5007 | $6.10^{-15}$ |
| [NII] | 6583 | $1.47.10^{-15}$ |
| | 6548 | $1.45.10^{-15}$ |
| [OII] | 3728.8 | $4.95.10^{-18}$ |
| | 3726.1 | $2.12.10^{-17}$ |
| H | 6563 | $6.8.10^{-2}$ |
| | 4861 | $2.6.10^{-2}$ |

Where Aij is the probability of a transition from state i to state j.

The width of a line due to radiation damping is equal to the sum of the widths of the two levels involved in the transition. Table 2.1 gives the natural line widths calculated for some of the transitions of importance in planetary nebulae.

### 2.2.2 Intrinsic Line Shape

Classically, the natural line shape may be derived by considering the frequency dependence of the energy loss of the damped harmonic oscillation of a dipole. Quantum mechanical considerations yield an identical result. The shape of the line depends upon the shape of the energy level distributions defining the levels under consideration.

The radiation field may be considered as the damping term in the equation of motion of an oscillating dipole:

$$\ddot{x} + \gamma\dot{x} + \omega_o^2 x = 0 \qquad (2.3)$$

Where $x$ is the displacement

$\omega_o$ is the angular frequency

$\gamma = 1/_{\Delta\zeta}$ where $\Delta\zeta$ is the classical lifetime

For small damping the solution of this equation is of the form

$$x = ae^{-\gamma/2t} \cos \omega_o t \qquad (2.4)$$

Only an infinitely long wavetrain of constant amplitude is truly monochromatic. The length of the wave train emitted by this oscillating dipole, may be considered as being defined by the super-position of the different frequencies spread around $\hat{\omega}_o$.

Fourier analysis of this damped wave allows the derivation of the frequency dependence of the emitted intensity and hence the natural line shape.

$$X(\omega) = \int_{-\infty}^{+\infty} x(t) \, \exp(-iwt) dt \qquad (2.5)$$

$$I(\omega) = X(\omega) . X^*(\omega) = \frac{\gamma/2\Pi}{(\omega-\omega_o)^2+(\gamma/2)^2} \qquad (2.6)$$

This is known as the dispersion or Lorentz profile. When $\Delta\omega = \omega-\omega_o = \pm \gamma/2$, $I(\omega)$ drops to half of its maximum value. The convolution of two Lorentzians of halfwidths $\gamma_1$ and $\gamma_2$ leads to another Lorentzian of halfwidth = $(\gamma_1 + \gamma_2)$

### 2.2.3 Doppler Profile

For an ideal gas at temperature T, the gas molecules or atoms will be moving randomly in all directions. There will therefore be a spread in wavelength emitted by these atoms due to their spread in velocities.

For velocities V <<c we may make the approximation:

$$\Delta\lambda = \lambda o \nu/_c \qquad (2.7)$$

Assuming that the distribution of velocities v along the line of sight will be Maxwellian, then if $P(\nu)d\nu$ is the probability that a particle of mass m will be in the interval $\nu$ to $\nu+d\nu$ we have:

$$P(\nu)d\nu = C_1 \exp(-m\nu^2/2kT) \qquad (2.8)$$

Where $C_1$ is determined by the normalization condition:

$$\int_{-\infty}^{+\infty} P(\nu)d\nu = 1 \qquad (2.9)$$

Substituting from 2.7 for $\nu$

$$P(\Delta\lambda)d\Delta\lambda = C_2 \exp\left[-\left(\frac{\Delta\lambda}{\Delta\lambda_D}\right)^2\right] d\Delta\lambda \qquad (2.10)$$

Where $\Delta\lambda_D = \frac{\lambda}{C}\sqrt{\frac{2kT}{m}}$ (2.11)

$\Delta\lambda_D$ is the $\frac{1}{e}$ width of the profile

$C_2$ is a normalization constant

Clearly then the Doppler profile is Gaussian in form and its width is sensitive to both the temperature and the mass of the emitting ion or atom.

## 2.3 Line Broadening

### 2.3.1 Pressure or Collision Broadening

Classical impact theory has its origins in an analysis performed by Lorentz who considered the atom to be a radiating oscillator, perturbed by encounters with other particles, such that a change in phase occurs during the encounter. The wave train is assumed to suffer instantaneous phase dislocations. This has the effect of shortening the wavetrain and hence broadening the number of frequencies required to define it.

In planetary nebulae, the radiation of forbidden lines requires that collisions be sufficiently infrequent that atoms with lifetimes measured in minutes can radiate before being collisionally deexcited. Clearly, this renders any collisional broadening negligible for the forbidden lines and also for the recombination lines of H and He since these arise from the same regions of the nebula and are therefore subject to the same conditions.

### 2.3.2 Structural Broadening

The factors affecting line shape that have been considered so far have been generated on a 'microscopic' sale in the sense that they have not been influenced by large scale structure or movements of the emitting gas. 'Large scale' may be defined, for practical purposes, as being comparable to the seeing limit imposed by the telescope, ie 1" .

These effects manifest themselves in the following ways:

#### 2.3.2.1 Velocity Spread

The finite size of the entrance aperture of the spectrograph subtends an angle on the sky corresponding to a certain area on the nebula. If the nebula is in radial expansion, then this area will encompass a range of different velocities relative to the line of sight, corresponding to a spread in wavelengths (Fig 2.2). The exact form of this broadening function is dependent on the size of the aperture relative to the nebula, and also on the 'shape' of the velocity surface presented by the nebula.

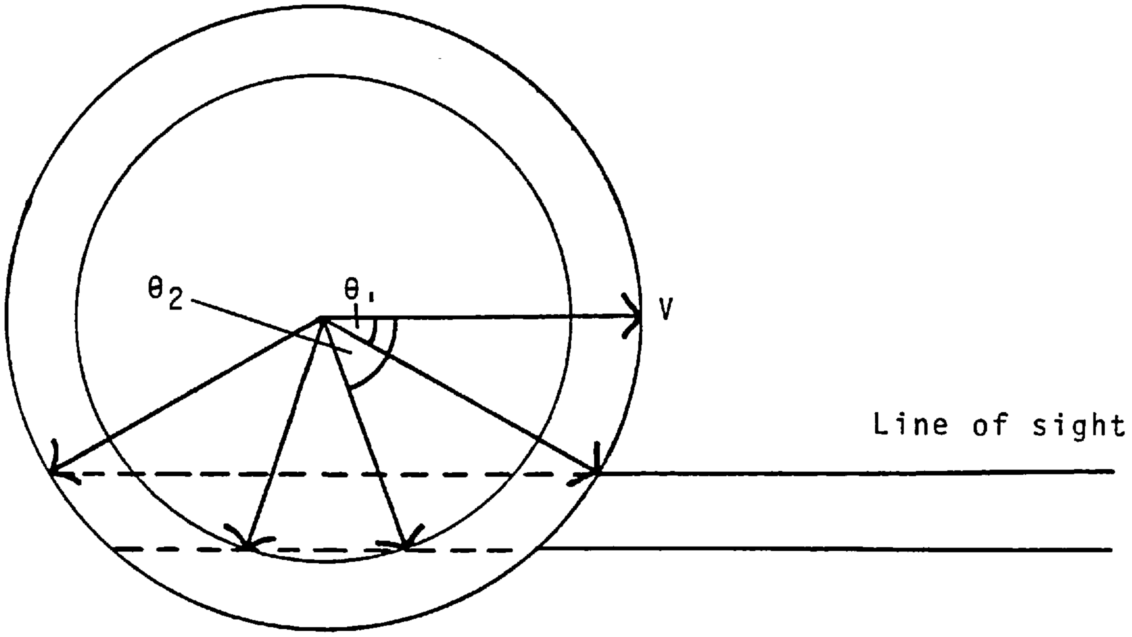

Figure 2.2 Diagrammatic representation of spread in velocities along the line of sight.

### 2.3.2.2 Profile Distortion

The presence of large scale inhomogeneities in the nebula, such as neutral globules or condensations, can suppress or enhance part of the profile. The presence of dust mixed in with the gas can lead to an extinction, which is greater for light emitted from the back face of the nebula than for light emitted from the front face. Thus there is a wavelength dependent absorption. The presence of dust in the central hole will suppress all the light from the backface equally. These two situations are shown schematically in Figure 2.3. Obviously, the exact form of this extinction curve will depend upon the density distribution of the dust.

Changes in the level of ionization, the effective temperature or density, or the presence of large scale turbulence can all distort the observed profile.

### 2.3.3 Seeing and Guiding Fluctuations

Fluctuations in the seeing during a scan may affect the line profile by refracting more or less of the light from positions immediately adjacent to the entrance aperture. Effectively the size of the entrance aperture is

FIG 2.3 EXTINCTION DUE TO DUST

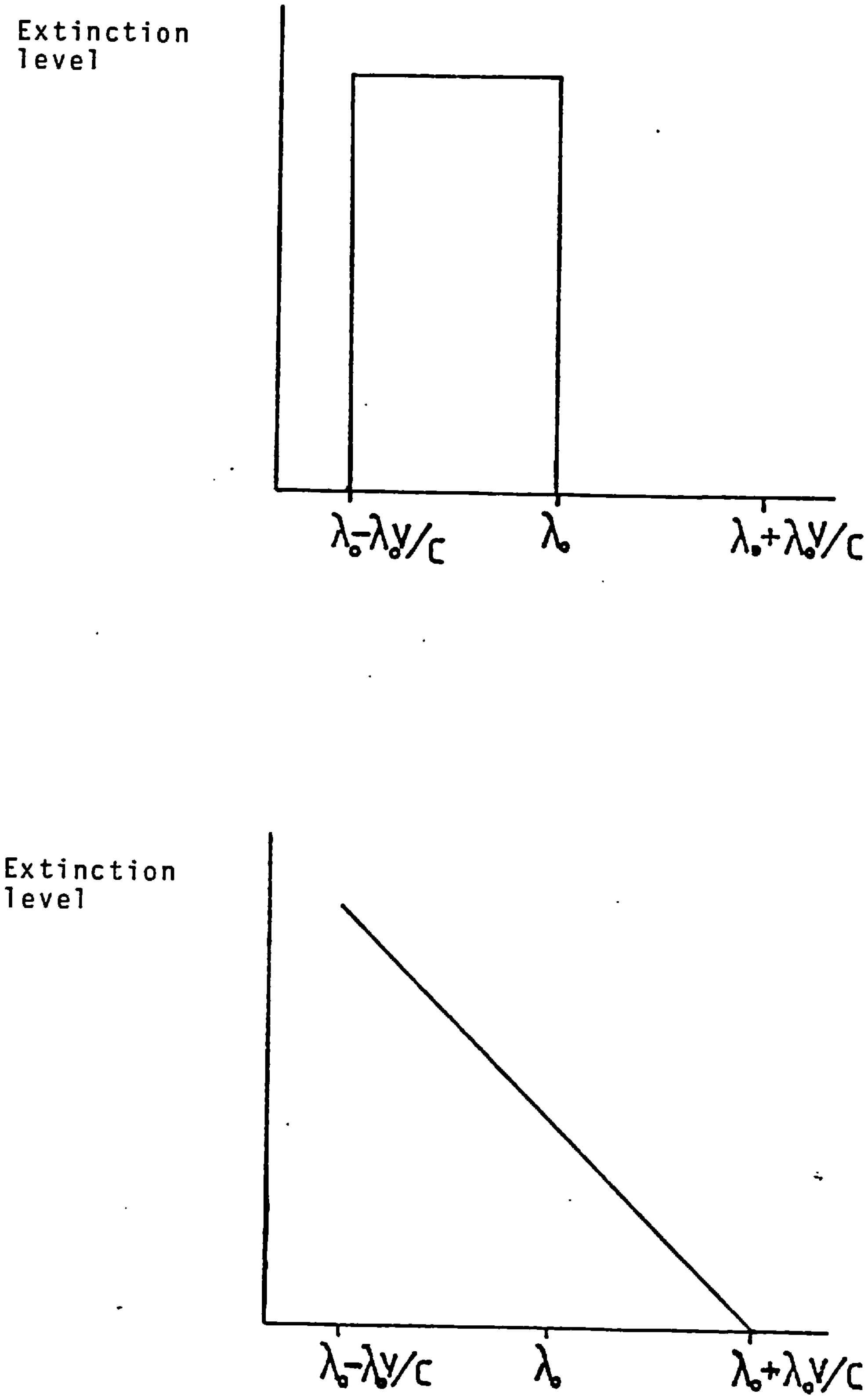

fluctuating and thus the broadening fluctuates. Fluctuations over a period shorter than the sampling period will average out to a simple broadening. Fluctuations over a period greater than the sampling period, but shorter than the time taken to record the whole scan will introduce a varying broadening which is effectively increasing the noise on the signal. In a similar manner systematic guiding or tracking errors can introduce some kind of broadening.

Effects such as those just described are virtually impossible to remove from the data and so they place constraints upon the observing conditions that are acceptable.

## 2.4 Instrumental Considerations

### 2.4.1 Spectral Resolution

The required spectral resolution is determined, ultimately, by the width of the spectral line to be studied and the detail in which we wish to study it. Measurements of the kinetic temperature of planetaries, made using the methods described in the previous chapter, indicate a figure which is usually in excess of $10^4$ °K. This sets a minimum value for the width of the spectral line of approximately 0.08A° for the 5007A° [OIII] line rising to about 0.3A° for $H\beta$ and $H\alpha$.

The sampling theorem (Nyquist, 1928) states that any signal which is band limited to an upper frequency limit Fhz may be completely specified by stating its values at a rate 2F per second or faster.

A lower limit on the width of any structure in the recorded spectrum is set by the width $\delta\lambda_I$ of the instrumental profile. Thus, in order that the resolution is not seriously degraded, the sampling theorem dictates a sampling interval S of less than $\delta\lambda_{I/2}$. In turn it is preferable if the profile width $\delta\lambda_I$ is less than the line width $\delta\lambda_L$ such that:

$$\delta\lambda_I < \frac{\delta\lambda_L}{2}$$

However, in this situation there is some loss of information. The highest frequency present in the spectral line is given by the highest component in its Fourier Transform. It is this frequency which defines the sampling interval if no information at all is to be lost. It is usual to compromise such that:

$$2S < \delta\lambda_I < \delta\lambda_L/_2 \qquad (2.12)$$

This implies a resolution of between $3.10^4$ and $10^5$ for the case as outlined above.

### 2.4.2 Instrumental Profiles

The resolving power R of a spectograph is defined by:

$$R = \lambda/_{\delta\lambda} \qquad (2.13)$$

Where $\delta\lambda$ is the full width at half maximum of the instrumental profile.

This definition is somewhat misleading however because the actual shape of the profile has a large influence on the resolvability of the recorded spectrum. This is especially important for work on absorption lines, where profiles with extended 'wings' can lead to a large amount of infilling to the line.

Figure 2.4 compares the results of convolving an observed emission line with three different profiles: an Airy function characteristic of a Fabry Perot, a sinc function characteristic of a Michelson, and a Gaussian. The full width at half maximum of the profiles was the same. Clearly the sinc function distorts the profile very little, whilst the Airy and the Gaussian depress the peaks and fill in the dip between the peaks. This illustrates the differences in resolvability encountered with instruments of supposedly identical resolution and demonstrates the superiority of the Michelson profile for detailed study of line shapes.

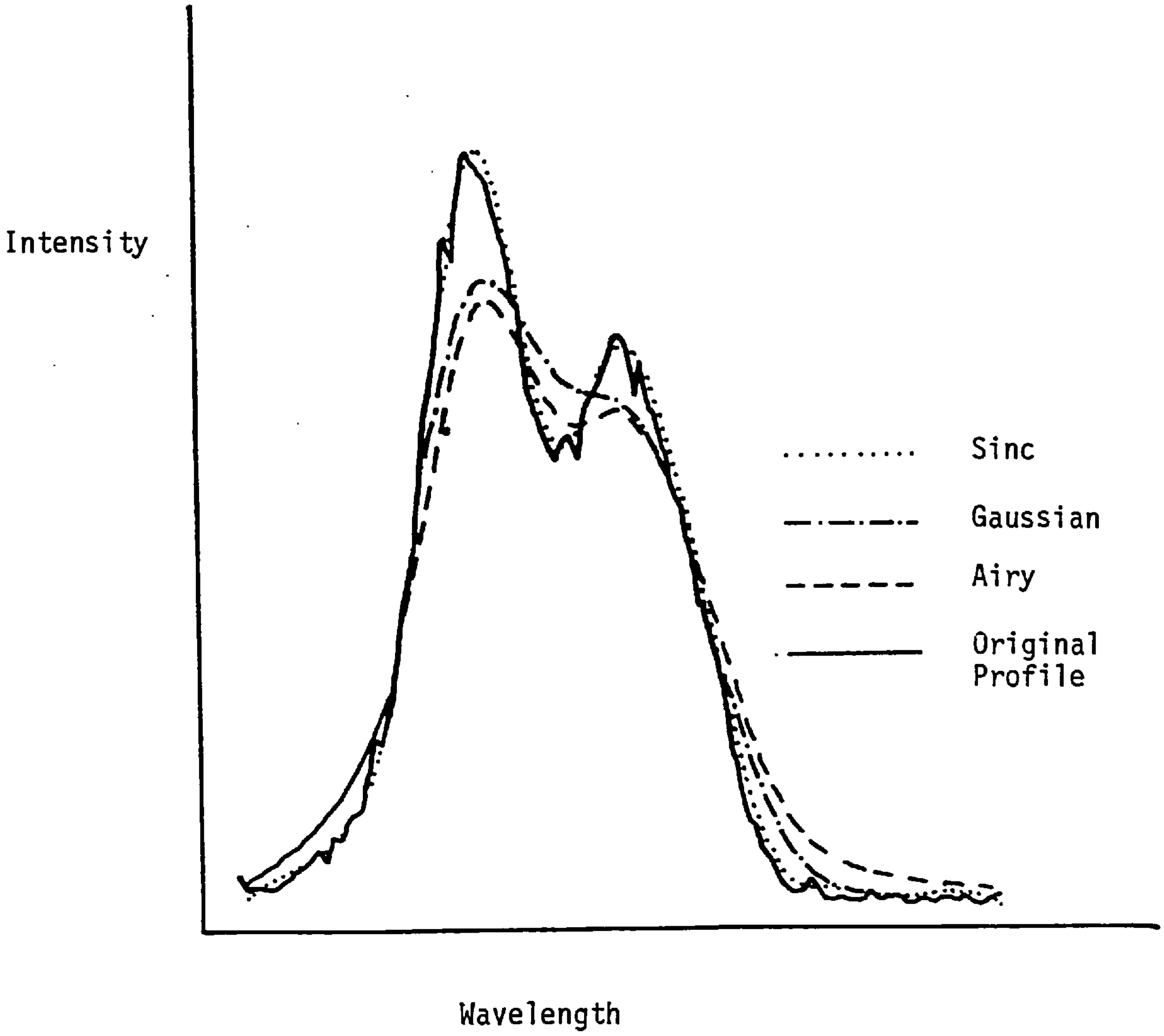

Figure 2.4 Comparison of broadening effects of different functions

### 2.4.3 Resolution-Luminosity Product

The advantage of the Fabry Perot Interferometer, in terms of its resolution luminosity product, over the grating and prism spectrometers, was first recognized by Jacquinot (1954).

A spectrograph may be characterized by two fundamental quantities: its resolution and its luminosity. A comparison of equal areas of dispersing element for the same resolving power reveals the superiority of the Fabry Perot spectrometer over the grating, and of the grating over the prism spectrograph. For nebular work this superiority can be of the order of a factor of 100 for the FP over the grating. The fundamental reason for the superiority of the FP is its rotational symmetry and the use of a whole closed fringe, embracing the direction where all interfering rays coincide. This advantage in R-L product, which takes the form of a large acceptance angle for a given resolution, is similar for the Michelson interferometer. The Michelson, however, is not so suitable for use with multi-element detectors, owing to the need to Fourier transform the interferogram to recover the spectrum. With the advent of microprocessors this disadvantage may become insignificant.

Clearly then the Fabry Perot has distinct advantages in R-L product over conventional spectrometers. The shape of its instrumental profile is not vastly inferior to that of the Michelson for emission line work, and it is easily portable and relatively inexpensive. It was for these reasons that the Fabry Perot Interferometer was chosen to carry out this programme of research.

## 2.5 The Fabry Perot Interferometer

### 2.5.1 Basic Equations

The fundamental equation governing the intensity of light (I) transmitted through a Fabry Perot is the Airy function:

$$\frac{I}{I_o} = \frac{1}{1+\frac{4N_R^2}{\Pi^2}\sin^2\left(\frac{2\Pi\mu t\cos\theta}{\lambda}\right)} \qquad (2.14)$$

Where $N_R$ is the reflective finesse

$t$ is the plate spacing

$\lambda$ is the wavelength of the light

$\theta$ is the off-axis angle

$\mu$ is the refractive index

The condition for a maximum of transmission is given by:

$$n\lambda = 2\mu t\cos\theta \qquad (2.15)$$

Where n is the order.

The effective finesse $N_e$ is defined as the ratio of the inter-order spacing ($\Delta\lambda$) or free spectral range to the full width at half maximum of the instrumental profile $\delta\lambda$:

$$N_e = \frac{\Delta\lambda}{\delta\lambda} \qquad (2.16)$$

Where $$\Delta\lambda = \frac{\lambda^2}{2t} = \frac{\lambda}{n} \qquad (2.17)$$

The wavelength resolution $^{\lambda}/\delta\lambda$ is given by:

$$R = \frac{\lambda}{\delta\lambda} = \frac{\lambda N_e}{\Delta\lambda} = nN_e = \frac{2\mu t}{\lambda} N_e \qquad (2.18)$$

It is possible to associate a defect finesse $N_D$ with the spread in plate spacing due to micro defects or spherical bowing where:

$$N_D = {}^{m}/_{2} \qquad (2.19)$$

Where the errors are of magnitude $^{\lambda}/_{m}$

It is also possible to associate a reflective finess $N_R$ with the reflectivity of the coatings where:

$$N_R = \frac{\Pi\sqrt{R}}{1-R} \qquad (2.20)$$

We may define an aperture finesse $N_A$ due to the spread of $\theta$ due to the finite sized aperture where:

$$N_A = \frac{2\Pi}{n\Omega} = \frac{2\Pi}{n\Pi\theta^2} = \frac{2}{n\theta^2} \qquad (2.21)$$

The effective finesse $N_e$ which results from a combination of these effects is given by:

$$N_e = (N_A^{-2} + N_R^{-2} + N_D^{-2})^{\frac{1}{2}} \tag{2.22}$$

### 2.5.2 Scanning

Inspection of the equation describing the condition that light will be transmitted by a Fabry Perot (2.15) suggests three distinct methods of changing the transmitted wavelength:

#### 2.5.2.1 Pressure Scanning

At constant t and $\theta$ a change $d\mu$ in the refractive index produces a change in the transmitted wavelength of $d\lambda$ where:

$$\frac{d\lambda}{d\mu} = \frac{2t\cos\theta}{n} = \lambda\cos\theta \tag{2.23}$$

At $\theta = o$, ie on axis

$$\frac{d\lambda}{d\mu} = \lambda \tag{2.24}$$

A change in the pressure dP will result in a change of the refractive index $d\mu$ given by:

$$\frac{dP}{d\lambda} = \frac{dP}{d\mu} \cdot \frac{d\mu}{d\lambda} = \frac{dP}{d\mu} = \frac{n}{2t} \qquad (2.25)$$

$$\therefore \; \Delta\lambda = \frac{2t}{n} \frac{d\mu}{dP} \Delta P = \frac{\lambda d\mu}{dP} \Delta P \qquad (2.26)$$

For air at 20°C the scanning range is approximately 1.2A° per atmosphere at 4000A°.

The beauty of this method is its simplicity, and it has been used extensively by many workers (Geake et al, 1959; Hindle and Reay, 1967). This method is particularly useful in the situation where a Fabry Perot is used with a grating premonochromator or in tandem with another FP as the passbands scan in synchronism as the pressure is changed.

The scanning range using this method is limited by the maximum pressure of the vessel containing the FP. The use of gases of high $d\mu/dP$ such as propane (0.0011) can increase the scanning rate to about 4.4 Å per atmosphere at 4000A°. The scan rate is limited by the need to prevent adiabatic expansion of the gas from introducing thermal instabilities to about 5A° per minute.

### 2.5.2.2 Scanning in Angle

Differentiation of equation 2.15 with respect to $\theta$ gives:

$$\frac{d\lambda}{d\theta} = \frac{2\mu t}{n} \sin\theta \tag{2.27}$$

Thus the dispersion in wavelength is apparent as a spatial separation of the fringe systems formed by the different wavelengths. There are several methods of utilizing this dispersion.

#### (a) Scanning by Tilting

For a single point detector we may scan in $\lambda$ by moving the detector across the fringe system or, more usually, by tilting the etalon. This has the fundamental disadvantage that the instrumental profile width and shape changes during a scan due to the change in dispersion. The resolution or the luminosity of the system is also much reduced.

When scanning between the central order and the first ring - if the spectral resolution is to be maintained over the scan then the detector must be matched to the angular halfwidth of the outer ring, where the fringe width is smallest. This will give a variation in resolution through the scan of about $\sqrt{2}$, the maximum occurring when $\theta = o$. There is also a variation in the luminosity because of the variation of the transmission across the detector with $\theta$. Again the luminosity is a maximum when $\theta = 0$.

The biggest single disadvantage of this method of scanning, aside from the variations in R & L mentioned previously, is its failure to utilize the full Jacquinot criterion in the central order. This represents a loss in luminosity, compared to methods which scan the central spot only, given approximately by the square of the ratios of the angular halfwidths of the central spot and the first ring.

The angular width $\delta\theta$ of a ring appearing at an off-axis angle $\theta$ is given by:

$$\delta\theta = \frac{1}{R\theta} \qquad (2.28)$$

The Jacquinot criterion $\theta_J$ for the central order is given by:

$$\frac{\theta_J{}^2}{2} = \frac{1}{R} \qquad (2.29)$$

Thus $$\frac{\delta\theta^2}{\theta_J{}^2} = \frac{R}{2} \cdot \frac{1}{R^2\theta^2} = \frac{1}{2R\theta^2} \qquad (2.30)$$

If we scan over one whole order to the first bright ring, then:

$$\cos\theta = \frac{n-1}{n} = 1-\frac{1}{n} = 1-\theta^2/_2 \qquad (2.31)$$

Thus:

$$\frac{\delta\theta^2}{\theta_J{}^2} = \frac{1}{2R2}\,n = \frac{1}{4N_R} \qquad (2.32)$$

This analysis does not take into account the variation in the relative transmission across the detector, which changes with θ. However, over one order, this represents a change of around 25% at maximum.

### (ii) Photographically

More usually the dispersion across the field is used by recording the fringes photographically. In this case it is important to match the resolution limit of the detector to the minimum width of the fringes. The gain of the system is directly proportional to the number of complete fringes observed, as the area of each ring is equal. However only part of the field is transmitting light. The ring system may be scanned over the rest of the field either by altering θ, μ or t.

A recent development by Courtes (1966) and Meaburn (1975) is the image tube insect eye spectrograph. Briefly a Fabry Perot etalon of constant gap is placed in the focal plane of the telescope and a number of fish eye lenses are used to isolate various parts of the field. The light incident on any one of these lenses is dispersed by the F.P. and an image of the primary mirror is formed at the detector, with a series of fringes superimposed upon it. In this the detector is an electronographic camera and the fringe patterns are recorded on electronographic emulsion. Spectral information is recovered by scanning the fringe patterns with a microdensitometer. This arrangement has a spectral gain which is proportional to the number of complete fringes produced by only one lens, and a spatial gain which is proportional to the number of lenses, compared to the single fringe gas spaced F.P. of equivalent diameter.

### 2.5.2.3 Scanning by Variation of Plate Spacing

Differentiation of equation 2.15 with respect to t gives:

$$\frac{d\lambda}{dt} = \frac{2\mu}{n}\cos\theta \qquad (2.33)$$

The fundamental difficulty involved in scanning the F.P. by varying the plate separation is the requirement that the plates remain parallel such that the overall finesse is not degraded. This implies an accuracy of better than the surface flatness of the plating, ie $\lambda/200$. This has been achieved with varying degrees of success, by the use of parallel spring strips, magnetostrictive transducers and piezo-electric transducers. Parallel spring strips tend to be too crude for use in the visible being more suited to longer wavelength applications where the tolerances are less severe. Transducers are in widespread use as activators nowadays, especially in the piezo electric form which has greater range and better linearity than the magnetostrictive type.

The important parameters to be considered when selecting a piezo-electric transducer are: the extension for a given applied voltage; the maximum or breakdown voltage; the linearity of the response; the hysteresis and the thermal coefficient of expansion. For systems where there is no feedback system to control the spacing or parallelism, it is necessary to select transducers with identical characteristics of expansion so that parallelism is maintained during a scan. The linearity of the response is not so critical as it can be calibrated out. Linearities of better than 2% over several microns of extension have been achieved.

The use of piezo electric transducers in Fabry Perot etalons falls into two main categories:

1) With optically contacted etalons (Smart and Ramsey, 1964; Bates et al 1968) where the piezo electric crystal is used as the spacer separating the plates. Quartz discs are glued with epoxy resin to each end of the transducer and these are polished flat and 'contacted' to each plate, the inter molecular forces bonding the two materials together. This is a very rigid configuration and is often used in rocket and balloon borne experiments where high stresses and vibrations are encountered. It has the disadvantage of having a fixed spacing and therefore a fixed resolution.

The piezo electric elements are very susceptible to thermal drifts, however, expecially when fabricated from several plates separated by brass electrodes. This cannot easily be compensated for in the optically contacted arrangement.

2) Spacer-less etalons: this mechanical arrangement permits compensation of the thermal expansion characteristics of the transducers and allows one to tailor the plate spacing, and hence the resolution, to the problem under investigation. This configuration is, however, susceptible to mechanical flexure, vibrations and drift.

The elimination of changes in the plate spacing due to mechanical and thermal drifts can be achieved using a servo control system to detect and correct the error. This will be discussed in section 2.6.

### 2.5.2.4 Central Spot Scanning

In this configuration the detector is placed on-axis ie in the central fringe or spot. The interferometer is then scanned by varying the gap t or the refractive index $\mu$ and the change in the fringe pattern is recorded by the detector. As the size of the detector, relative to the fringe pattern, is increased, so the luminosity of the system is increased whilst the effective resolution is decreased. The maximum luminosity will occur when the whole of the central fringe is being observed. However the resolution in this case is much degraded. Conversely the maximum spectral resolution is achieved when the detector is infinitely small. In this case the resolution tends to $R_{max}$ where:

$$R_{max} = n\left[N_R^{-2} + N_D^{-2}\right]^{-\frac{1}{2}} \qquad (2.34)$$

However the luminosity of the system is now zero.

It is usual to compromise between these two situations such that the effective resolution $R_E$ and the effective luminosity $L_E$ are given by:

$$R_E = \frac{R_{max}}{\sqrt{2}}$$

$$L_E = \frac{L_{max}}{\sqrt{2}} \qquad (2.35)$$

This situation occurs when the spread in wavelength $\delta\lambda_D$ across the detector is equal to the wavelength spread defined by $\delta\lambda max = \frac{\lambda}{R_{max}}$

From 2.27

$$\frac{d\lambda}{d\theta} = \lambda \sin\theta$$

As $\theta$ tends to zero, so $d\theta$ tends to $\theta_J$ and sin $\theta$ tends to $\theta_{J/2}$ where $\theta_J$ is the off-axis angle subtended by the detector.

Thus: $$\frac{\theta_J^2}{2} = \frac{1}{R_{max}} \qquad (2.36)$$

which is the Jacquinot criterion (Jacquinot, 1954).

The degradation of the resolution due to the finite size of the detector (or entrance aperture) may also be described by the aperture finesse $N_A$ where $N_A = \frac{2}{n\theta^2}$.

It is not necessary to confine ourselves to the central fringe however and, by using annular masks to isolate the maxima of the ring pattern for a particular wavelength it is possible to increase the luminosity of the system, (Meaburn, 1968). These masks are usually produced by photographing the ring pattern produced by the line under observation. As the area of each ring is equal, the increase in the luminosity is directly proportional to the number of rings.

## 2.6 The Servo-Control System

### 2.6.1 Introduction

A servo system may be divided into two separate component parts: the error detection system and the error correction system. Two distinct methods of servo-controlling Fabry Perots, developed by Ramsey (1962) and Hicks et al (1974) share the same method of error correction, ie piezo-electric transducers. It is in the detection of the error that the systems differ.

The Ramsey system uses Brewster fringes formed by double-passing the etalon to detect deviations from parallelism. A narrow beam of white light is passed through the etalon at one end of a diameter, reflected across the aperture and then passed back through the etalon at the other end of the diameter. Any differences in the gaps results in a drop in the intensity of the transmitted beam. This is detected by a photo multiplier tube, amplified and fed back to the piezos such that the error is corrected.
It is necessary to impose a small 'jitter' on one of the plates in order to sense the direction of the error.

The Hicks-system employs the techniques of capacitance micrometry, developed by Jones and Richards (1973), and will be discussed in more detail later on.

The major disadvantage of the Ramsey system is the leakage of light from the servo-channels into the signal channel, giving noise levels of several counts per second. This is not compatible with the study of faint objects. Furthermore, sudden changes in the gap of greater than one fringe cannot be rectified as the system will lock onto the next fringe.

### 2.6.2 Description

The servo- system used to stabilize the Fabry Perot has been described by Hicks (1974 b). It is convenient to recall some of the salient features in order to illustrate the constraints imposed on the mechanical design.

The servo utilises capacitance micrometry to detect small changes in plate spacing. The error signal so derived is amplified and fed back to the piezo electric transducers in such a manner that they expand or contract, correcting the deviation from parallelism. Capacitor pads are formed around the edge of each Fabry Perot plate by evaporating gold onto chromium to form the arrangement shown in Fig 2.5. The plates are then positioned one on top of the other such that five parallel plate capacitors are formed, there being two on each orthogonal axis and a fifth pad to monitor the overall plate spacing.

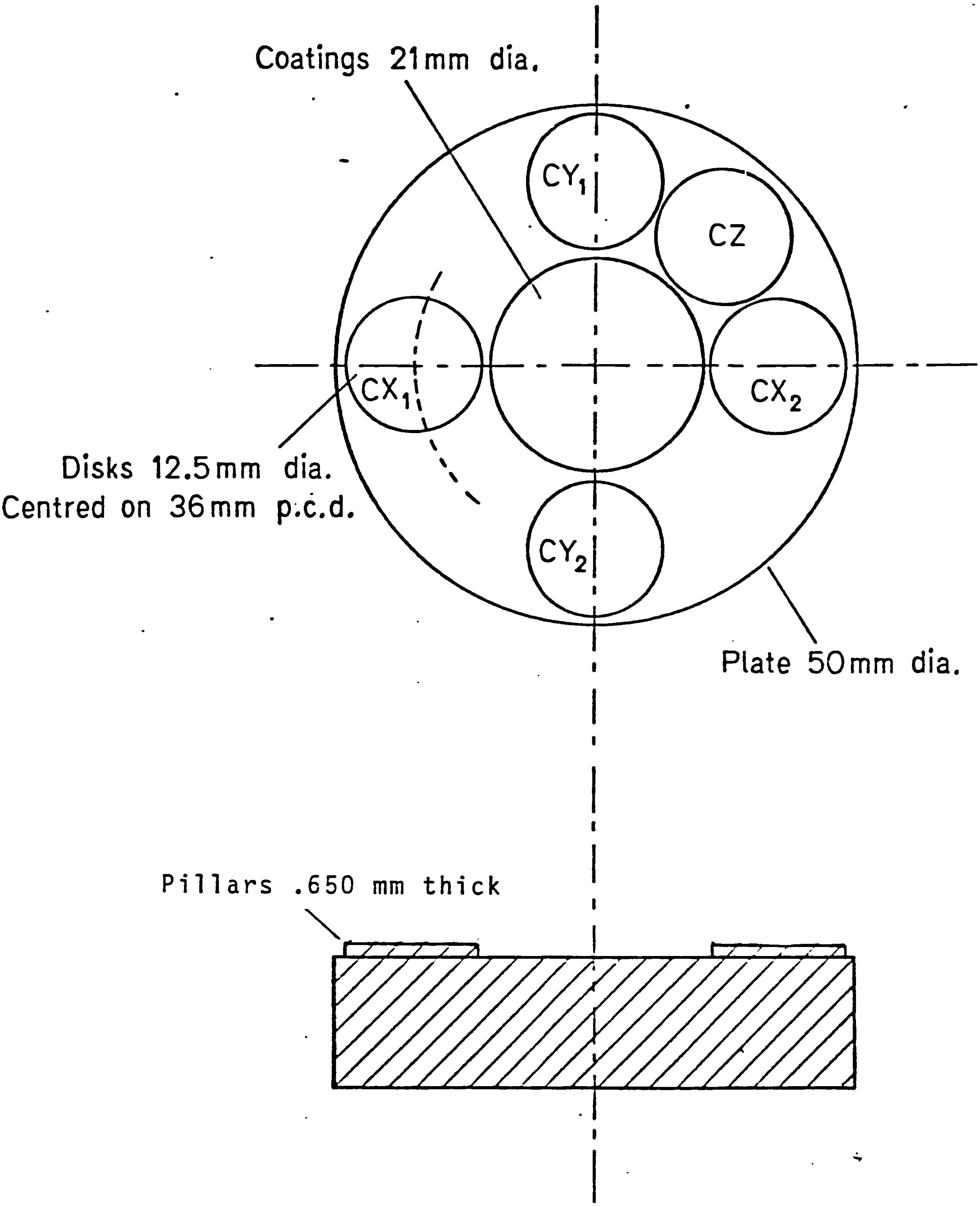

FIG. 2.5 CAPACITOR PAD ARRANGEMENT

A capacitance micrometer functions by allowing the displacement to be detected to vary the geometry and hence the capicitance of some form of capacitor. The capacitance of a parallel plate capacitor is given by:

$$C = \frac{KA}{t} \qquad (2.37)$$

where K is the dielectric constant of the material between the plates

A is the overlapping area

t is the distance between the plates

A change in spacing dt is accompanied by a change in capacitance dc where

$$dc = \frac{-KAdt}{t^2} \qquad (2.38)$$

The optimum capacitor gap is dictated by the sensitivity required of the system, and the relative importance of stray capacitances, which tend to obscure the changes in the gap. For this application, the optimum gap is about 50µ. Clearly this is not necessarily the value required for the overall spacing of the F.P, as this is dictated by the required resolution, and so the pads are formed on pillars which are optically contacted to the plate surface. The height of these pillars is chosen to be the required optical gap, less 50µm.

It is convenient to make the pads evaporated onto one plate larger than those on the other plate, so as to prevent mismatch of pad areas, inducing large imbalances in the bridge, reduce sensitivity to lateral shifts of the plates, and minimise edge effects.

The F.P. plates are aligned parallel by looking at fringes from an emission line lamp. The values of the capacitors formed on either side of a diameter are compared using a transformer ratio arm bridge arrangement (Jones and Richards, 1973 Figure 2.6) and are equalized by using small offsets in capacitance and resistance. The correct spacing is achieved by comparing the Z capacitor with an external reference capacitor whose value has been selected.

When all three bridges have been balanced the servo-loop is closed. When $C_1 \neq C_2$ a current $i_D$ will flow through the low impedance detector. The sensitivity of the bridge to changes in capacitance is given by:

$$\frac{di_D}{dc} = j\omega V_i \qquad (2.39)$$

Where $\omega$ is the bridge drive frequency

$V_i$ is the bridge drive voltage

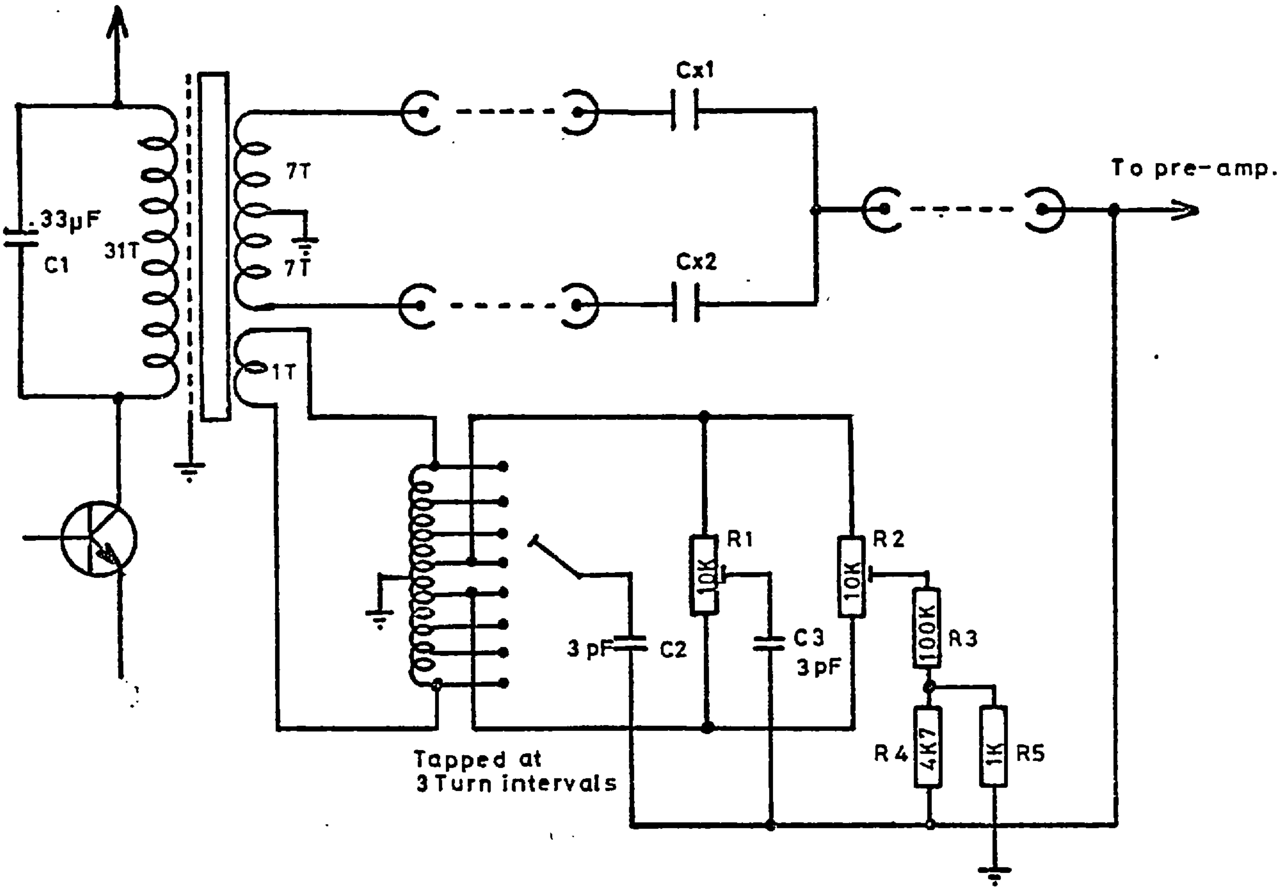

FIG. 2.6 X-CHANNEL RATIO ARM BRIDGE

The bridge drive frequency, $\omega$, is 16 khz as this is sufficiently low to render stray reactances unimportant, yet high enough to give a reasonable sensitivity.

The coarse capacitative offsets can switch in up to 0.5 pF in parallel with either micrometer, whilst the fine control may feed in up to 20 fF. This corresponds to a total range of about 2 orders.

Resistive balance controls are also provided to take out unequal resistive components in the two arms of the bridge.

The error signal appearing across the low impedance is demodulated using a phase sensitive detector, amplified, and fed back through a high tension supply to the appropriate transducer, or combination of transducers, as determined by a coordinate transformation unit. This unit allows three transducers, spaced equally around a circumference, to correct errors detected across orthogonal axes.

The time constant $\zeta$ and gain M of the servo-system may be varied so as to give the best operating conditions. $\zeta$ is set in the integrating amplifier of the P.S.D. and is deliberately made larger than the time constant of any other part of the circuitry, ensuring that the complete system behaves as a single pole exponential lag, and is therefore stable.

### 2.6.3 Reference Capacitor

The value of the external reference capacitor is chosen using equation 2.37. Inspection of this equation shows a dependence of the capacitance on the dielectric constant K. The value of K for air is found to vary with both temperature and humidity (Bell, 1960), which will lead to changes in the absolute capacitance. If the external capacitor is of a ceramic or similar type then clearly its capacitance will not vary in the same way and drifts in the plate spacing are introduced. The use of an air spaced parallel plate reference capacitor, consisting of two fused silica discs spaced by, and optically connected to, three pillars, with capacitor pads formed on each disc, alleviates this problem to a certain extent, by rendering the capacitor so formed liable to extraneous drifts in exactly the same manner. Thus no error signal is generated as both the capacitor values drift together, and the plate spacing is maintained. Obviously it is necessary that the reference capacitor be placed in close proximity to the F.P. so that the conditions are identical.

## 2.7 Fabry Perots at the Cassegrain Focus

The incentive to use Fabry Perots at the Cassegrain, where operating conditions are much more severe, is provided by the numerous disadvantages of working at the Coude focus. Although in theory most of these disadvantages can be overcome, it is unusual to find a situation where this is the case.

Most large telescopes have five mirror Coude systems, although three mirror systems do exist. The extra throughput of a three mirror system may be offset against the reduction in operational efficiency incurred by the need to drive the declination mirror separately when finding or setting on an object. Reflection losses can be reduced, in principle, from around 20% down to a few percent by means of enhanced silver coatings. These coatings however are limited spectrally to wavelengths longer than 4000 $A^{o}$ and as a result they are not in widespread use.

Image rotation can also be a problem when studying extended objects both spatially and spectrally. Image rotators are available but tend to be lossy.

At the Cassegrain there may be large temperature and humidity fluctuations over short periods of time. Setting and tracking on objects can impose considerable changes in the gravitational load on the equipment, whilst the exposed position increases the susceptibility to electrical pick-up. The absence of image rotation and the increase in light levels by a factor of two or more, compared with Coudé foci, are its primary advantages.

Previously the use of F.P.s at Cassegrain has been confined to optically contacted, pressure scarred or piezo-scarred etalons. This is mainly due to the susceptibility of spacer-less or mica spaced etalons to vibration and drift under the severe operating conditions encountered (Smith et al, 1976). The inflexibility of optically contacted etalons and the potential of the capacitance servo-control system to stabilize a spacer-less F.P. under adverse conditions led to the design and construction of a spacer-less servo-controlled Fabry Perot for use at the Cassegrain focus.

## 2.8 Design

### 2.8.1 F.P. Parameters

In section 2.4.1 an operational resolution of between $3.10^4$ and $10^5$ was defined. From the Jacquinot criterion (Equation 2.36) and taking the higher resolution, we find a permitted off-axis angle through the Fabry Perot of $\sqrt{20} \times 10^{-3}$ radians. The diameter of the plates required is dependent on the area of the sky to be observed and the size of the telescope:

By conservation of energy:

$$A_{FP} . \Omega_{FP} = A_{TEL} . \quad D_{TEL} \qquad (2.40)$$

Which reduces to:

$$\theta_{FP} . \; D_{FP} = \theta_{TEL} . D_{TEL} \qquad (2.41)$$

For a 2.5m telescope and F.P. plates with a 2cm coated area we find an area on the sky of diameter 10 arc secs.

The resolution of the F.P. is given by equation 2.18 as $R = n.N_e$. Assuming an effective finesse of Ne = 30 then a resolution of 80,000 is obtainable with n = 2,600 corresponding to a gap of 650μ and thus pillars of 600μ. This corresponds to a free spectral range of 2A$^{o}$. The maximum transmission occurs when the effective finesse is as close as possible to the reflective finesse, the transmission T being given approximately by:

$$T = N_e/N_r \qquad (2.42)$$

Thus $N_R$ is chosen small enough to give a large T without degrading Ne. For Ne = 35 we choose $N_R = 50$ corresponding to a reflectivity of about 94%, as determined by equation 2.20.

### 2.8.2 Optical Configuration

In order to preserve the advantage in efficiency gained by using the Cassegrain focus, a simple system with the minimum of optical components in the path was designed.

The telescope forms an image of the source at the entrance aperture (E) of the instrument (Fig 2.7) which acts as a field stop. Behind the entrance aperture the light diverges, is collimated by a lens (L), passes

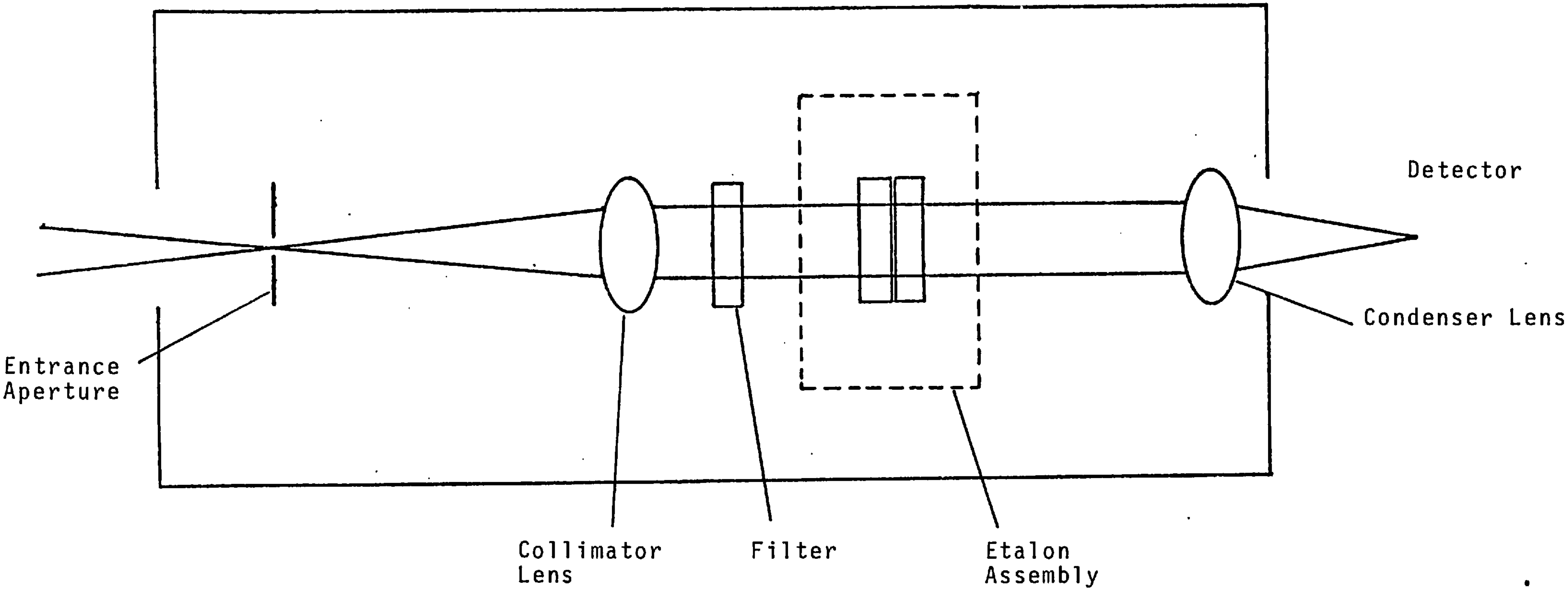

FIG. 2.7 OPTICAL LAYOUT OF INTERFEROMETER

through the Fabry Perot etalon and is then focussed by a condenser lens ($L_2$) onto the photocathode of a photomultiplier tube. Various mirrors and lamps were provided to allow for calibration and adjustment of plate parallelism. A bypass system was also provided to allow the photomultiplier to 'look' through the filter at the source, in order that the filter could be tuned to the correct wavelength for the object under observation. These facilities are shown in Figure 2.8.

### 2.8.3 Guiding

Guiding was performed by viewing the light reflected off the front face of the entrance aperture through the viewing system shown in figure 2.7. For this purpose, the entrance aperture was tilted at an angle of $22\frac{1}{2}^{\circ}$ to the incoming beam.

The aperture was formed by drilling a hole in a glass surface at an angle of $22\frac{1}{2}^{\circ}$ with a chamfered bit, the resultant hole being shown in figure 2.9(a). The front reflecting surface was formed by evaporating Aluminium onto the opposite face of the glass disc. When the diameter (d) of the aperture approaches the wall thickness x, one begins to lose a large proportion of the light due to vignetting. Referring to Figure 2.9(b),

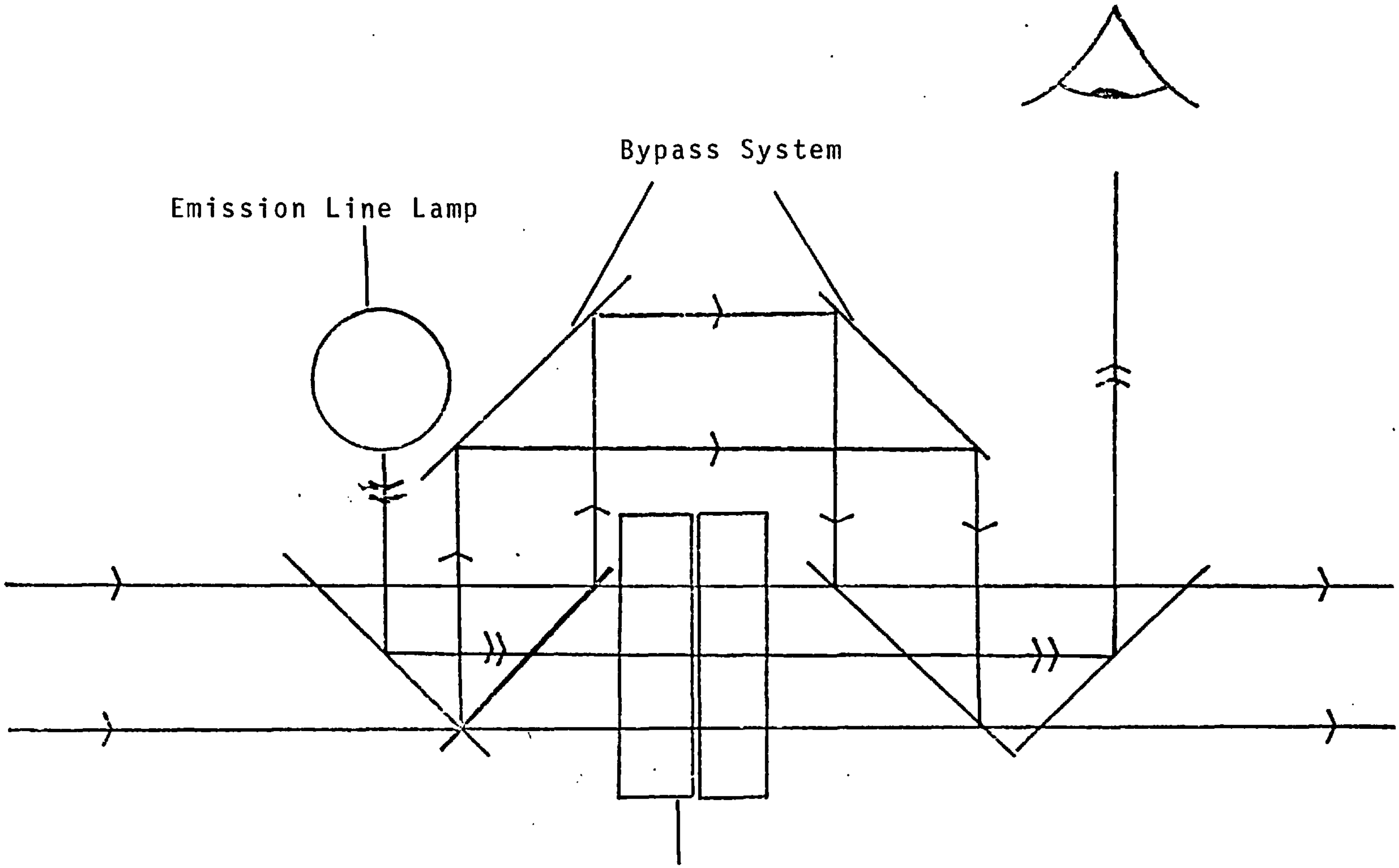

FIG. 2.8 BYPASS AND ALIGNMENT SYSTEM

FIG. 2.9(a) ENTRANCE APERTURE

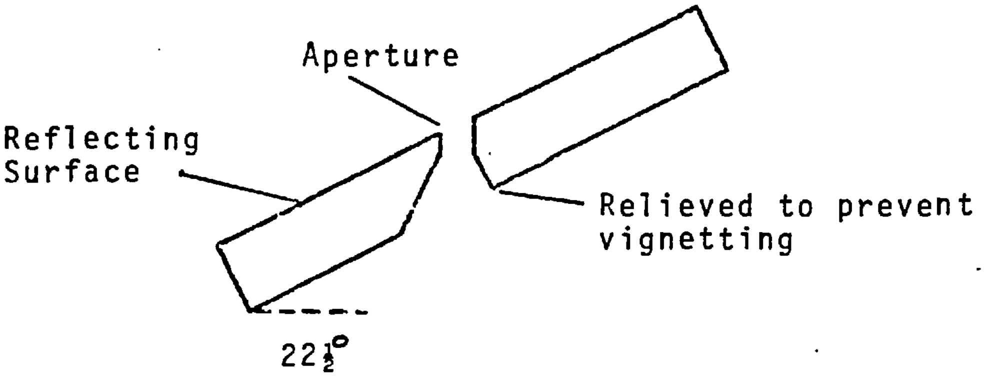

FIG. 2.9(b) VIGNETTING

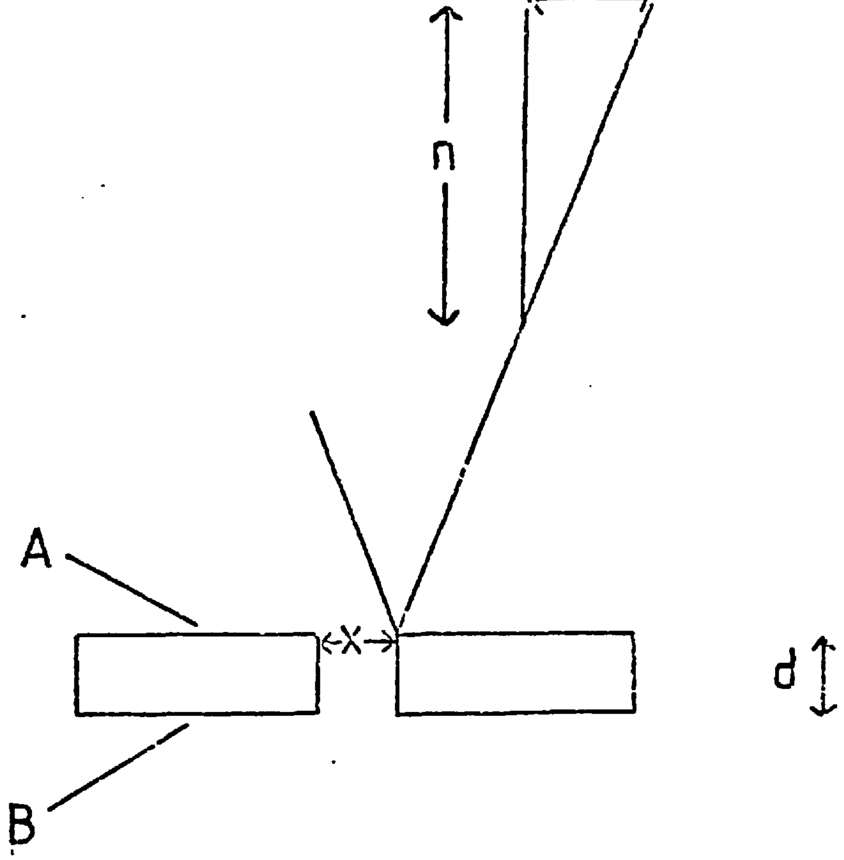

assuming a light beam of divergence f/n is focussed on to plane A then the light falling inside a radius x/2 at A diverges to fill a radius of $({}^{x}/_{2} + {}^{d}/_{2n})$ at B, of which only light inside a radius $^{x}/_{2}$ is allowed to pass.

Thus the fractional loss in light is given by:

$$F = 1 - \frac{(\frac{x}{2})^2}{(\frac{x}{2} + \frac{d}{2n})^2} \qquad (2.43)$$

In the case where d = x and using an f/14 beam we find a loss of 21.8% due to vignetting. On small telescopes with small image scales this situation occurs at apertures of about 5 arc seconds, corresponding to about 300μ diameter as this is about the limiting thickness that can be left by the ultrasonic drilling procedure. To alleviate this problem and also to increase the field of view sufficiently to enable one to use guide stars an offset guider was constructed.

### 2.8.4 Offset Guider

A schematic view of this is presented in Figure 2.10. A mirror is placed in the beam at 45° which deflects the light out to an Erfle-type guider eyepiece. A hole in the centre of the guider mirror allows light from the object to pass through and fall upon the entrance aperture.

The guider mirror is set on an adjustable carriage which is in turn mounted on a translation slide. This allows the object being studied to be observed periodically through the guider eyepiece. The eyepiece itself is mounted on an X-Y slide and an illuminated graticule is provided in the focal plane. This graticule is made from a disc of perspex with horizontal and vertical lines scratched upon it. The illumination is provided by means of a red L.E.D. shining through a polished edge of the disc. The L.E.D. was powered by a 9-volt battery and could be adjusted by means of a potential divider.

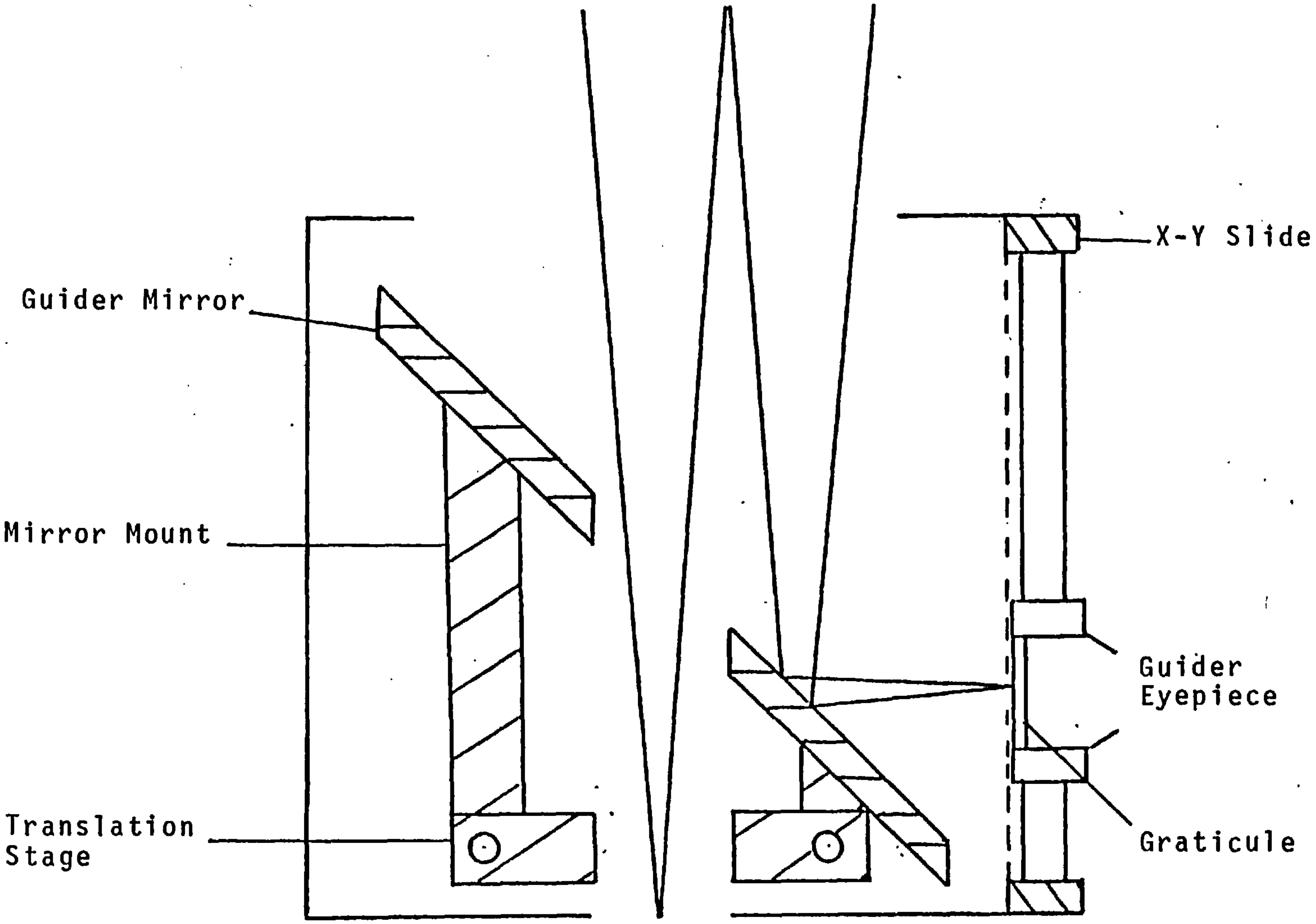

FIG. 2.10 OFFSET GUIDER BOX

### 2.8.5 Premonochromation

This was achieved using 50 mm diameter, three period interference filters of about 10 A$^{o}$ bandwidth, centred slightly to the red of the emission line under observation. The efficiency of these filters was typically about 55%. Fine tuning of the pass band was performed by tilting the filter with respect to the incoming beam. For ease of operation the filters were mounted in a 3-position filter wheel (Figure 2.11) with independent tilting adjustment available for each of them.

### 2.8.6 Collimation

The collimation was performed using a plano-convex lens mounted in an Ealing Optical adjustable lens mount. Adjustments in x,y,z and $\theta$ were provided for. The mount itself was fixed to a translation slide so that major adjustments in the aperture to lens distance could be made, providing for different collimating lenses.

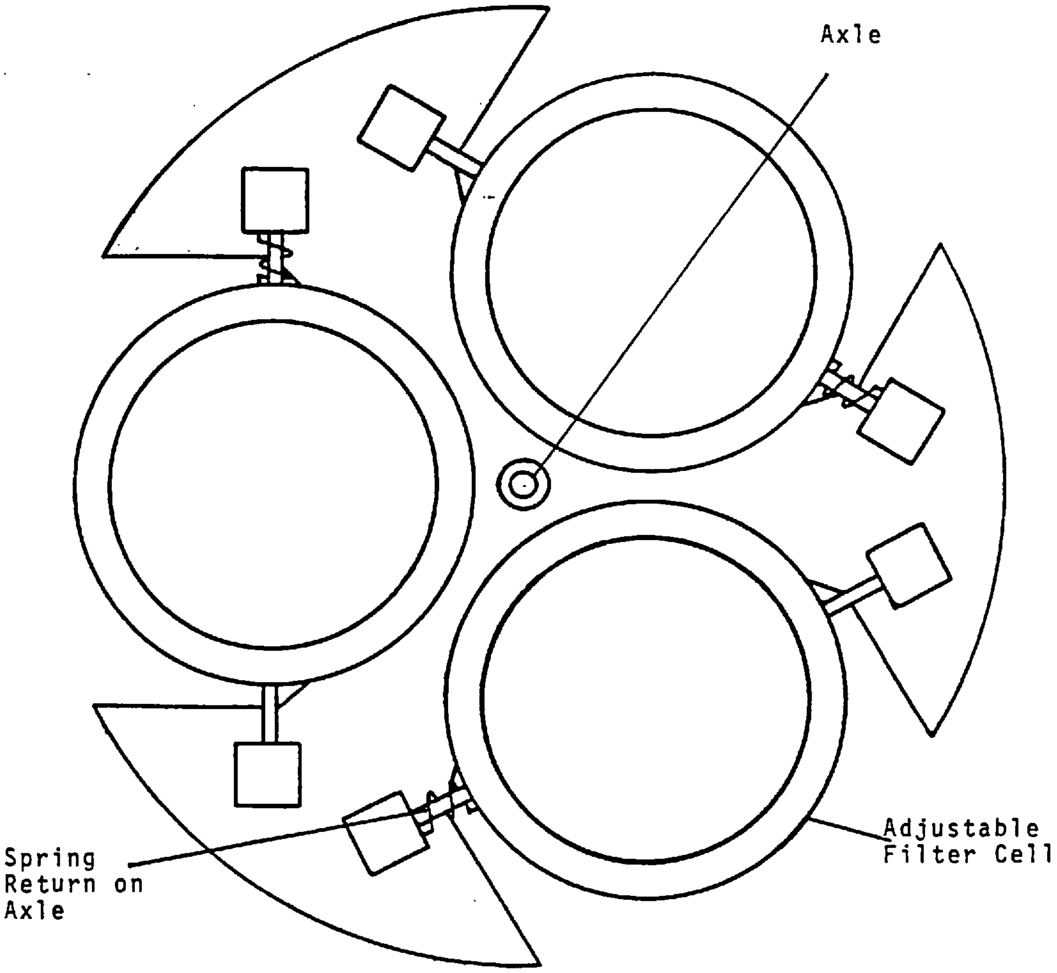

FIG. 2.11 FILTER WHEEL

### 2.8.7 Condenser Lens

The exit lens of the interferometer focussed the collimated beam onto the photo cathode of a photomultiplier tube. In practice, for a single point detector, this image was slightly defocussed, so that the effect of any cathode non uniformities would be reduced. The lens, again plano-convex, was mounted on an Ealing optical electronic shutter.

### 2.8.8 Etalon Design

The use of spacer-less Fabry-Perot etalons at the Cassegrain focus is fraught with difficulties. In particular the change in the orientation as the telescope tracks changes the gravitational load and induces a change in the plate spacing and parallelism.

Typically, a large telescope will be able to track objects to within 10° or 20° of the horizon. This corresponds to a change in attitude of about 160° when tracking on an object that passes through the zenith. The range of a piezo-electric transducer 2.5 cm in length, in the form of a radially polarized cylinder, is about 5μm for ± 1KV applied voltage. If a scanning range of 1μm, corresponding to 4 orders in the green, is required, then 4μm of movement is left to correct any mechanical or thermal drift.

Initially the use of a commercial, thermally compensated lens mount was attempted. This was equipped with differential micrometers for adjustments in X and Y and was mounted on a translation slide. This enabled easy access to the plates and facilitated the setting up of the interferometer, allowing motor drives to be attached to the micrometers so that complete remote control was possible. A diagram of this arrangement is shown in Figure 2.12.

Each plate was mounted in a cell. One cell was mounted in the commercial mount and the other on a piezo assembly (Figure 2.13). The piezo assembly consisted of three large transducers for scanning in gap and three smaller transducers used for correcting drifts in parallelism. A brass bush with a 4BA tapped hole in it was bonded inside each piezo electric cylinder for the purpose of attaching it to a stainless steel ring and also to provide a contact to the inner surface. A fused silica disc with a V-groove polished in the surface was cemented to the top of each piezo stack. These provided a kinematic mount for the sub-assembly, consisting of the small piezos and the interface plate, which were sprung together in the same way. Gold plated sockets were located in insulating bushes around the periphery of the interface plate. To the back of each socket was attached a co-axial cable which carried the 16 Khz signals to or from the ratio arm bridge circuitry. The cells which plugged into these sockets are described in section 2.8.9.

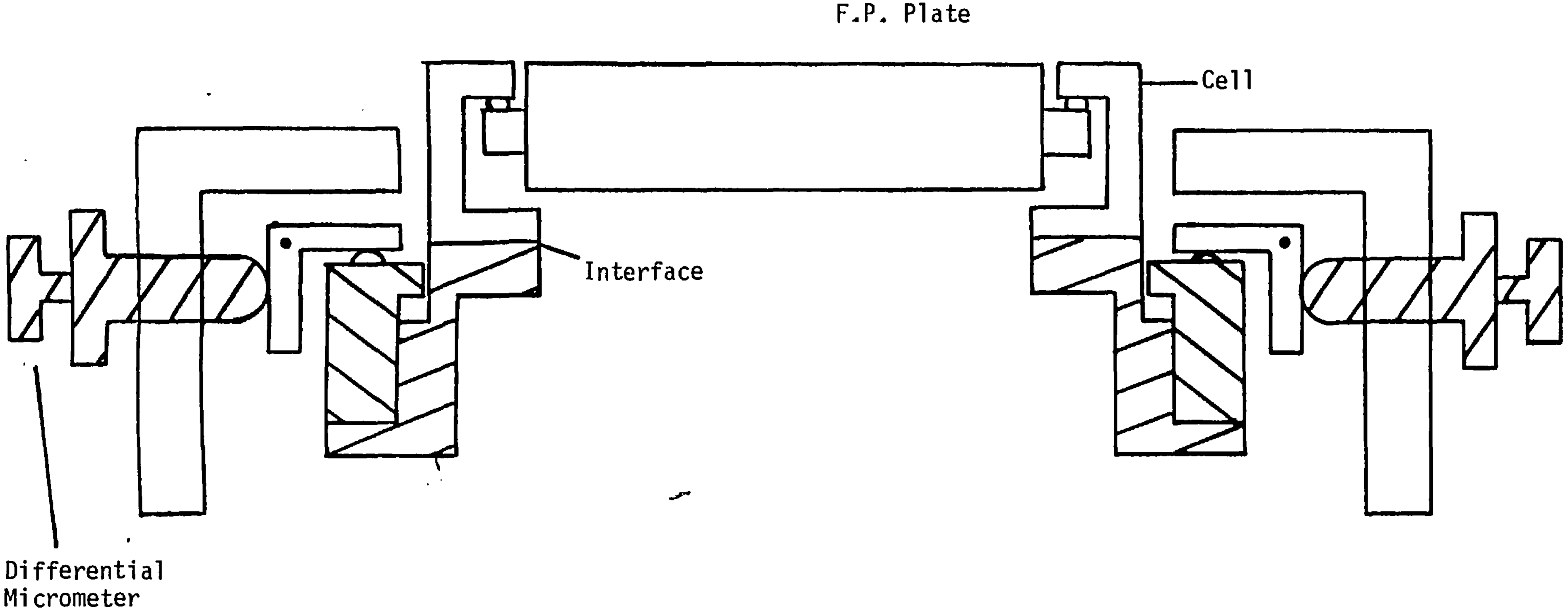

Figure 2.12 Commercial Mount

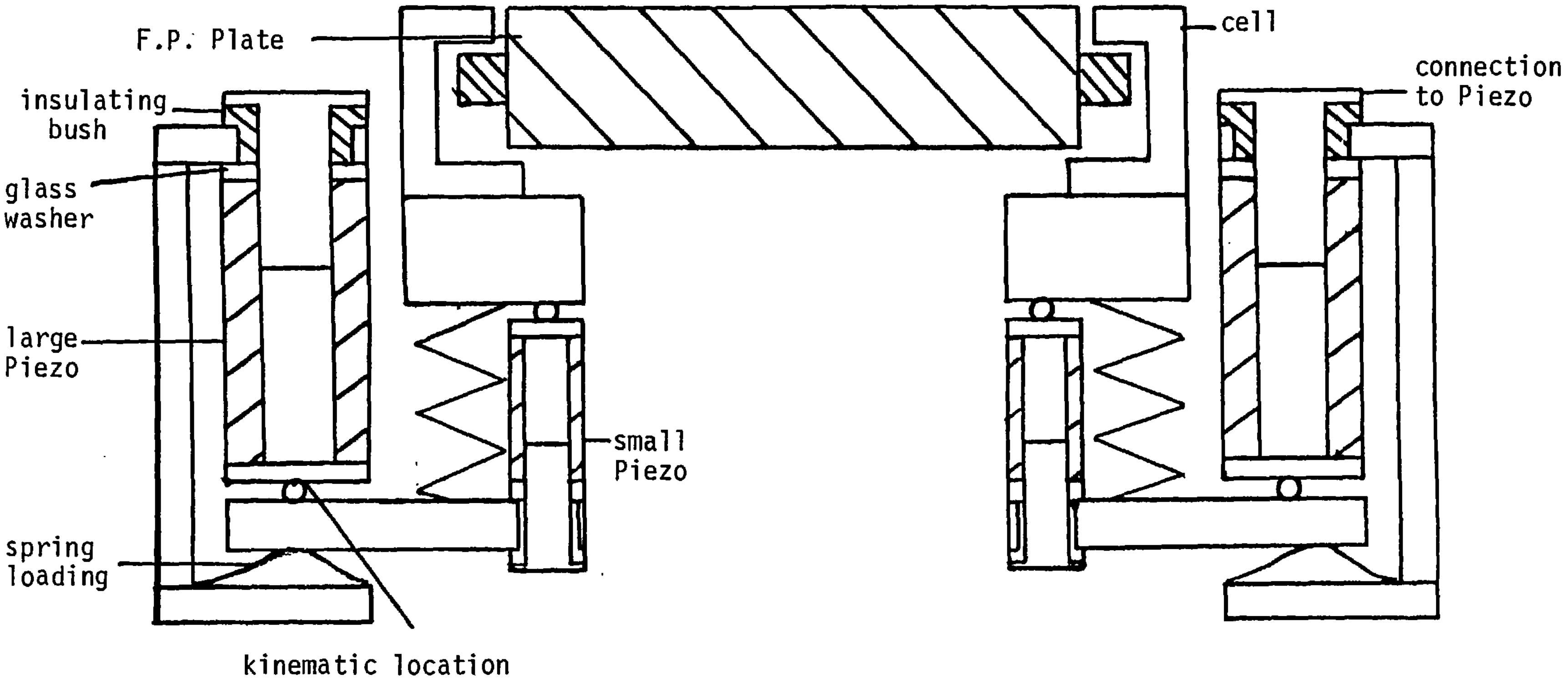

Figure 2.13 Piezo Assembly

The two assemblies were coupled together by a stainless steel baseplate. The size of the etalon prohibited the adjustment of the whole assembly perpendicular to the beam and so adjustments were provided on the piezo-assembly instead. Alignment of the etalon with the optical axis of the telescope, defined by a laser beam, was performed by first aligning the plate on the piezo assembly, using back reflections, and then aligning the second plate parallel to it.

The performance of this etalon assembly proved to be extremely poor. Not only was the mechanical drift, due to changes in orientation, very large, but also the system was highly sensitive to vibration. Light pressure applied to the translation slide induced movements of several fringes.

Various attempts to improve the performance of this arrangement were made: the coupling between the plates was increased; the z-slide was pretensioned by springs to remove the play; the commercial mount was modified and stiffened up considerably. This resulted in a slightly improved performance, but the system was still not satisfactory. For this reason the commercial mount and translation slide were discarded and replaced by the carriage shown in Figure 2.14.

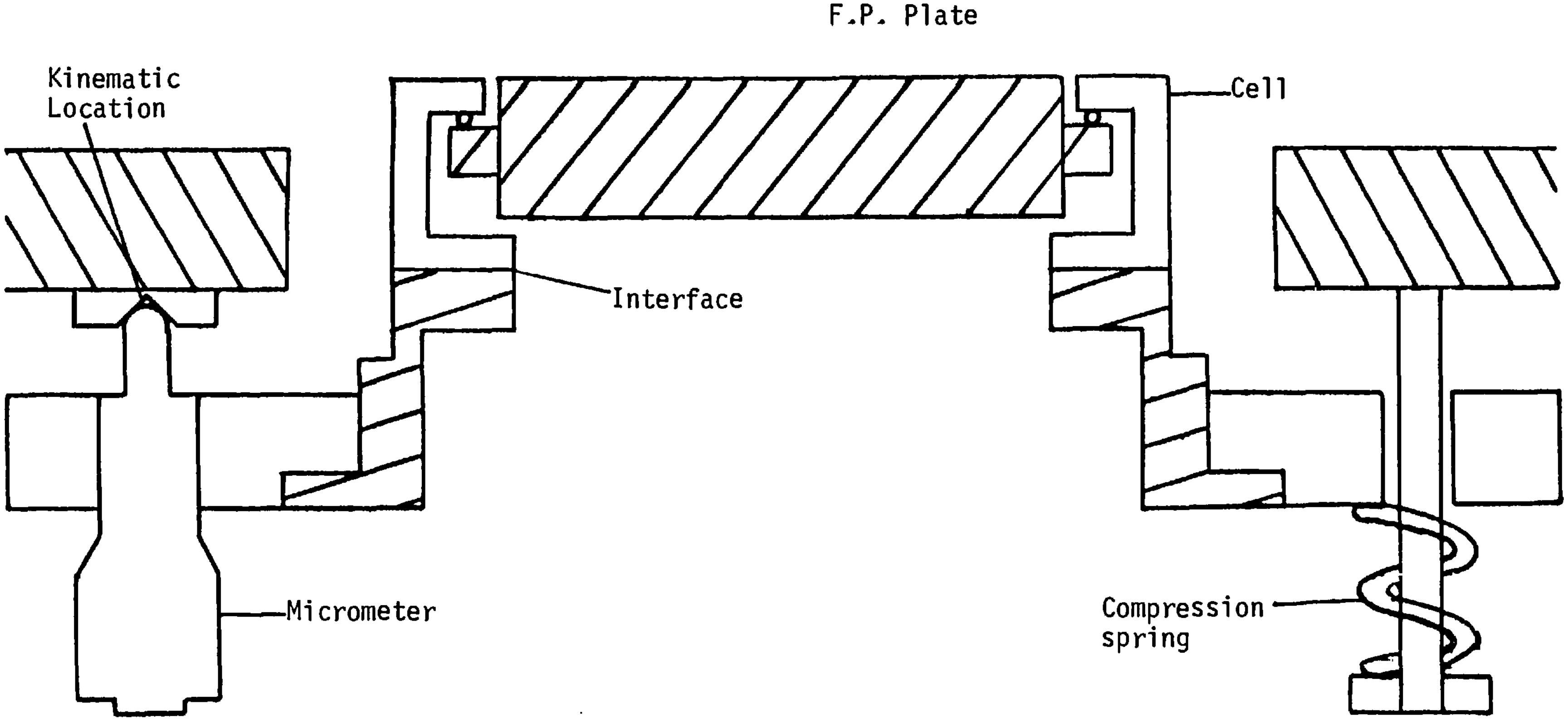

Figure 2.14 Micrometer Carriage

This carriage consisted of a dural ring supported on three ball ended micrometers, mounted orthogonally and locating in radial V grooves milled into a stainless steel plate which was strapped, rigidly, to the plate supporting the piezo assembly. This configuration was much more stable being far less sensitive to either vibration or orientation. Tests performed on the 36" telescope at the Royal Greenwich Observatory in August 1976 showed that the servosystem was capable of correcting the mechanical sag, over a range of about $60^{\circ}$, corresponding to 4 hours observing time.

In order to decrease the residual mechanical sag and decrease the time constant of the assembly, the piezos were attached rigidly to a steel plate at each end. This made the structure highly resonant due to cross-talk between the piezos and they tended to crack under low lateral loads.

### 2.8.9 Cells

Figure 2.15 shows the system used for mounting the plates. Three fused silica lugs, each with a V groove formed in the top, were cemented at 90° intervals around the circumference of the plate. The plate is then located kinematically on ball bearings mounted on a stainless steel ring. Nylon screws are then tightened behind each lug, to ensure that it remains in good contact with the ballbearing.

Connections to the capacitor pads are made within these cells by means of sprung gold strips pressing against gold contacts which are cemented to the side of the plate. On the F.P. plate the connection between the capacitor pad the the gold strip is made using a silver-loaded conducting paint. From the spring strip a connection is made to a gold plated plug. This plug mates with the socket mounted in the interface plate mentioned previously.

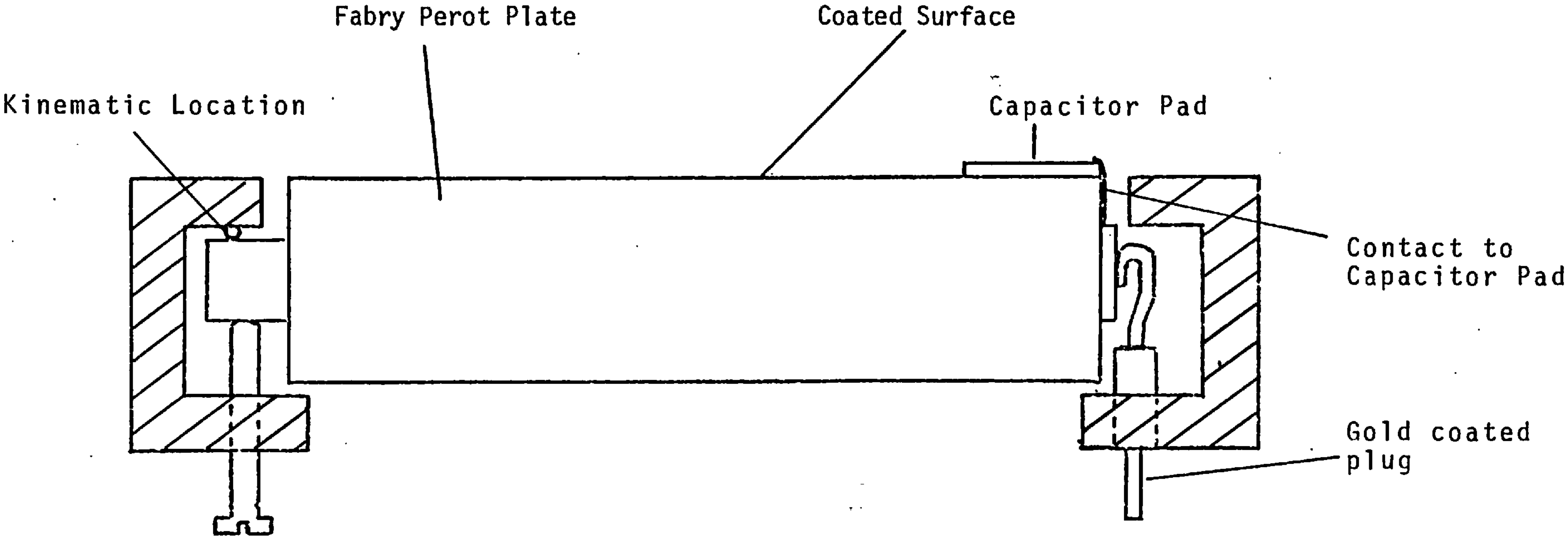

FIG. 2.15 CELL FOR SUPPORTING F.P. PLATE

## 2.9 Construction

The interferometer was mounted in a Dural box measuring 10" square by 34" long. This box was constructed from a frame of ½" square Dural rod with a $^{3}/_{8}$" base plate and $^{1}/_{4}$" sides and top. The top was split into two pieces and easily removable for access.

Two panels were cut in the sides next to the etalon also for access. Facilities for attaching a laser for alignment purposes was provided at either end of the box. The box was mounted on the telescope by means of a large adaptor plate Figure 2.16, which was drilled to suit several telescopes. Figure 2.17 shows a photograph of the interferometer mounted on the 1.5m telescope in Tenerife.

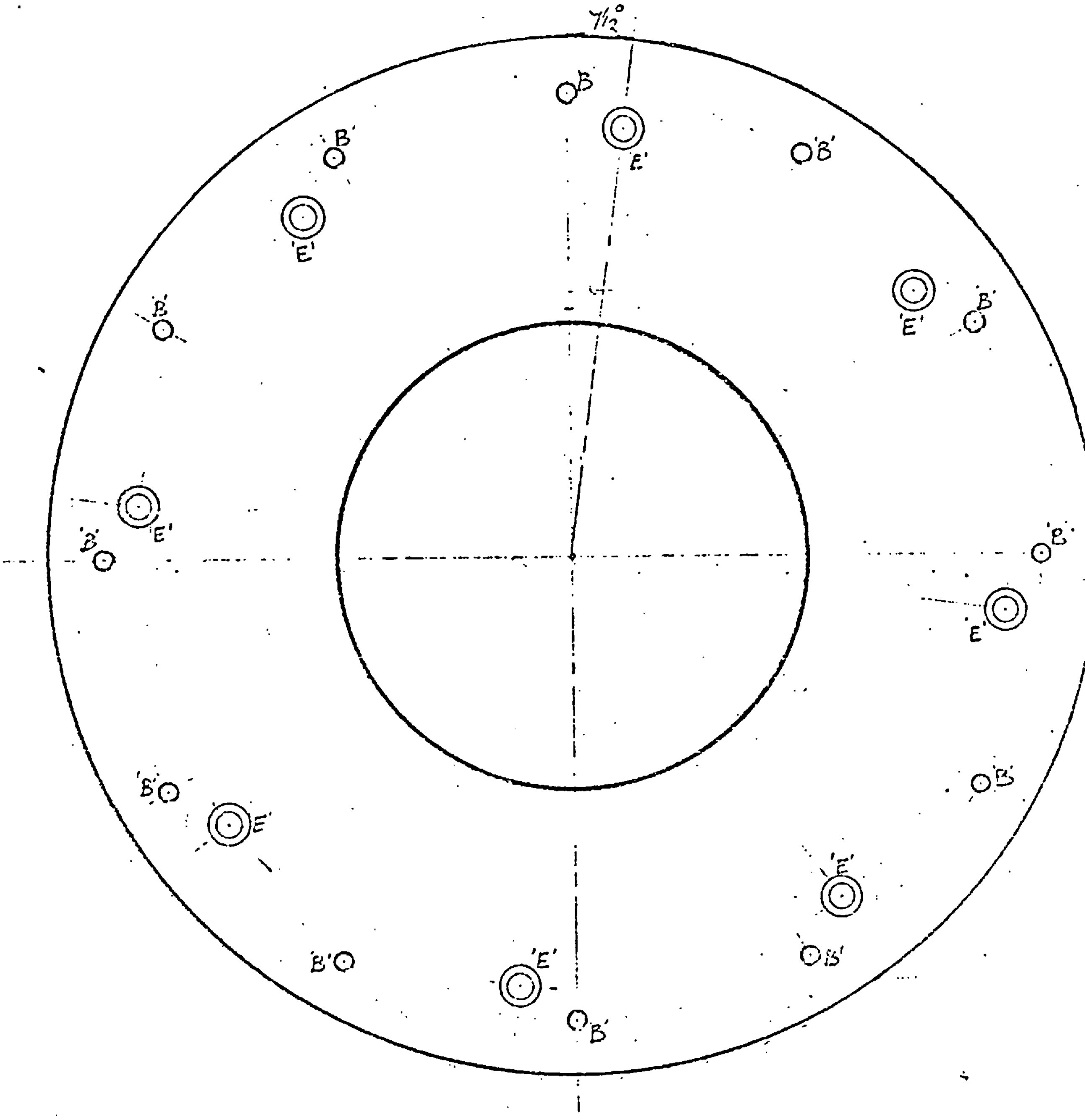

Figure 2.16 Adaptor Plate

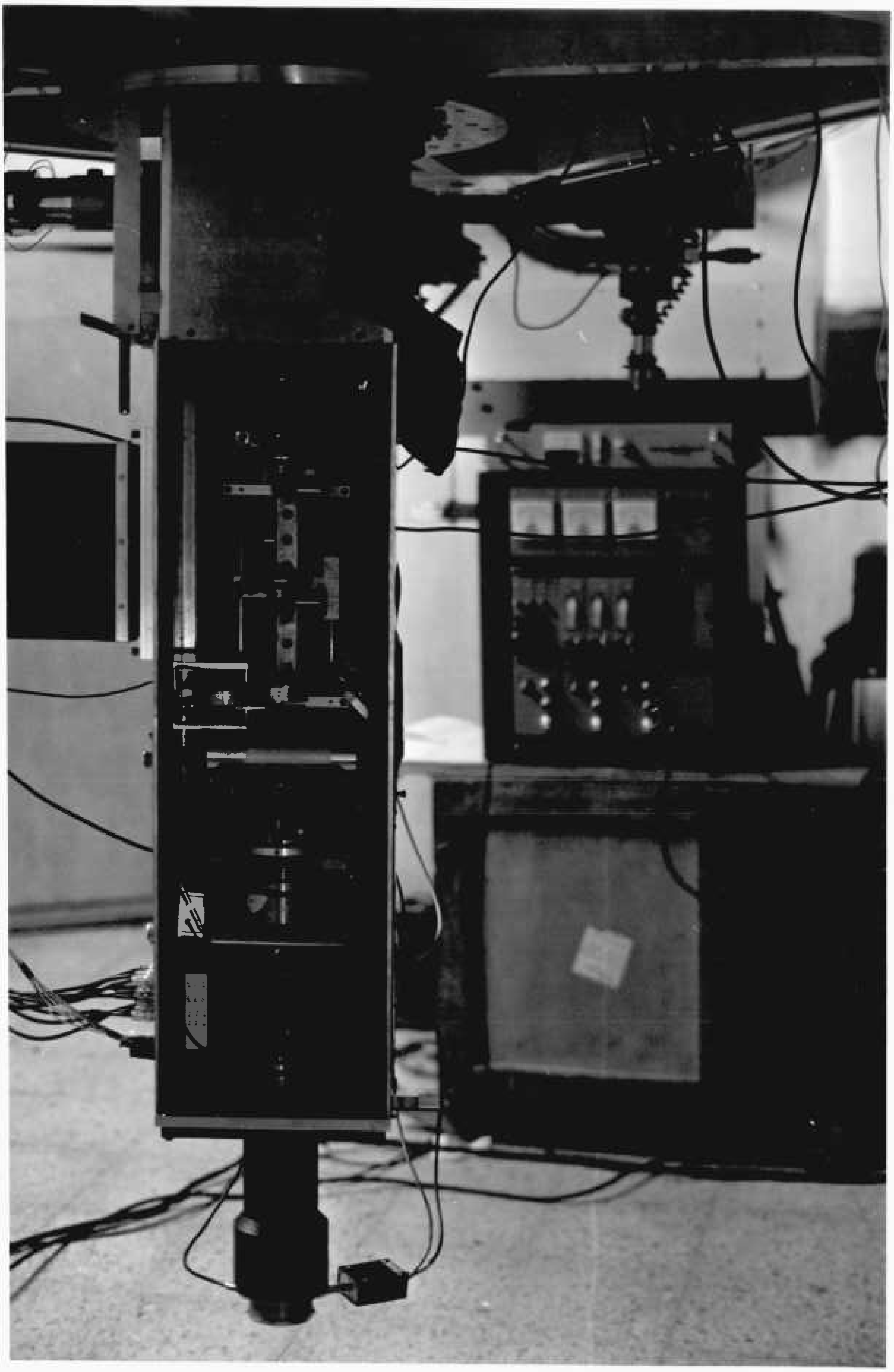

Figure 2.17 The FP on the 1.5 m

## 2.10 Operational Procedure

On arrival at an observatory the setting up of the instrument after its attachment to the telescope proceeded in the following manner.

Initially the optical axis of the telescope was established by means of a laser beam. The laser beam was adjusted until the beam passed through the exit pinhole and was incident on the middle of the secondary mirror, the back reflection being symmetrical about the exit pinhole. In some cases there is a hole in the centre of the secondary mirror and this prevents observation of the back reflection. The entrance pinhole was then adjusted to be on-axis and then the collimating lens, again utilizing back reflections. One of the F.P. plates was then placed in position and aligned almost perpendicular to the laser beam. The entrance pinhole was then uniformly illuminated and the collimating lens was moved along the optic axis until auto collimation was achieved, a clear image of the entrance pinhole being formed adjacent to itself. This image is then superimposed on the entrance pinhole by adjusting the F.P. plate. The second plate is then placed in position and the procedure outlined in section 2.6.2 is followed to set up a servo-ing etalon. The exit pinhole is then removed and replaced by the condenser lens and finally the interference filters are put in. A finesse scan of a line from a hollow cathode lamp, typically Na or Mg, or a laser line, is then performed to check the quality of the alignment.

## 2.11 Calibration

Calibration of the system in wavelength is carried out by the method of exact fractions. Two or more monochromatic light sources are scanned and the position of the interfer at the peak of each line is noted, giving positions $P_1$, $P_2$ ..... $P_i$. The inter-order spacings $I_1$, $I_2$ . . . $I_i$ were also noted. We may then write the following series of equations:

$$2t = \lambda(n_1 + E_1) = \lambda_2(n_2+E_2) \tag{2.44}$$
$$= \lambda_i(n_i+E_i)$$

where $P_1 = E_1I_1$; $P_2 = E_2I_2$; $P_i = E_iI_i$ (2.45)

An approximate value of the gap t is known from the height of the pillar, the value of the reference capacitor and the area of the pads on the plates. Values of n corresponding to this gap may then be inserted into the equations 2.44 and 2.45 and using the values for one line, the corresponding values for the other lines are predicted. Different values of n are then used until a consistent set of equations are obtained. The number of different lines required to establish t increases as the value of t, and hence n, increases. For $t \sim 3$ mms ie $n \sim 10^4$ up to seven or eight lines of accurately known wavelength will be required. For $t \sim 100\ \mu$ M two or three lines should give an unambiguous result.

## 2.12 Performance

The instrumentation was tested on the 36" telescope at the Royal Greenwich Observatory during August 1976. A finesse of 26 was achieved whilst the telescope was tracking and some preliminary scans of various objects were obtained (Figure 2.18).

The finesse was degraded to 23 as the telescope tracked towards the limiting range of the piezos. This was traced to low gain in the servo-electronics. In general the servo-system will reduce any offset introduced by a factor M, the open loop gain. Thus an offset x will be reduced to $^x/_M$. The value of M was measured to be approximately 120, so that a mechanical drift of 5 fringes in the visible would be reduced to

$$5.\frac{\lambda}{2} \cdot \frac{1}{120} = \frac{\lambda}{48}$$

Clearly to remove this problem, either a decrease in the mechanical drift or an increase in the open loop gain is required. An upgraded version of the servo-electronics has now been constructed which has an open-loop gain of 50,000. In the interim the gain of the old electronics was increased to about 500.

## 2.13 Vibrations

After initial tests on the 36" had proved the viability of the instrument, observing time was obtained on the 1.5m flux collector in Tenerife, for a period of fourteen nights in December 1976.

The presence of vibrations, originating from the R.A. stepping motor drive and passing through the worm gear-box to the worm wheel, reduced the operational finesse to about 12 when operating at 100μ capacitor gap. These vibrations induced oscillations of the F.P. plates of an amplitude sufficient to blur the visible ring pattern. In addition vibrations of an even larger amplitude were induced by the declination drive stepping motor. Attempts to increase the frequency response of the servo-system by decreasing the time constant, were thwarted by the resonant structure of the etalon which caused the system to oscillate when too short a time constant was selected.

An investigation of the nature of the vibrations revealed a tendency for the amplitude to change sinusoidally with time. The F.P. was scanned, repeatedly, through the peak of the Mg5183A$^{o}$line. The resultant chart recorder trace is shown in Figure 2.18. Clearly the height and width of the profile varied with time. This variation could be attributed to a misalignment of some sort of the worm gear

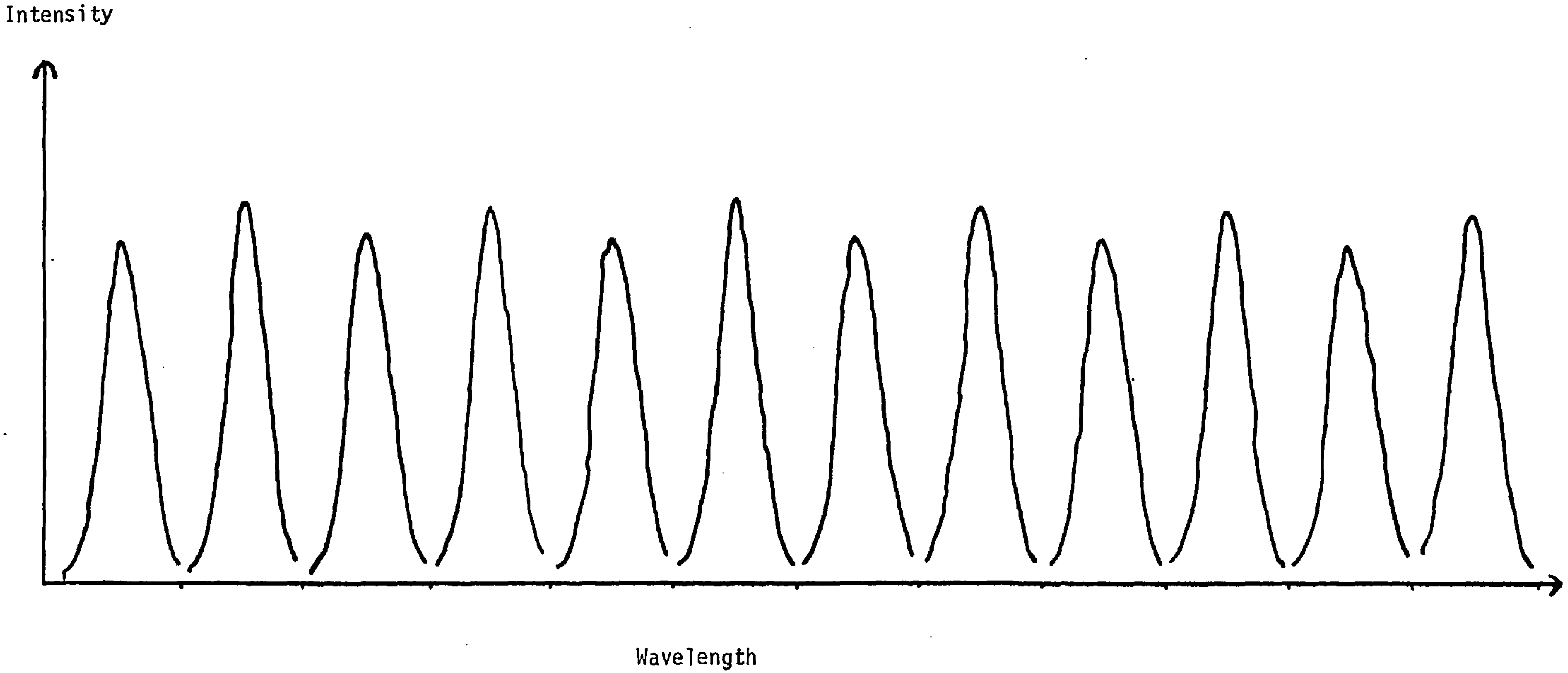

Figure 2.18 Vibration Variation

with respect to the wheel.

Visual inspection of the fringes from a Zn lamp whilst servoing indicated that the etalon was responding to a frequency of a few Hz, although this could have been demodulated from a higher frequency carrier wave.

Several independent paths were available for the vibrations from the stepping motor to the Cassegrain focus, the contribution from any particular one being unclear. Partial isolation of the stepping motor from its mountings were attempted with little success. Attempts to create other resonant systems in the path or next to the interferometer, to divert some of the energy of the vibration and hence reduce the amplitude induced in the F.P. also failed. It was found impossible to decouple adequately any part of the system using the tools available.

## 2.14 Vibration Isolation

### 2.14.1 Theory

The principle of isolation from vibration has been stated by Crede (1951).

> "To mount the equipment upon resilient supports or isolators in such a manner that the natural frequency of the equipment and isolator system is substantially lower than the frequency of the vibration to be isolated."

The transmissibility of a system (T) is defined as the ratio of the transmitted force to the applied force. This transmissibility varies according to the ratio of the driving frequency (f) and the natural frequency ($f_o$) of the system in the following manner.

$$T = \frac{1}{1-(f/f_o)^2} \qquad (2.46)$$

A graph of T versus $f/f_o$ is shown in Figure 2.19 for various values of damping.

For a system executing simple harmonic motion it is possible to relate the natural frequency $f_o$ of the system to the static deflection x of the system under gravitational load.

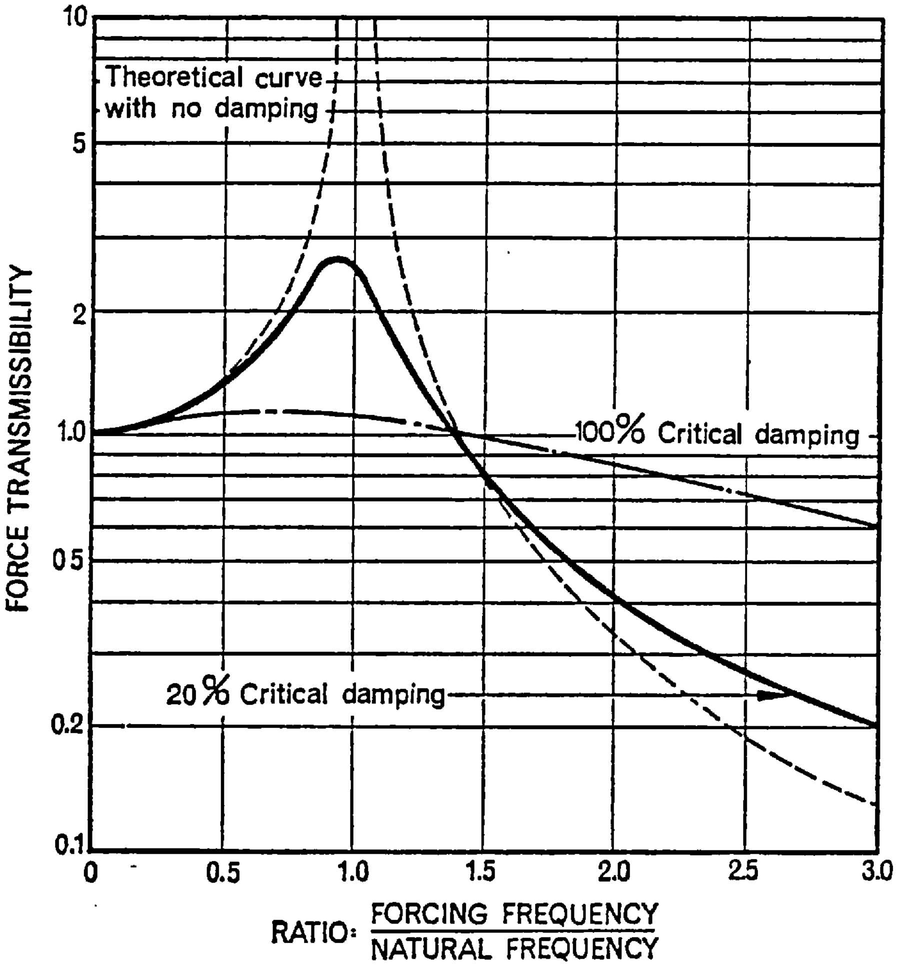
10
5
2
1.0
0 5
0.2
0.1
FORCE TRANSMISSIBILITY
Theoretical curve with no damping
100% Critical damping
20% Critical damping
0
0.5
1.0
1.5
2.0
2.5
3.0
RATIO: FORCING FREQUENCY / NATURAL FREQUENCY

Figure 2.19

From Hookes Law

$$F = sx \qquad (2.47)$$

In equilibrium we may write

$$mg = sx \qquad (2.48)$$

For a system executing simple harmonic motion

$$f_o = \frac{1}{2\Pi} \sqrt{s/m} \qquad (2.49)$$

Combining 2.49 and 2.48

$$f_o = \frac{1}{2\Pi} \sqrt{g/x} \qquad (2.50)$$

The static deflection is a convenient parameter as it describes the deformation required for a certain natural frequency.

Combining equations (2.46 and (2.50) we may obtain an expression for the efficiency of isolation of a system, at a particular driving frequency, as a function of the static deflection

$$T = \frac{1}{1 - \frac{4\Pi^2 x f^2}{g}} \qquad (2.51)$$

A graph of T vs x is shown in Figure (2.20). Thus it is possible to assess directly the static deflection required for a given efficiency of isolation at a given frequency.

### 2.14.2 Practice

Clearly the price of isolation of vibration is the sacrifice of any rigid coupling between the F.P. plates and the telescope.

It was decided to introduce the isolators around the etalon itself, decoupling it from the box, as this was structurally the simplest place. As the telescope tracks, the load on the isolators changes and the orientation of the etalon will change with respect to the optic axis. This tends to scan the passband and change its shape and width. This effect may be reduced to a minimum by ensuring that the plane in which the isolators are attached to the etalon contains the centre of gravity of the etalon assembly. In this configuration there is no change in the relative torque on any of the isolators with charges in the attitude of the telescope, and thus no charge in the orientation of the etalon. There may however be a lateral shift of the etalon.

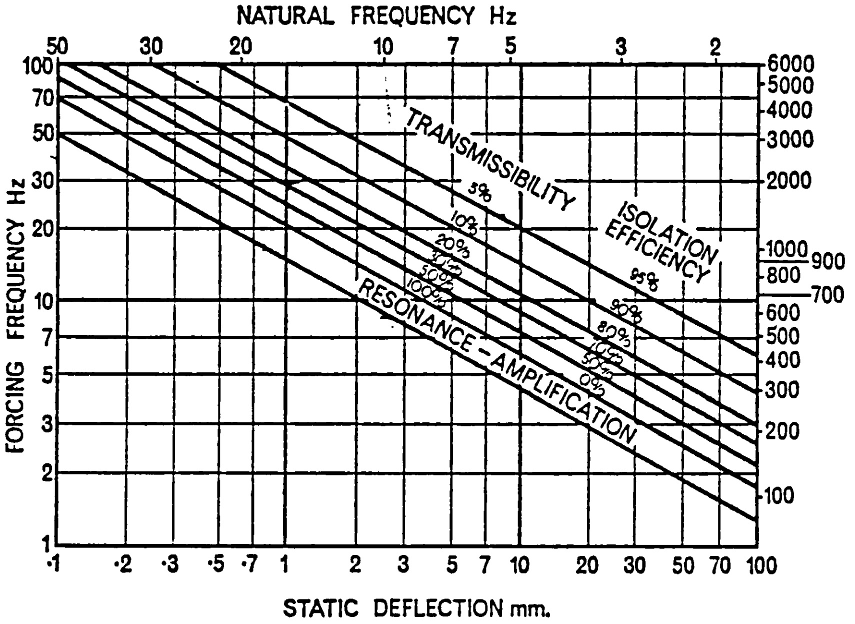

Figure 2.20 Vibration Transmissibility

The centre of gravity of the etalon assembly was determined roughly by suspending it from three different points and locating the intersection of the vertical lines produced through the point of suspension. In operation the position of the centre of gravity could be 'tuned' to the correct position by the addition of small weights.

The stiffness s of an isolator is different in the lateral shear mode to the longitudinal compression - tension mode. Thus a particular configuration of isolators and equipment will have different characteristics of response to longitudinal vibration than to lateral vibration. For the case in question it seemed most likely that the higher frequencies present in the noise at the Cassegrain focus were of the longitudinal mode: that is parallel to the optical axis of the telescope.

The arrangement used is shown in Figure 2.21. Commercial anti vibration mounts or isolators were purchased, consisting of a screw thread bonded to each end of a rubber cylinder. These were chosen to have a shear stiffness of 52 lbs per inch giving a static deflection of approximately 0.1 inches or 2.5 mm. This corresponds to a natural frequency of about 10 hz, giving progressively better efficiency of isolation as the driving frequency f increases above this value, according to Figure 2.20.

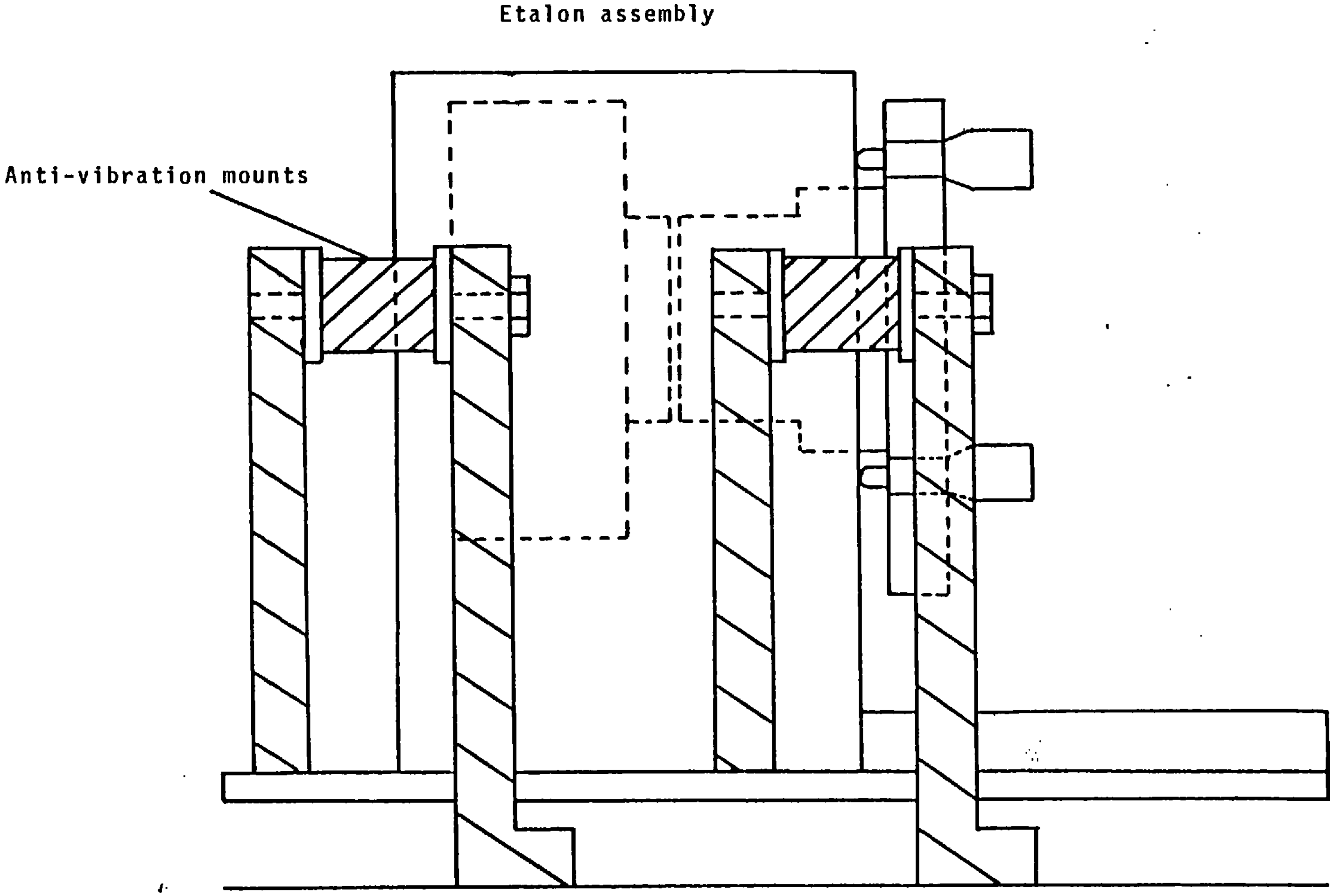

FIG. 2.21 ANTI-VIBRATION MOUNTING ARRANGEMENT

### 2.14.3 Performance

The modified instrument was tested on the 1.5 m Flux collector in Tenerife in February 1977. The equipment was damaged in transit, necessitating the replacement of the small piezo-electric transducers with steel pillars, and a reversion to the coordinate transformation system using the three larger transducers.

It was immediately apparent that the vibrations had been isolated as finesses of up to 35 were obtained, with $N_R = 42$, with the R.A. drives on. The lateral movement was such that slight vignetting of the beam occurred at the extremes of movement. The ratio of the lateral movement of the F.P. to its angular movement was indicative of the quality of the mounting frame, maintaining finesse whilst allowing sufficient sag to ensure efficient isolation.

The efficiency with which the vibrations had been isolated indicated that the exciting frequencies were fairly high compared to the natural frequency of the assembly, and leading to the possibility of increasing the stiffness of the isolators and decreasing the mechanical sag and tilt of the etalon assembly without degrading the performance.

# CHAPTER 3: DATA ACQUISITION AND REDUCTION

Data has been acquired from two separate systems: the servo-controlled F.P. discussed in Chapter 2, and a piezo-scanned F.P., mounted at the Coudé focus of the 88" telescope on Mauna Kea, Hawaii, known as S.P.I.F.I.

The acquisition system used for the servoed F.P. will be discussed followed by a brief description of S.P.I.F.I. and the translation and preliminary reduction of the data acquired from it. A comparison of the different reduction problems and the quality and consistency of the data is made, followed by a description of the general reduction techniques.

## 3.1 Introduction

It is the function of the Data Acquisition system to enable the observer to set up a scan of x points in increments of s steps covering y Angstrom units with integration times of t seconds, where x,s,y and t are all variables, and to record the data acquired. Preferably some kind of display will be provided, be it a chart recorder, oscilloscope or visual display unit, to allow a degree of interaction with the data. There may also be some remote control of the ancillary devices involved in the calibration of the system.

## 3.2 Data Acquisition

### 3.2.1 I.C. Data Acquisition System

Effectively, two separate systems exist: a back-up system consisting of a Brookdeal SCl photon counting system and logic control unit, and a system based on computer control through CAMAC. These systems are shown diagrammatically in Figure 3.1.

Photo electron pulses from the photo-multiplier are amplified by an ORTEC X10 preamplifier and sent down a long co-axial cable to the Brookdeal, where they are selected by discriminators and counted. When the system is under computer controls the output of the discriminators is fed into a CAMAC scaler module. The integration time is set by an internal clock in the Brookdeal, or by using the PRESET COUNTER module to 'gate' the scaler. At the end of an integration, in the back-up mode, a pulse is sent back to a programmable logic unit, which advances the F.P. to its next position by feeding a number into a digital to analogue converter, the output voltage of which is fed into the z channel of the capacitance bridge as an offset. In the computer control mode this number is supplied through the I/O register in the CAMAC rate.

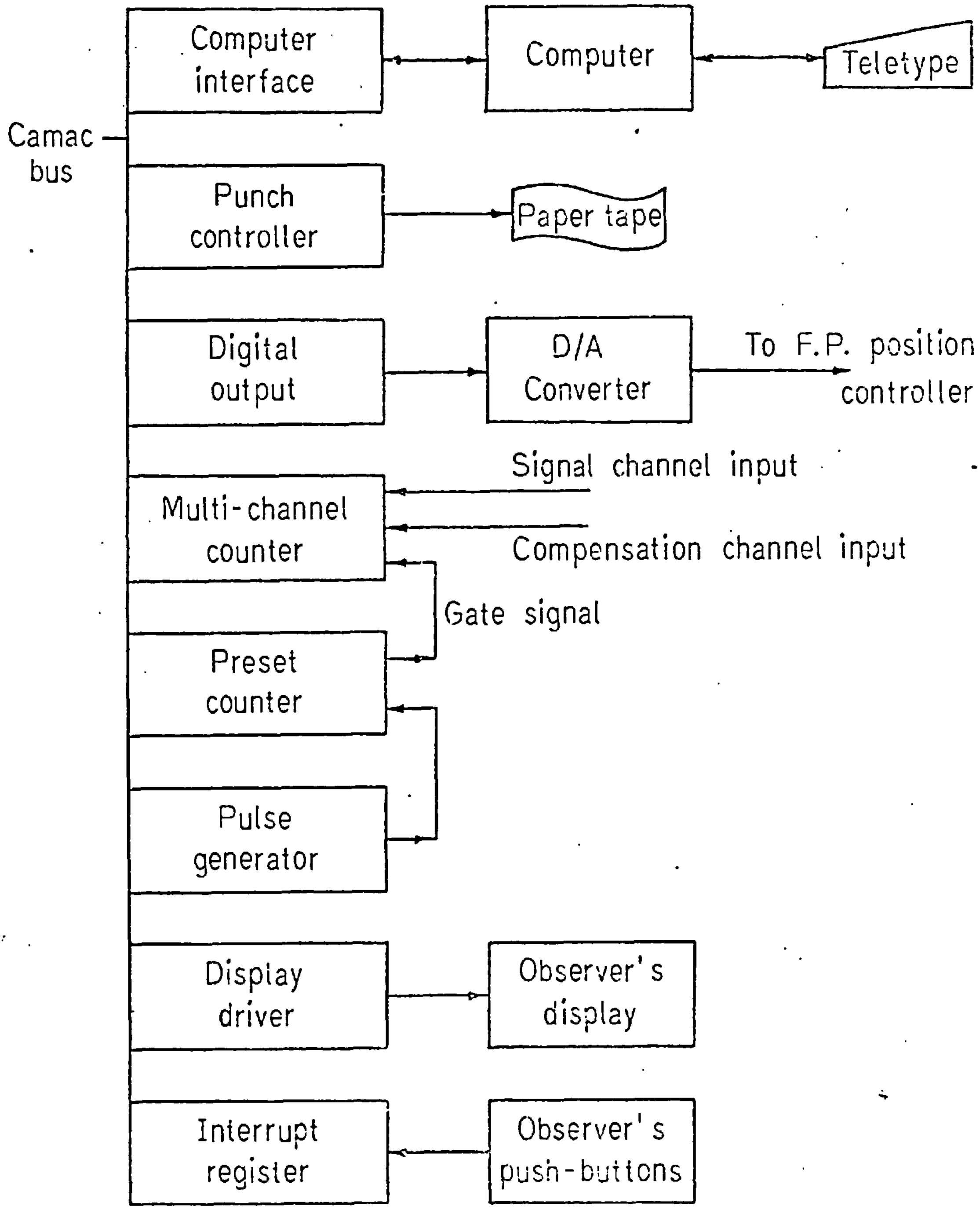

Figure 3.1 Data Acquisition System

The scanning range is divided into 256 steps, each of which is addressable using an 8-bit binary number. A scan may be programmed by specifying the stop number at which the scan is to commence (FPST), the step increment (FPINC) and the total number of sample points (NPTS). The back-up programmable logic unit provides also an automatic 'repeat-scan' facility, as well as the ability to pause or abort during a scan. In the computer control mode these facilities are supplied on user-programmable buttons located on the computer.

The data is recorded on papertape, the count for each point being punched at the end of the integration time. In the back-up mode the data is displayed on a chart-recorder, using the analogue output of the Brookdeal. Under computer control a real time display of the scan is possible as well as displays of the compensation channel or the co-add array. This display is updated at the end of each sample point. An additional facility available under computer control is that of rapid scanning, where the integration time may be as low as 5 msecs per point. The limiting speed is set however by the BASIC interpreter, which takes up to 50 m secs to process each instruction. For data acquisition the rapid scan mode has the advantage of removing the effects of slow changes in signal strength during a scan. However when the integration time is equal to the time taken by the computer to output the next instruction, only 50% of the time is being used for observation and rapid scanning becomes inefficient. This time varies according to the operating system and the computer language being used, and could be drastically reduced if the routines were written in Assembler or a lower-level language.

#### 3.2.1.1 Preliminary Processing

In conditions where the signal strength fluctuates a second channel is employed to monitor these fluctuations. This channel is called the compensation channel and measures the total incident flux just before the premonochromator by reflecting a small percentage of the light from a microscope slide in the beam into a photomultiplier. This provides a measure of the quality of the data. This value is recorded on paper tape as a count following each signal count. The paper tape formats, although at the discretion of the user when under computer control, are typically of the following form.

Each scan is allocated a number (NSCAN) which is the first number on the tape. This is followed by the scan parameters: FPST, FPINC, NPTS, and these are followed by alternate signal counts and compensation channel counts. Under computer control the facility to co-add scans of the same position as an object is available. This co-add array is stored in the core memory of the computer and may be displayed on a VDU whilst a scan is in progress, or chopped with a recently acquired scan to compare the data and note any changes in the shape of the profile. This feedback enables the observer to assess the relevance and importance of a particular observation and is significant in increasing the efficiency of the acquisition process.

Paper tapes created by the back-up system are of a set format, determined by the Punch interface, and need to be translated into a form compatible with the CDC 6500 computer available at Imperial College. This translation is performed using an Interdata 70 computer. At this stage the opportunity is taken to add further information from the observing log which is not already present and which is used by the reduction package described later. Thus up to 80 characters of text information describing the object, the position of the object, the size of the entrance aperture and the observing site are inserted after the scan parameters. The scan parameters are also increased to include the date and time of observation, the total integration time, and the sample time. Paper tapes generated by the computer may already have most of this information present on them but still need to be translated on the Interdata owing to differences in the character set. Coadding of various scans is also performed at this stage, prior to the production of a paper tape compatible with the I.C. computer system.

### 3.2.2 S.P.I.F.I.

The system known as SPIFI was developed by Professor W.H. Smith of Washington University, St. Louis and is described in Smith et al 1976.

A diagram of the optical system is shown in Fig 3.2. The system consisted of a piezo scanned Burleigh Instruments Fabry Perot etalon and associated scanning electronics, coupled to a control system comprising a magnetic tape drive, a chart recorder, real time data display and the facility to control remotely the various lenses and calibration lamps available.

Guiding was performed using light reflected from a front surfaced mirror with a hole in it corresponding to 6 or 10 arc secs. This rendered guiding somewhat imprecise, as the observer was required to judge and maintain the positioning of the object from the beginning to end of a scan. However the superb tracking of the telescope made this procedure adequate. Slight variations in the profile are found from scan to scan, indicating slight drifts in position. These effects

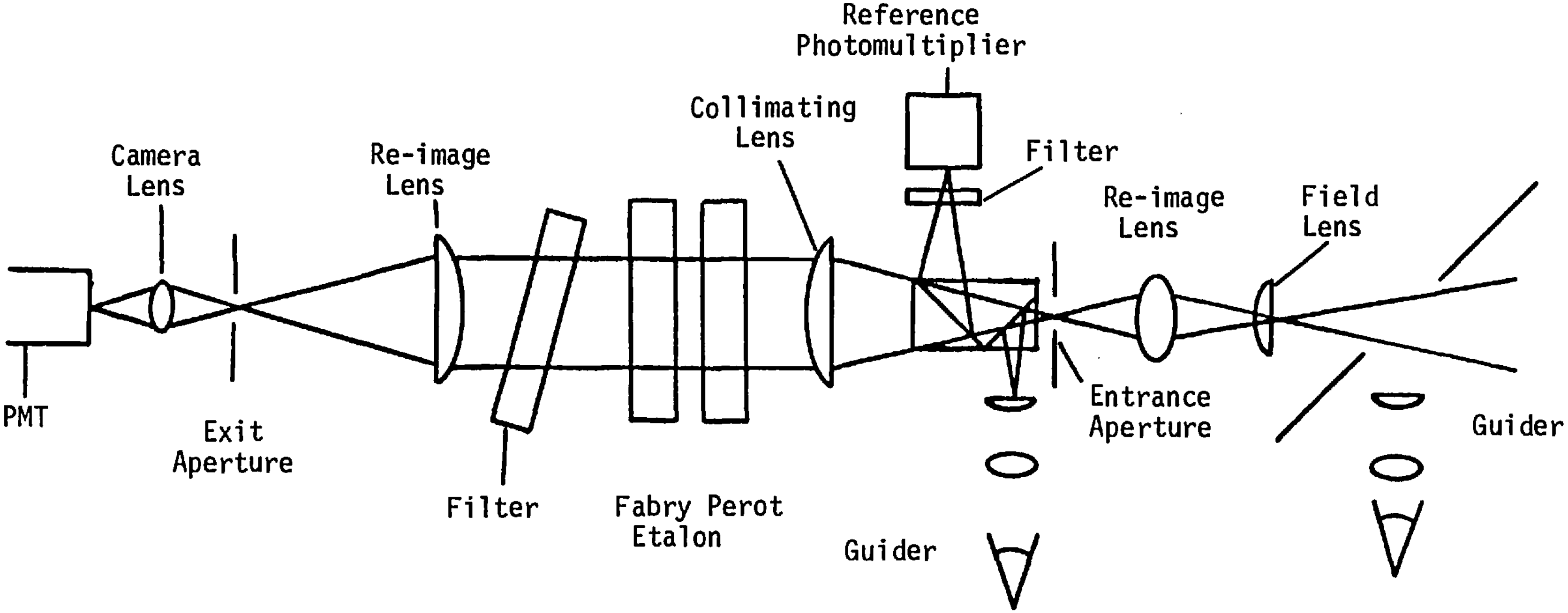

Figure 3.2   S.P.I.F.I.

were not so serious on the larger objects studied, where drifts of 1-2 arcsecs represented a much smaller fractional part of the size of the nebula.

Premonochromation was accomplished using a diffraction grating, ruled at 1800 lines/mm and mounted in a modified Czerny-Turner arrangement. The size of the grating limited the area on the sky to about 10 arcsecs diameter, with a profile halfwidth of about 5 $A^{O}$. The grating position was calibrated, enabling the isolation of any emission line with ease.

The detector consisted of a photomultiplier tube, typically an RCA C31034 with a Ga-As photocathode, mounted in a Peltier cooled housing and coupled to a photon counting system.

The system was capable of operation in two different modes:

1) Multi Channel

The mode of operation used when observing astronomical objects was the multi channel mode, in which the etalon was scanned very rapidly and the data coadded into a multi channel analyzer array. An integration time of between 13 msecs and 23 msecs per point was used and approximately 300 - 600 sweeps were made per total scan. The contents of the multichannel analyzer could be displayed on an oscilloscope in real-time, so that one could watch the build up. This mode has the advantage of removing the effect of fluctuations in transparency across a scan.

### 2) Experimental Counter

The second mode of operation was used to record calibration scans. These scans were made in the usual way, with only one sweep per scan and a longer integration time per point, depending upon the brightness of the calibration source.

These two modes use different parts of the data word to store the information. At the end of each scan a leader word, followed by a series of data words corresponding to each sampling point, was written onto magnetic tape. Following this a tracing of the scan was made on the chart recorder.

### 3.2.2.1 Preliminary Processing

The reduction of this data was severely complicated by the incompatibility of the 9-track magnetic tape structure, with the 7-track systems presently employed at Imperial College. The tape was translated into a compatible form by Dr J.D. Argyros, using the system at University College, London.

The tape format is shown in Fig 3.3(a) and contains a great deal of information. It will be noticed for instance that the time to the nearest millisecond is given for every data point. However the clock used to derive this information was totally unreliable and subject to large jumps in time and also changes in speed. Thus a large part of this information is redundant. Furthermore, the number of points in each scan given in the leader word did not correspond to the number of points on the file, as the system showed a tendency to add the first fifteen to twenty sample points on to the end. Further problems included the representation of the count from the multichannel analyser bin as binary information in the middle of a data word written in hexadecimal.

SPIFI Data Word Format

(a)

| | | | | | | | | | | |
|---|---|---|---|---|---|---|---|---|---|---|
| B | HR. | MIN. | SEC. | MSEC | FILTER | POSITION | EXPT. | MULTI | REF. | E |

I.C. Tape Formats

(b)

| | | | | | | | | | | | |
|---|---|---|---|---|---|---|---|---|---|---|---|
| Scan No. | FPST | FP INC. | NPTS | TIME INC. | INTEG. TIME | YEAR | MTH. | DAY | HR. | MIN. | SEC. |

| |
|---|
| Text Information (80 characters) |

| |
|---|
| Y(1), Y(2), Y(3), Y(I) |

Figure 3.3 Tape Formats

To cope with these problems a conversion routine was written to read the data off the tape and transform it into a format compatible with the data reduction package described in section 3.4.4. This routine generates information in the format shown in Fig 3.3(b).

In order that separate scans of the same object could be stacked together a routine was written to shift all the scans such that the calibration line appeared at the same step position for each.

## 3.3 Comparison of Systems

It is interesting to compare the two systems in terms of their observational efficiency and the quality of the data acquired.

### i) Observational Efficiency

Analysis of the observing logs indicates that of the time spent set on an object, approximately 30% of the time was spent in calibration procedures with the SPIFI, whilst less than 20% was spent with the servo-controlled system. These figures are distorted by the fact that whilst for SPIFI the calibration system was entirely automatic, for the servo-controlled system it was rather crude and hence time-consuming to set up.

The settling down time of the SPIFI system after a realignment was around two days, preventing the changing of the etalon plates during an observing run, unless greater drifts from scan to scan were acceptable. For the servo-control system the etalon plates could be changed in approximately 30 mins.

### ii) Quality of Data

With the sophisticated automatic calibration system and by temperature controlling the system drifts in the interferometer passband amounted to $\gtrsim 0.5$ of the full width at half maximum of the instrumental profile from scan to scan. The rate of drift corresponding to 2 F.W.H.M of the instrumental profile per hour. This compares to approximately 0.2 F.W.H.M. for the servo controlled system over periods of up to several days.

## 3.4 Data Reduction Techniques

### 3.4.1. Representation of the Instrumental Profile

Although the instrumental profile of a Fabry Perot is theoretically an Airy function, in practice it is modified by the presence of micro defects on the plates, spherical bowing and the finite size of the entrance aperture. Hernandez (1966) has treated this problem and derived an analytic function representing the convolution of the functions describing these effects, which consist of a Gaussion and two rectangular functions, respectively:

$$P = A \; 1+2\sum_{n=1}^{\infty} R^{n} \exp(-\Pi^{2}n^{2}G^{2}) \, \mathrm{sinc}(nt) \, \mathrm{sinc}(nd) \cos 2\Pi nx$$

where t is the width of the rectangular bandpass defined by spherical defect

d is the width of the rectangular bandpass defined by diaphragm in units of the free spectral range

A is the amplitude

R is the reflectivity

G is the half width at $^{1}/_{e}$ of maximum in units of the free spectral range of the Gaussian describing instrumental errors

Caplan (1972) has described the application of this function using the Gaussian component to represent the thermal Doppler profile and fitting the function to an observed line profile.

Thus an observed profile may be represented as:

$$N(x) = A_1P'(x-x_1) + C \tag{3.2}$$

for a single experiment, or as

$$N(x) = A_1P'(x-x_1)+A_2P'(x-x_2)+C \tag{3.3}$$

for a double profile.

Smith and Weedman (1970) found that their instrumental profile differed very little from a Gaussian in form. This allowed them to determine the intrinsic width of the line profile using

$$a^2_{\text{intrinsic}} = a^2_{\text{observed}} - a^2_{\text{instrument profile}} \tag{3.4}$$

where a is the full width at half maximum.

In this case the instrumental profile was typically one third of the intrinsic line width, and thus the error introduced by the approximation was insignificant.

Figure 3.4 shows a typical instrumental profile compared with a Gaussian of the same height and halfwidth. Clearly the instrumental profile has much higher wings than the Gaussion. For the purpose of removing the Doppler broadening

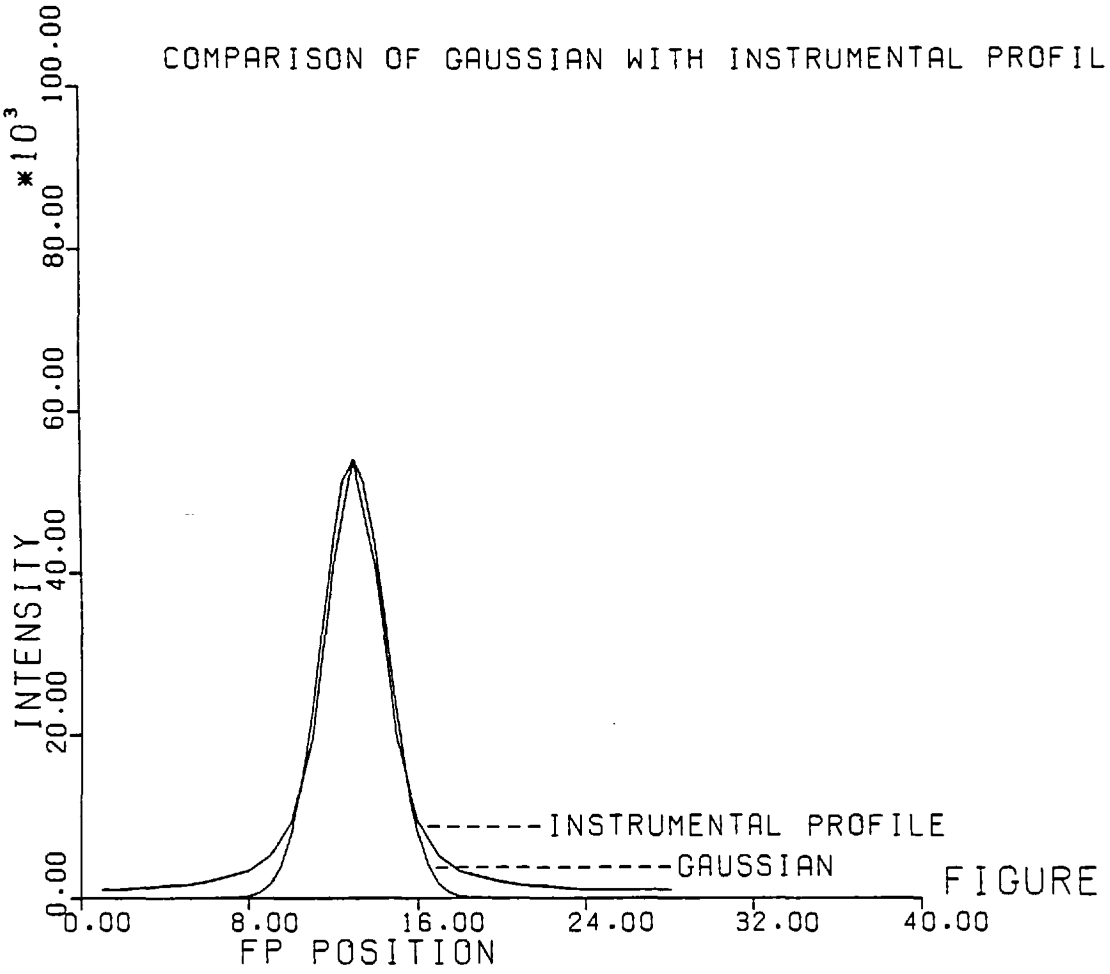
COMPARISON OF GAUSSIAN WITH INSTRUMENTAL PROFIL
INTENSITY
*10³
0.00
20.00
40.00
60.00
80.00
100.00
0.00
8.00
16.00
24.00
32.00
40.00
FP POSITION
------INSTRUMENTAL PROFILE
------------GAUSSIAN

FIGURE 3.4

of a line, these differences only become significant when the width of the instrumental function is comparable to that of the observed profile.

### 3.4.2 Deconvolution

Another method sometimes used to remove the broadening effect of the instrumental function is that of deconvolution. This is normally carried out by dividing the Fourier transform of the data by the transform of the instrumental functions and retransforming. However this technique has serious limitations: the signal to noise on the data needs to be very high otherwise the presence of noise of a high spatial frequency can introduce violent spurious oscillations in the deconvolved profile.

This can be suppressed by smoothing the data to remove any high frequency components. However the number of apparently resolved features deconvolved in this way is a strong function of the way in which the smoothing is performed, ie on the character and width of the smoothing function, judicious choice of the correct smoothing function allowing one to choose the number of components to be present. Clearly this is unsatisfactory and for this reason the method is not generally used: rather the problem is tackled from the other direction, the theoretical profile being convolved with the instrumental profile before comparison with the data.

An iterative technique for limiting the spatial frequency over which the deconvolution is performed has been proposed by Taylor (1974) which removes the subjective choice of the smoothing function. Retrieval of spectral features of $^1/_5$ of the width of the instrumental profile is claimed.

### 3.4.3 Signal to Noise Ratio

#### 3.4.3.1 Photon shotnoise

The frequency distribution among equal time intervals of events which occur randomly in time is described by the Poisson distribution. It may be shown that, if, taking the mean of a large number of equal intervals, z counts occur in a certain time interval, the probability that r counts occur in this interval is:

$$Pr = \frac{z^r e^{-z}}{r!} \tag{3.5}$$

A plot of Pr against r will give the Poisson distribution. Near maximum this curve closely resembles a Gaussian with a standard deviation of $\sqrt{z}$. For small z this approximation is not good, as the distribution becomes very strained. However as z increases the approximation becomes very good. Thus the root mean square error on a photon count of z counts will be $\pm\sqrt{z}$ providing $z >> 1$.

### 3.4.3.2 Detector Noise

This is largely due to thermal emission from the photocathode, with a small contribution from cosmic ray events. Typical noise levels for the EMI S-11 tube used for work on the OIII lines are 5→10 counts per second at room temperature, dropping to 1→2 counts per second at $\sim -5^{\circ}C$. Noise levels of 30→40 per second were achieved by cooling the Ga As RCA tube to dry ice temperatures. The noise levels are merely a zero offset on the data and can be determined and subtracted fairly accurately.

### 3.4.3.3 Other Noise Sources

These include fluctuations in background due to changes in the background illumination, variations in transparency due to changes in the cloud cover, drift of the source across the entrance aperture of the system and extraneous electrical pick-up.

The first two may be eliminated by the use of a compensation channel and the last by the use of careful screening and termination of the signal cables.

### 3.4.4 Computer Programs

The fitting to and the smoothing of line profile data is performed interactively using the Interactive Graphics Communications System of the I.C. Computer Centre. A graph of intensity vs wavelength is displayed on the screen of a Tektronix 4010 graphics terminal, operating at 9600 baud, using a specially installed high-speed line.

Hard copies of the graphical information can be made on 35 mm microfilm, using further facilities provided by I.C. Two data reduction packages exist at present. The first enables the production of microfilm copies of untreated data and of data convolved with various standard functions. The second package allows the fitting of Gaussian profiles to the raw data.

#### 3.4.4.1 Smoothing

There are various purposes to be achieved by smoothing data with various functions.

If the data is Gaussian in form then convolution of it with another Gaussian will have the effect of producing the auto-correlation function, accentuating the position of the line, and allowing a more accurate determination of its position. This process is not sensitive to the exact shape of the smoothing function.

The effective resolution of a profile may be reduced by convolving with the theoretical instrumental profile which is an Airy function. Similarly for the purpose of reducing the noise on the data it may be 'blocked up' by convolving with a rectangular function.

Convolution with a sinc function has the effect of limiting the spatial frequencies present in the data, as would a low-pass filter. Effectively high frequency noise may be removed without affecting the overall line structure. This is exactly the same as taking the Fourier transform of the data, cutting if off at a certain limiting frequency and retransforming. However, care must be taken with data where the noise extends over all frequencies, as spurious components can easily be introduced. This technique is of limited use in conjunction with fitting, whereby a more realistic value of the reduced chi-squared for noisy data may be obtained if some of the high frequency noise is filtered out in advance.

### 3.4.4.2 Fitting: The Chi-squared Test

This test provides a quantitative assessment of the quality of a fit. Essentially a good fit is defined as one where the standard deviation of the errors between the data and the fit is equal to the standard deviation of the random errors on the data.

Thus:

$$\chi^2 = \frac{1}{\sigma_y^2} \sum_{i}^{N} (y_i - f(x_i)^2 \qquad (3.6)$$

$$i=1$$

$$\text{Where } \sigma_y = y^{\frac{1}{2}} \qquad (3.7)$$

And thus:

$$\chi = \sum_{i=1}^{N} \frac{(y_i - f(x_i)^2}{y_i} \qquad (3.8)$$

Thus, in the case where the two standard deviations are equal then chi-squared will have the most probable value N. The reduced chi-squared is defined as $\chi^2/N$ and thus has a most probably value of 1 for a best fit. In practice if the value of chi-squared is lower it indicates that the variance of the fit to the data is too low, and thus the fit is over-constrained, ie too many parameters have been used. Conversely, too high a value of chi-squared indicates that too few parameters have been used. The values of chi-squared will usually lie within the limits:

$$N-\sqrt{2N} \leq \chi^2 \leq N+\sqrt{2N} \qquad (3.9)$$

which covers the range in which the fitted function f(x) may be considered a reasonably good fit.

When fitting to data which has noise of a higher frequency, the value of chi-squared will usually be very much higher than allowed by the criterion set by equation 3.9, whilst still fitting the general low-frequency features of the spectrum quite well. It is in this case that the use of a sinc function, to filter out high frequency noise, can be of value.

### 3.4.4.3 Fitting Programs

A non-linear least squares fitting routine, described by Bevington (1969) is used to fit a specified function to the data. This routine is looped to obtain the best fit, which is then displayed on the screen of a Tektronix terminal along with the parameters of the fitted function (Figure 3.5(a)). At present up to 10 Gaussions may be fitted to a single spectrum, each of which is specified by three parameters: the height, halfwidth and position. The residual to the fit, along with each fitted component, may also be displayed (Figure 3.5(b)), to clarify the relative shapes and positions of the profiles.

For single profiles, ie those with no appreciable structure, the fitting of Gaussian profiles facilitates the accurate location of the height, halfwidth and position of the profile, allowing the determination of relative radial velocities, relative intensities and an indication of the Doppler broadening. In addition, for profiles with two clearly separated components, accurate values for the velocity splitting can be found.

The situation is different, however, in the case where profiles have blended components or are assymmetric. In this case the position at which a blended component is found is strongly dependent upon the exact form of the fitting function. In many cases a very good visual fit can

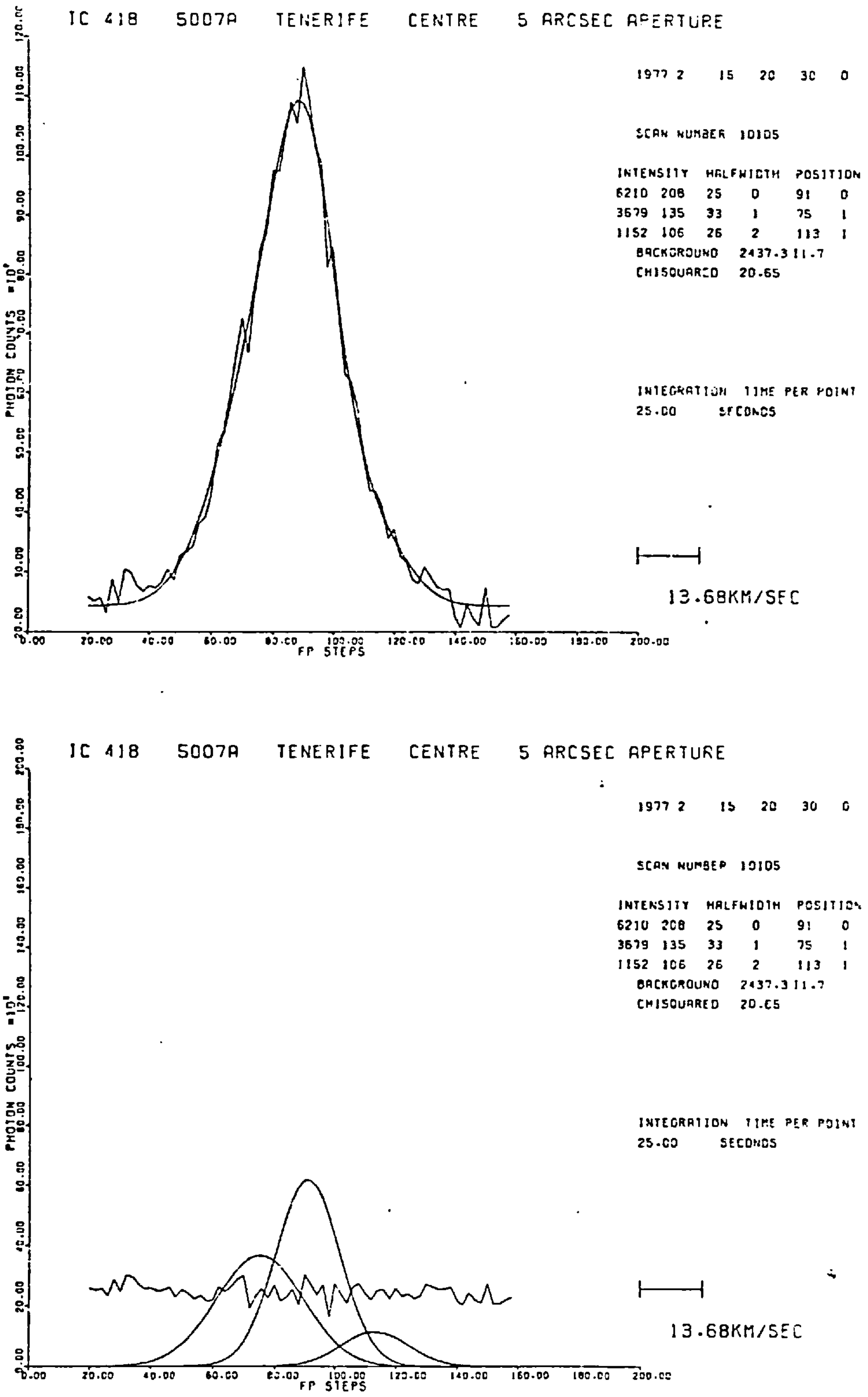
IC 418 5007A TENERIFE CENTRE 5 ARCSEC APERTURE
1977 2 15 20 30 0
SCAN NUMBER 10105
INTENSITY HALFWIDTH POSITION
6210 208 25 0 91 0
3679 135 33 1 75 1
1152 106 26 2 113 1
BACKGROUND 2437.3 11.7
CHISQUARED 20.65
INTEGRATION TIME PER POINT
25.00 SECONDS
13.68KM/SEC
PHOTON COUNTS *10²
FP STEPS
0.00
20.00
40.00
60.00
80.00
100.00
120.00
140.00
160.00
180.00
200.00
30.00
50.00
70.00
90.00
110.00
120.00
IC 418 5007A TENERIFE CENTRE 5 ARCSEC APERTURE
1977 2 15 20 30 0
SCAN NUMBER 10105
INTENSITY HALFWIDTH POSITION
6210 208 25 0 91 0
3679 135 33 1 75 1
1152 106 26 2 113 1
BACKGROUND 2437.3 11.7
CHISQUARED 20.65
INTEGRATION TIME PER POINT
25.00 SECONDS
13.68KM/SEC
PHOTON COUNTS *10²
FP STEPS

Figure 3.5

be found by increasing the number of components fitted, but this usually results in a value of chi-squared which is too low, indicating that the fit is over constrained. In this eventuality, if an analytic function which adequately represents single profiles from the same source cannot be found, we must resort to modelling to attempt to synthesize the profile. This is discussed further in the Appendix.

# CHAPTER 4: ASTRONOMICAL OBSERVATIONS

## 4.1 NGC 3242

### 4.1.1 Introduction

NGC 3242 has a fairly bright stellar nucleus which is surrounded by a roughly elliptical ring of bright nebulosity whose major and minor axes are approximately 26" and 16" in length and the major axis position angle is 145°. Around this bright ring is a fainter and slightly patchy oval disc of diameter about 40" by 35".

One of the most notable features of this object is that it is a non-thermal radio source (Meron and Terzian 1965) which renders it unique amongst the bright, symmetrical nebulae.

Isophotal contour maps obtained by Minkowski and also by Feibelman (1970) suggest the presence of condensations at the ends of the major axis of the inner ring.

Czyzak et al (1965) made electron temperature and density measurements based on various forbidden line ratios and also on the Hβ flux. From this data they found $T_e = 11,500\ ^{o}k$, $N_e = 6,000\ cm^{-3}$ and suggested that filamentary structure may not be an important factor in the determination of the density of the central regions.

Morphological studies by Wilson (1946) and later by Weedman (1968) indicate that the inner ring is expanding at about 20 km $sec^{-1}$ with respect to the central star. The slight tilt found on the emission lines obtained when the slit was orientated along the major axis indicates that this axis is almost perpendicular to the line of sight. No line tilt was found by Wilson (1946) with his spectrograph slit at position angle $90^{o}$, ie almost along the minor axis.

Weedman (1968) observed a tendency for the expansion velocity to increase as the radial coordinate of the position of the observation increased, assuming that the nebula was prolate in form with the major axis equal to 1.5 times the length of the minor axis. This velocity gradient was found to be 6.6 km $sec^{-1}$ arc $sec^{-1}$.

Perhaps one of the most interesting morphological questions is whether the inner, bright ring and the outer shell are separate or are physically related. There are many examples of multiple or double ringed planetaries: NGC 2392, NGC 6826, NGC 7009 etc. The physical relationship of these shells has important implications for the ejection mechanisms responsible for their formation. If the shells are separate it would suggest that they arise from a series of separate ejections in which a complete shell is thrown off in a comparatively short time, rather than being formed from some continuous process of mass loss. It might then be expected that the shells would be expanding at different velocities owing to their different radii and possibly in different shapes, depending upon the initial conditions. It might also be expected that some kind of structure would be observed in the line profile due to the physical separation of the shells. The major difficulty with observing an outer halo is that it is usually very faint compared to the inner structure. This usually means that unless the halo is observed at some distance from the bright ring, it tends to get swamped by the radiation from the inner region. In the following sections the results of a preliminary study of the radial velocity field of NGC 3242 are discussed, in order to determine whether any evidence existed to suggest that the halo was physically separate from the inner ring.

### 4.1.2 Radial Velocity Data

Observations of the radial velocity field of this object were taken on the 1.5m Flux collector in Tenerife. A Fabry Perot Interferometer was used operating at a resolution of 80,000 with a finesse in excess of 30 and a free spectral range of 2Å at 5000Å. Spectral scans of the [O III] λ 5007Å line profile were made at various positions on the nebula. Figure 4.1(a) shows the positions from which the profiles were observed superimposed on a λ 5007 Å isophotal contour map of NGC 3242. The size of the circles shown represent the size of the entrance aperture. Figure 4.1(b) shows the profiles obtained set out in the same relative positions. The intensity scale for each profile is the same. Wavelength increases to the right.

Clearly the maximum line splitting occurs in the centre of the nebula. This splitting has been measured by fitting Gaussians to the profile, as 39.9 ± 0.4 km $sec^{-1}$. This corresponds closely to the figure of 39.6 km $sec^{-1}$ obtained by Wilson (1950), and gives an indication of the accuracy of the calibration.

Moving to the edge of the nebula the line splitting decreases and the lines broaden and merge together. Once in the outer

Figure 4.1(a) NGC 3242 OIII contour map

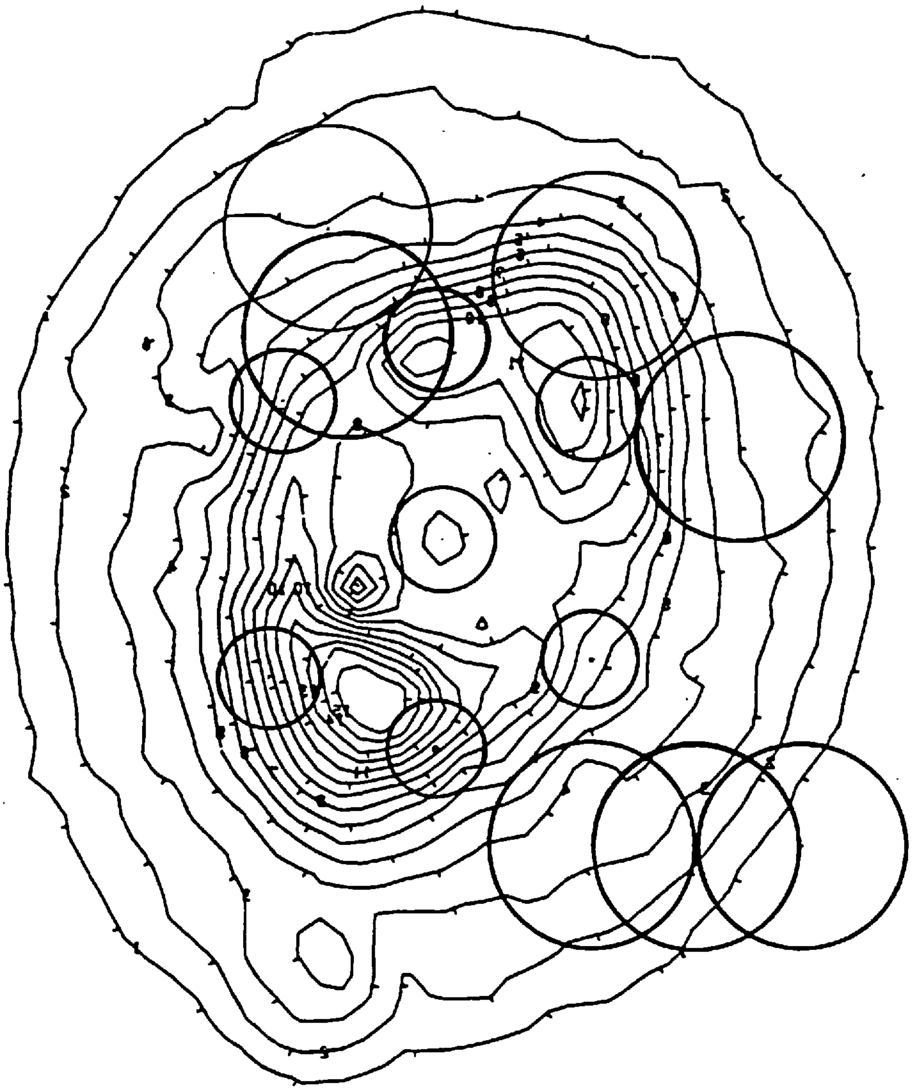

Figure 4.1(b) Line Profiles

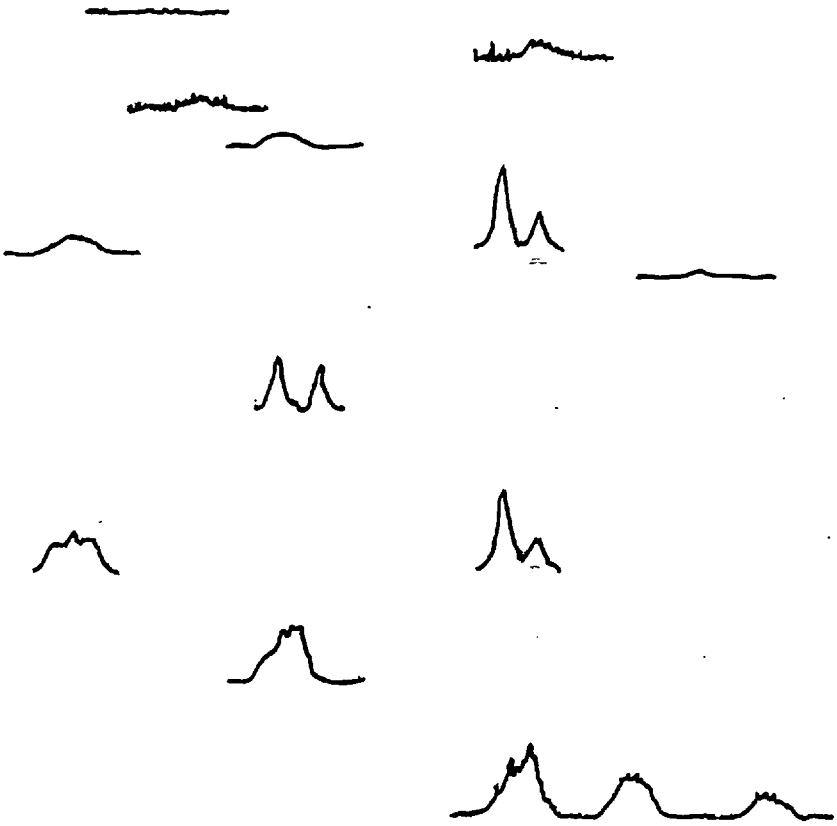

halo the lines become very broad and are no longer split. Comparisons of the mean radial velocity of the halo profile and that of the centre of the nebula (Figure 4.2) indicate an apparent shift to the red. Profiles obtained from a position at the southern end of the bright inner ring show a component which appears to be at zero radial velocity relative to the centre (Figure 4.3). This component corresponds to a blend found on a profile obtained at a position immediately adjacent, but does not appear at any other position.

### 4.1.3 Discussion

Inspection of this data allows a number of general points to be made concerning the form of the nebular envelope:

1) The shape and width of the lines arising from the outer halo indicates a more or less continuous distribution of gas along the line of sight. This suggests that the halo is not necessarily a physically distinct shell separated from the bright inner ring, and was probably formed during some continuous process of ejection.

2) The apparent shift in radial velocity of the halo compared to the centre of the nebula could be explained by a very patchy shell, the deficiency of material at a particular

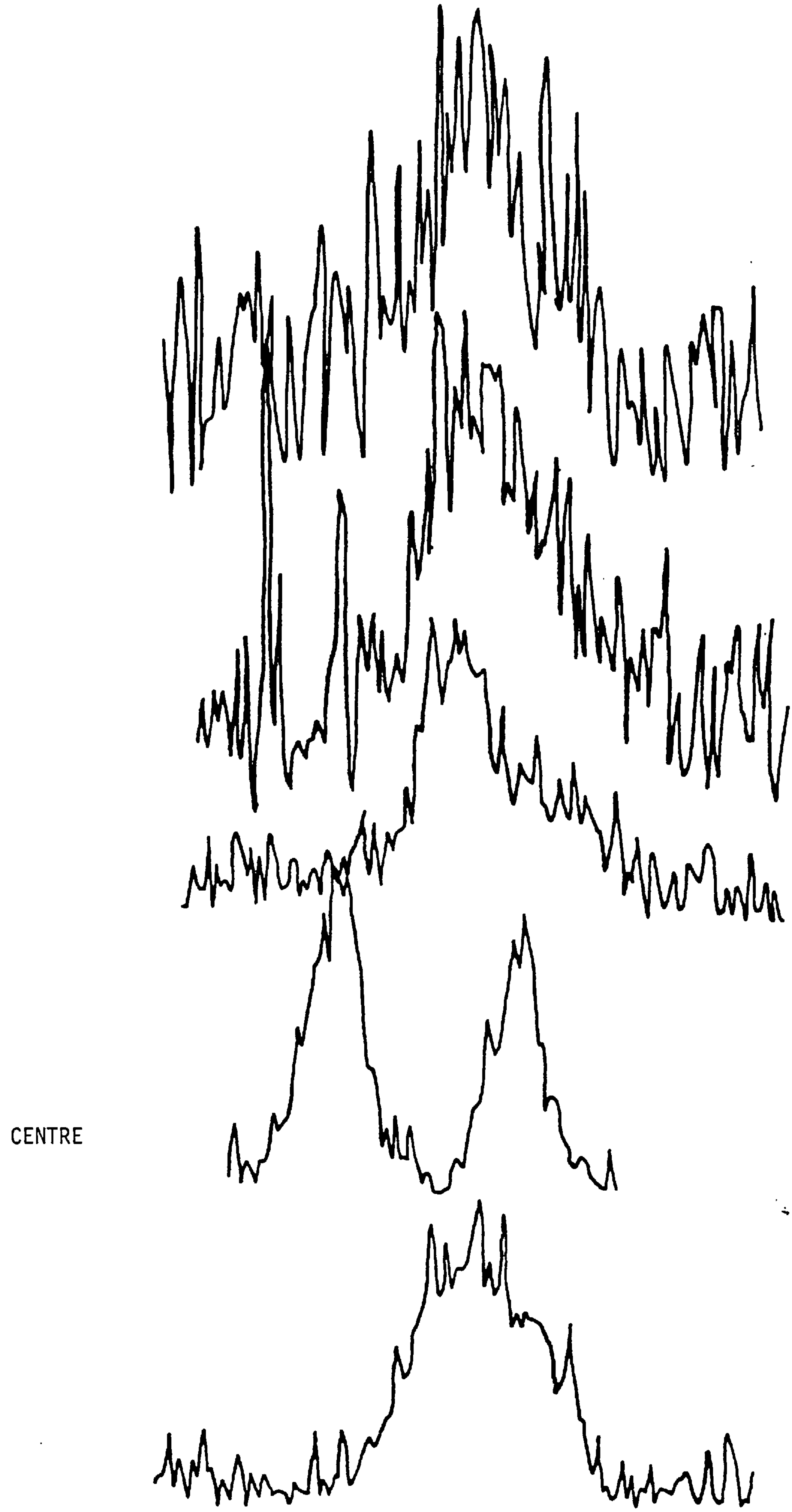

Figure 4.2 NGC3242 Scans of outer halo

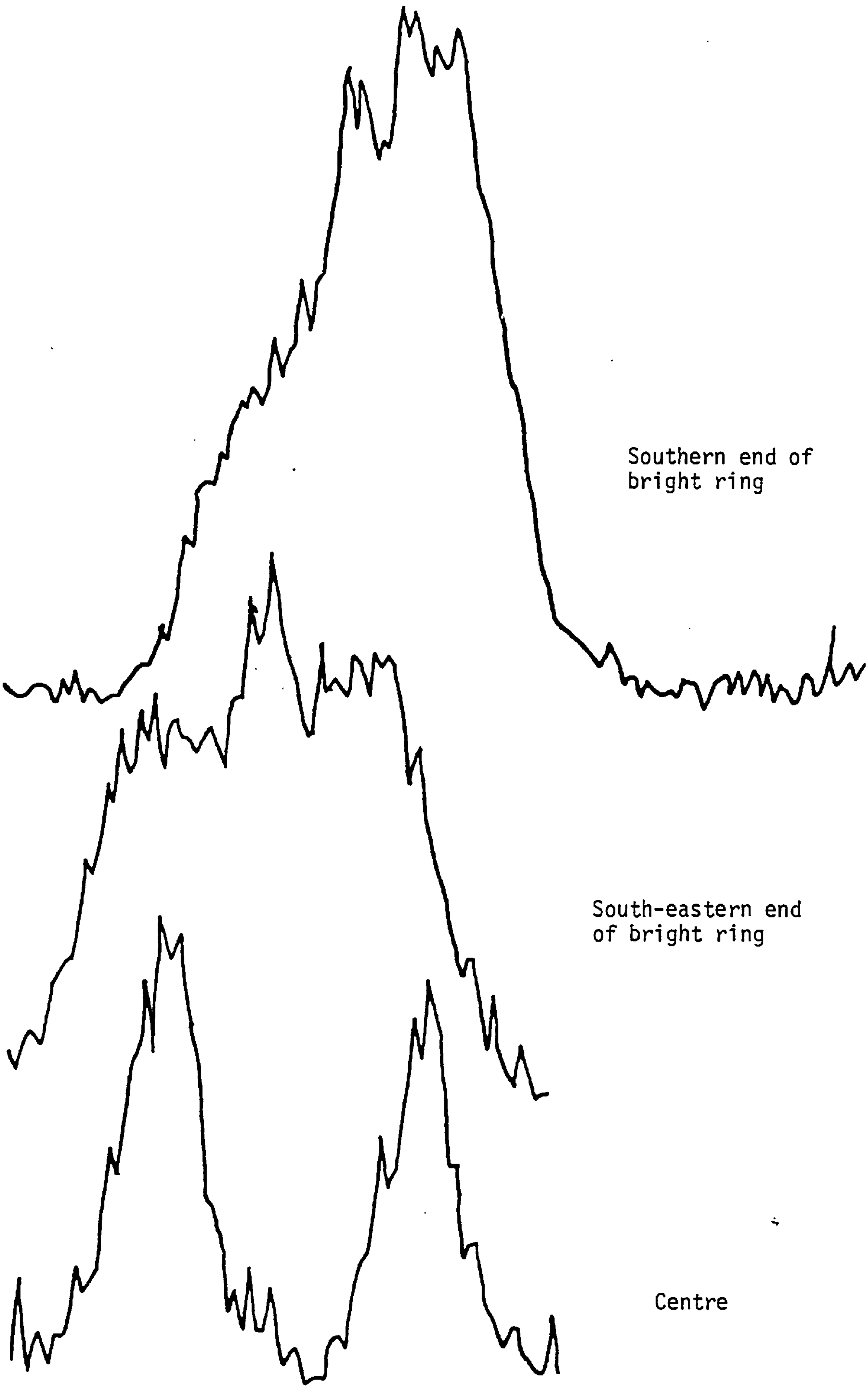

Figure 4.3 NGC 3242 Scans with 3 components

radial velocity tending to distort the profile. Evidence for this patchiness can be seen in a print of the λ5007Å electronograph (Figure 4.4 ).

An alternative explanation might be that the movement of the planetary through the interstellar medium has produced a distortion of the shell, in the manner suggested by Bohuski and Smith (1974). This could shift the centre of gravity of the line profile.

3) The presence of a zero velocity component at one end of the bright ring and the assymmetric way in which the splitting varies across the object indicates that the structure of the nebula is not as symmetrical as it might first appear. Feibelman (1970) has suggested that condensations may exist at one end of the bright ring and it could be that these may be responsible for the strange shape of the profile.

Due to the unreliability of the off-setting of the telescope, the absolute and relative positions of the various profiles are somewhat uncertain. Furthermore large fluctuations in the 'seeing' occurred during several of the scans and this may also have introduced some distortions in the profiles.

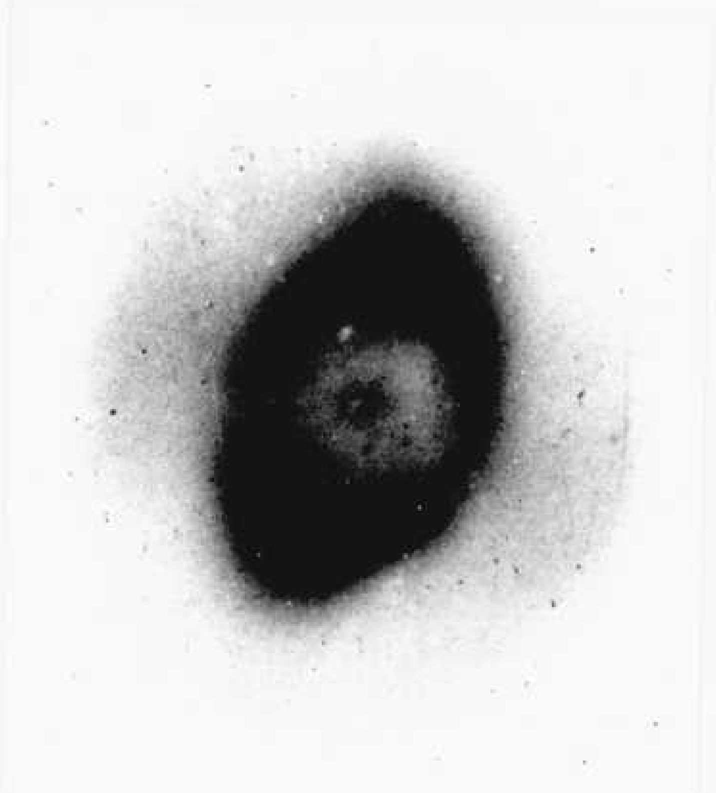

Figure 4.4 NGC 3242 OIII 5007Å

Mapping of the radial velocity field at a spatial resolution of around $\hat{1''}$ to $\hat{2''}$ is needed before any firmer conclusions can be drawn about this object.

## 4.2 NGC 6720

### 4.2.1 Description

NGC 6720, otherwise known as the Ring nebula in Lyra, is distinguished by its symmetrical, bright, ring-like structure. It is surrounded by an extensive and very faint outer halo of about twice the diameter of the inner ring, discovered by Duncan (1937) and is of medium excitation, Wilson (1950).

Previous spectral investigations of NGC 6720 have been confined to spectroscopy using grating spectrographs (Wilson, 1950). However the large diameter and relatively low surface brightness make this object difficult to observe using instruments of this type. This is because the width of the entrance slit of conventional grating spectrographs required for resolutions of 60,000 represent only a very small fraction of the size of the nebula, severely restricting the amount of light available.

### 4.2.2 Temperature and Density

Spectroscopic observations (Minkowski and Osterbrook, 1960) show three distinct regions of density determined from the [O II] ratio of λ 3729/λ3726: the outer shell, where $N_e$ = 280 $cm^{-3}$, the ring where $N_e$ = 730 $cm^{-3}$, and the central regions where $N_e$ = 550 $cm^{-3}$. Boeshaar (1974) has argued, from measurements of the [S II] lines, that the ring consists of very high density filaments ($N_e \sim 5.10^3 cm^{-3}$) embedded in a uniform, low density envelope (Aller et al, 1970 suggest that inadequacies in the published cross sections may affect this data). This leads to a variation in measured temperature and density dependent upon the position in the nebula and the ion used for the determination, although there is a tendency for the temperatures to be higher in the central region than in the ring.

Aller and Walker (1970) have found that [N I] λ5200 Å and [N II] λ 5755 Å are virtually missing from the interior, although it is strong in the ring, suggesting that this radiation arises mainly from the filamentary structure. Reay and Worswick (1977) have shown from electonographic exposures in the light of [O I] λ6300 Å, that the cool knots and condensations are preferentially located along the minor axis of the nebula.

The nebula itself is well stratified, the ionization structure having a profound effect on its visual appearance.

### 4.2.3 Ionization Structure

The stratification of NGC 6720 has been studied extensively notably by Proisy (1974) and Louise (1974), using photographic methods, and by Reay and Worswick (1977) using electonography.

A general trend of increase in image size with decreasing ionization potential is seen, except in the cases of HeI and [NeIII.] The HeI region is of similar size to that of HI (Reay and Worswick, 1977) which conforms with model calculations for $T_* > 40,000$ °K(Osterbrock , 1974). Reay and Worswick (1977) measured the ellipticity (defined as the ratio of the minor axis to the major axis) of the nebular envelope from the separation of the emission peaks along the major and minor axes, Er, and from the overall dimensions along these axes Eo. They found no systematic variation of Eo with ionization potential, indicating that the outer regions of the nebula are defined by the general gas distribution. A general tendency for Er to increase with ionization potential suggests that the inner structure is a result of ionization. Thus we may assume that the nebula is density bounded.

Observational evidence indicates that for density bounded nebulae the [O III] λ5007 Å and the HI λ4861 Å radiations originate in the same region (Weedman, 1968). Furthermore expansion velocities measured from these two lines are usually in close correspondence. The validity of this generalization for the case of NGC 6720 is proven by Figure 4.7, which shows that the [O III] and HI regions have essentially identical shapes and sizes.

The suitability of the [O III] line for spectroscopic observations of the velocity field is due to its low thermal broadening and its origin in the same regions as the HI emission.

### 4.2.4 Morphology

The structure of NGC 6720 has been the subject of some controversy. Minkowski and Osterbrock (1960), Osterbrock (1960) and Hua and Louise (1972) have suggested that it is a toroidal structure, mainly from density considerations. Simple ellipsoidal or spheroidal shells proposed by Curtis (1918), and Gurzadyan (1970) were ruled out by Louise (1974) on the basis of the ellipticity of the observed distribution and the relative intensities of emission from the centre of the nebula and the outer ring. From a study of monochromatic photographs of the nebula, he proposes instead a choice of two models. Either an oblate spheroid, with density enhancements around the equator, or a quasi flat band structure, resembling a toroid, tilted at an angle of 45° to the line of sight. Both of these models are consistent with the observations of Hua and Louise (1972) who determined the variation in the width of the band with angle for the N II line, concluding that a flat band type model best fitted their data. The [N II] lines being low excitations, arise from the extreme outer regions of the nebula, mainly from filaments and condensations (Williams, 1970; Aller and Walker, 1970; Capriotti, 1973) and are not necessarily representative of the overall structure of the nebula. A programme of high spectral resolution observations, to investigate the velocity field, is suggested to help distinguish between these models.

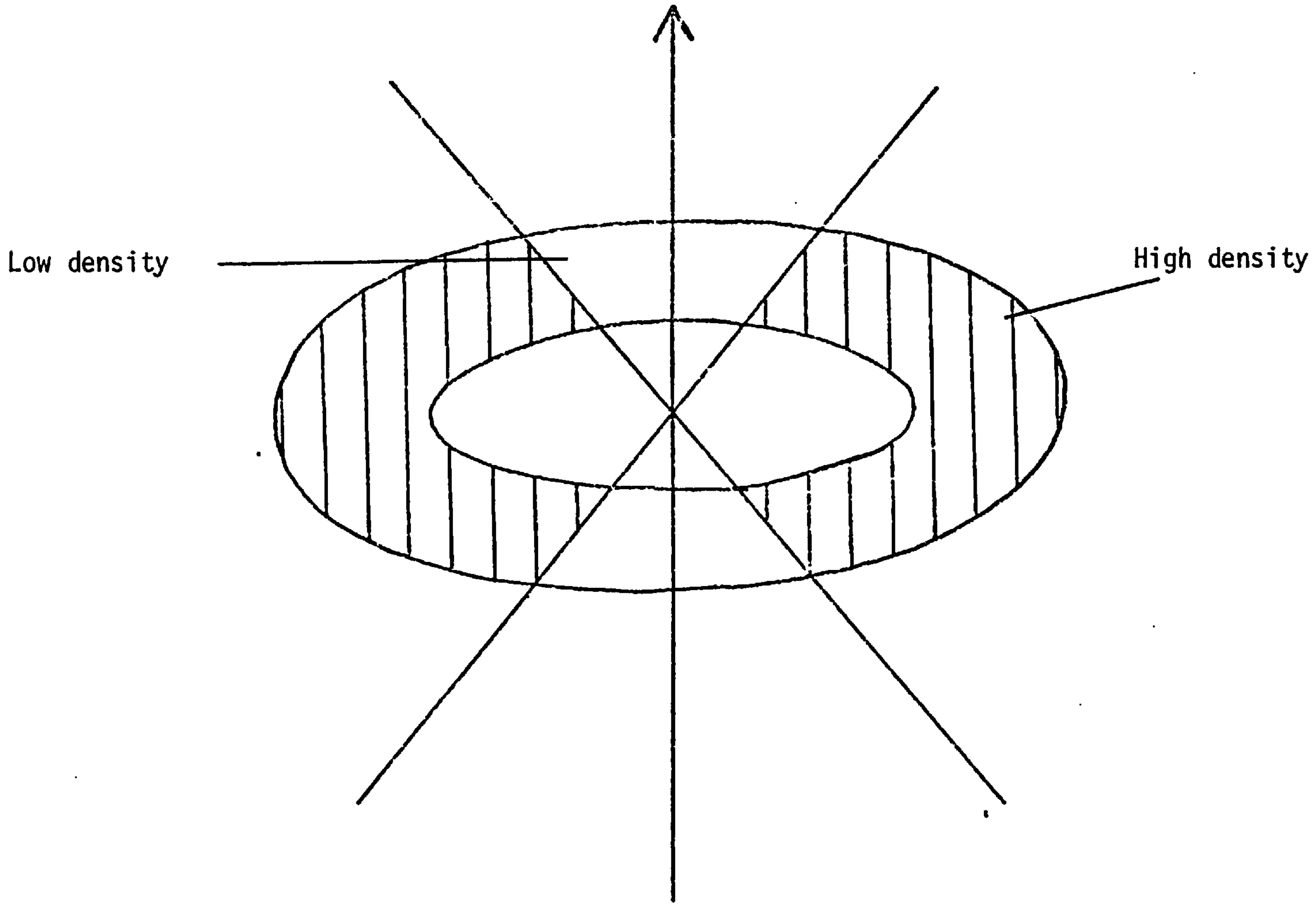

Figure 4.5 NGC 6720 Model of Louise (1974)

Proisy (1974) has proposed a toroidal, barrel-shaped distribution, the axis of which lies in the plane containing the observer and the major axis of the observed distribution. This model is shown in figure 4.6. The model is based on monochromatic photographs taken in the light of H$\alpha$ + [N II], [O III], He II and [Ne III] and is claimed to be of general applicability, presenting an outline which varies from rectangular to circular, depending upon the angle of projection (in this case between 30° and 50° to the line of sight).

The variety and number of these models may well imply that either the structure of NGC 6720 is not as simple as it appears, or that the data upon which they are based is inadequate in quality or scope. In the following section the results of a programme of observations of NGC 6720, using a Fabry Perot Interferometer, are presented and combined with electronographic observations obtained by Reay and Worswick (1977) to develop a model envelope which is consistent with the observations to date.

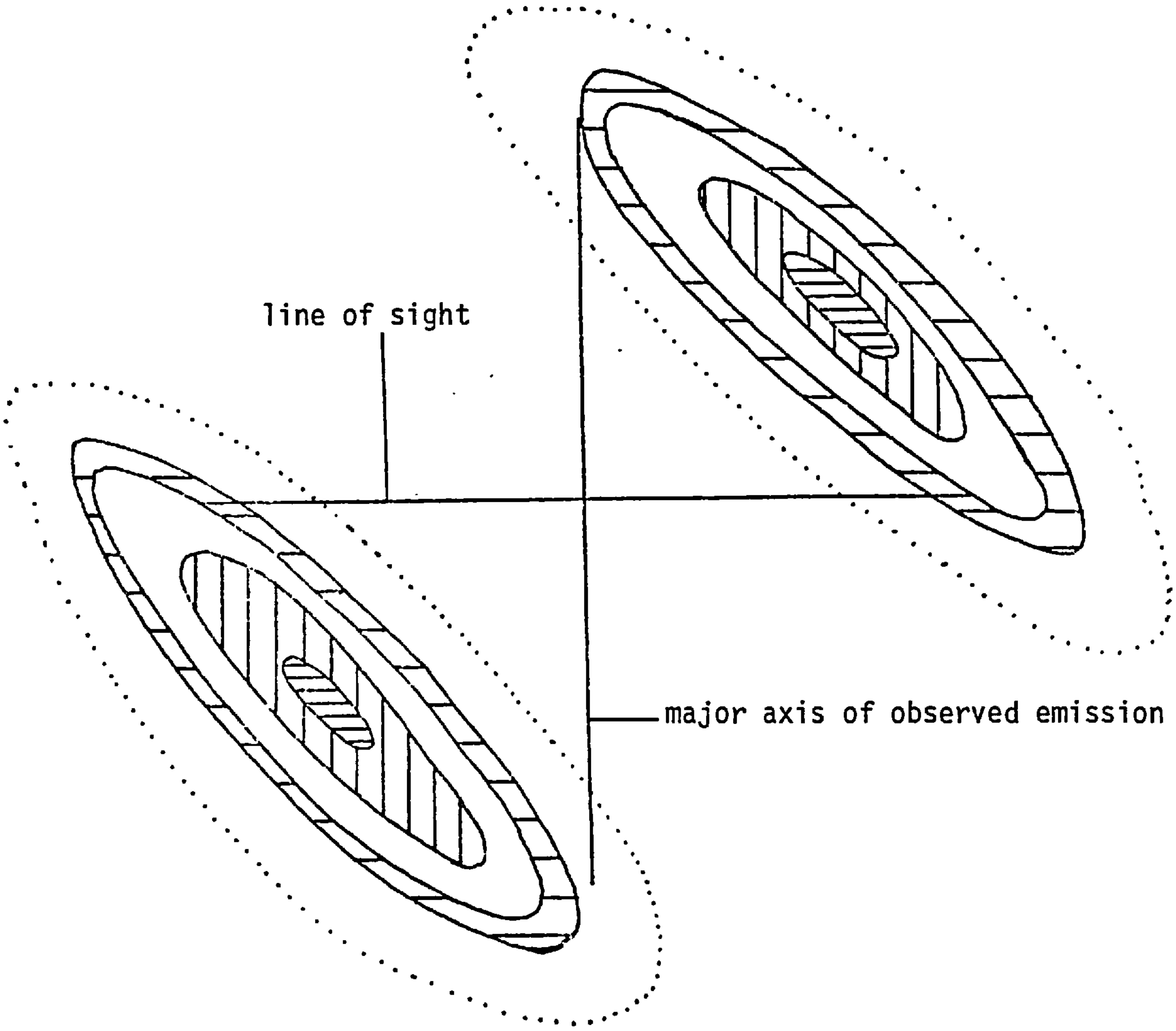

Figure 4.6 NGC 6720 Model of Proisy (1974)

### 4.2.5 Observations

#### 4.2.5.1 Electronographic Observations

The evaluation of relative intensity variations across the nebula is facilitated by the large dynamic range of the electronographic process which makes it possible to obtain relative fluxes on both the bright and faint regions of the nebula at the same time. Comparisons between electronographic and photographic data show substantial agreement for small intensity variations, but for large changes higher ratios are found from the electronographic process than from the photographic process.

Figure 4.7 shows contour maps produced from the [OIII] λ5007 Å + λ4959 Å and the Hβ 4861Å exposures. Figure 4.8 contrasts the map for the high excitation He II λ4686Å line with the lower excitation [NII] λ6583Å line. Whilst the [OIII] and Hβ exposures show almost identical structure, the HeII and [NII] maps illustrate well the effects of the stratification of the nebula.

In addition, photometric information has been obtained along directions corresponding to the major and minor axes of the nebula. Figure 4.9 shows that for [NII] the intensity in the centre of the nebula falls to about 3%

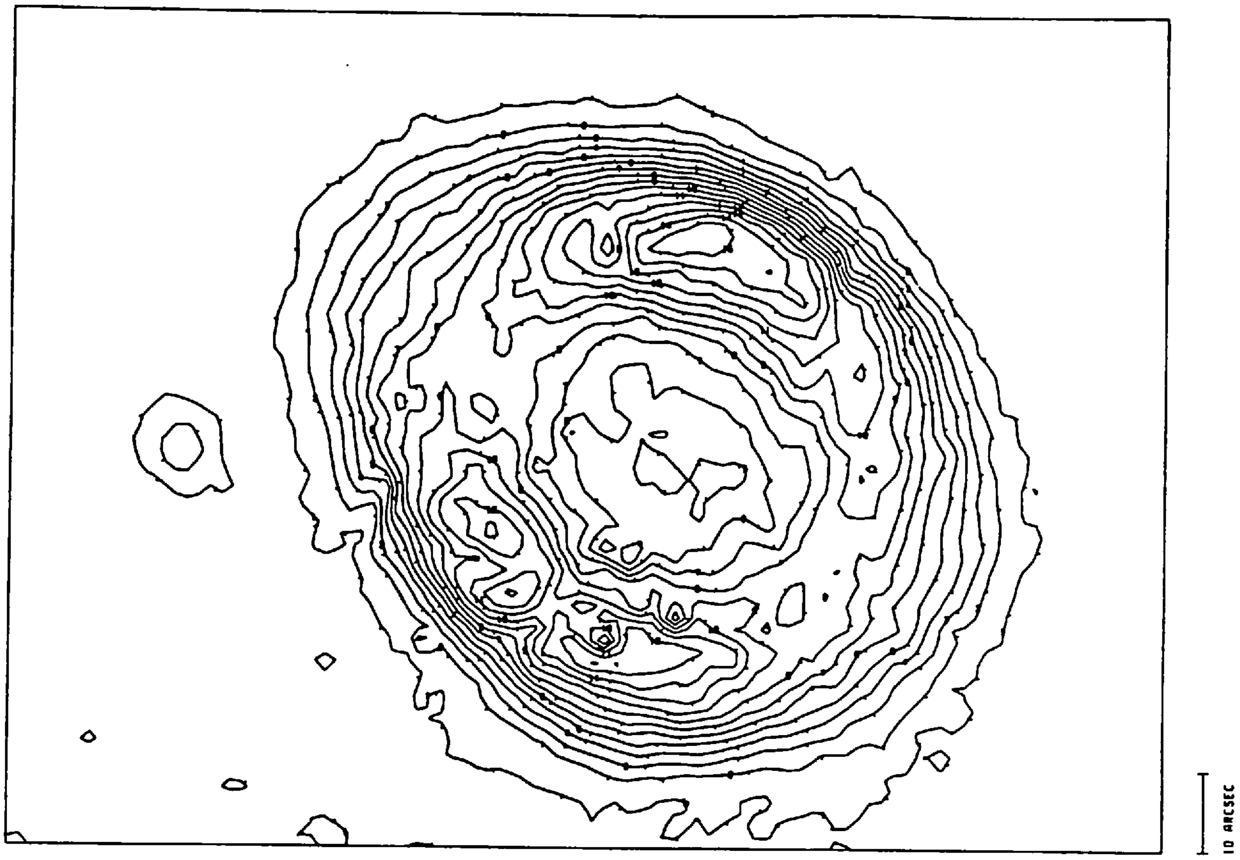

H-Beta

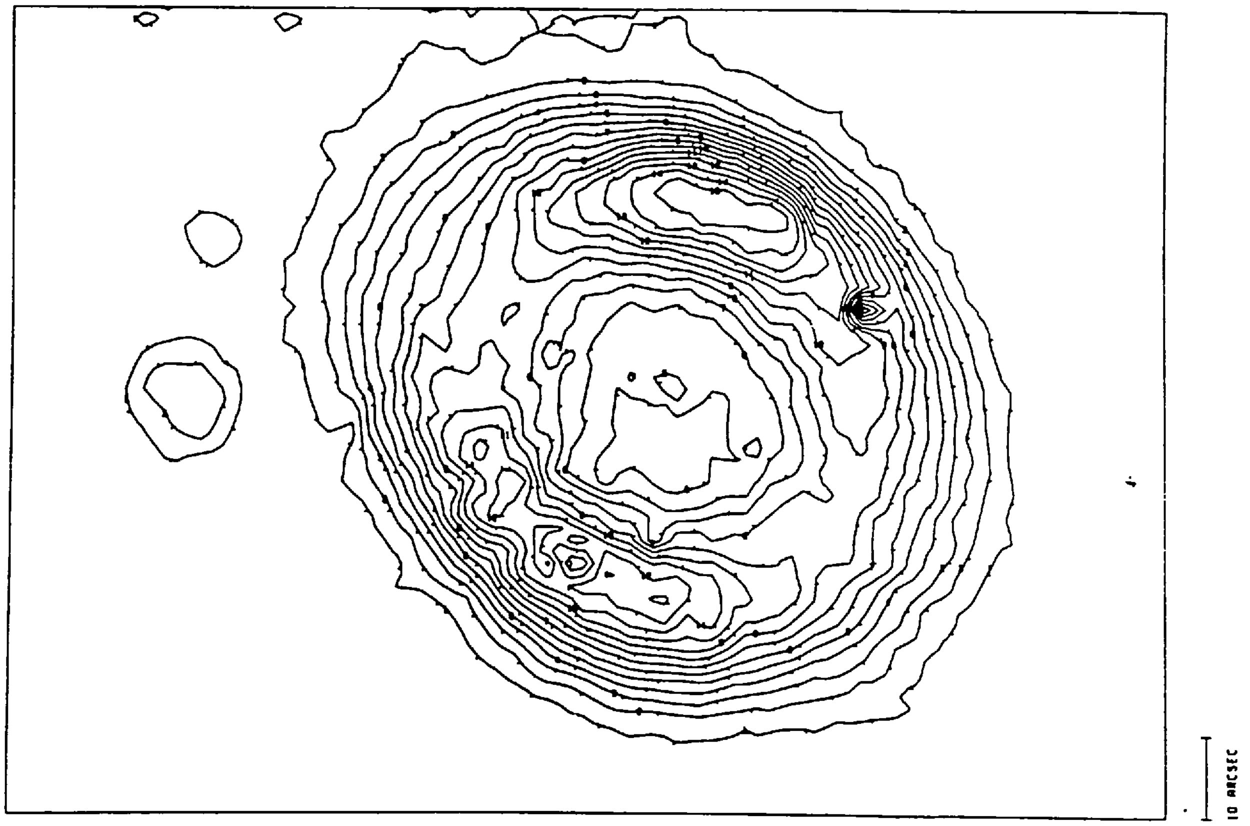

[O III]

Figure 4.7

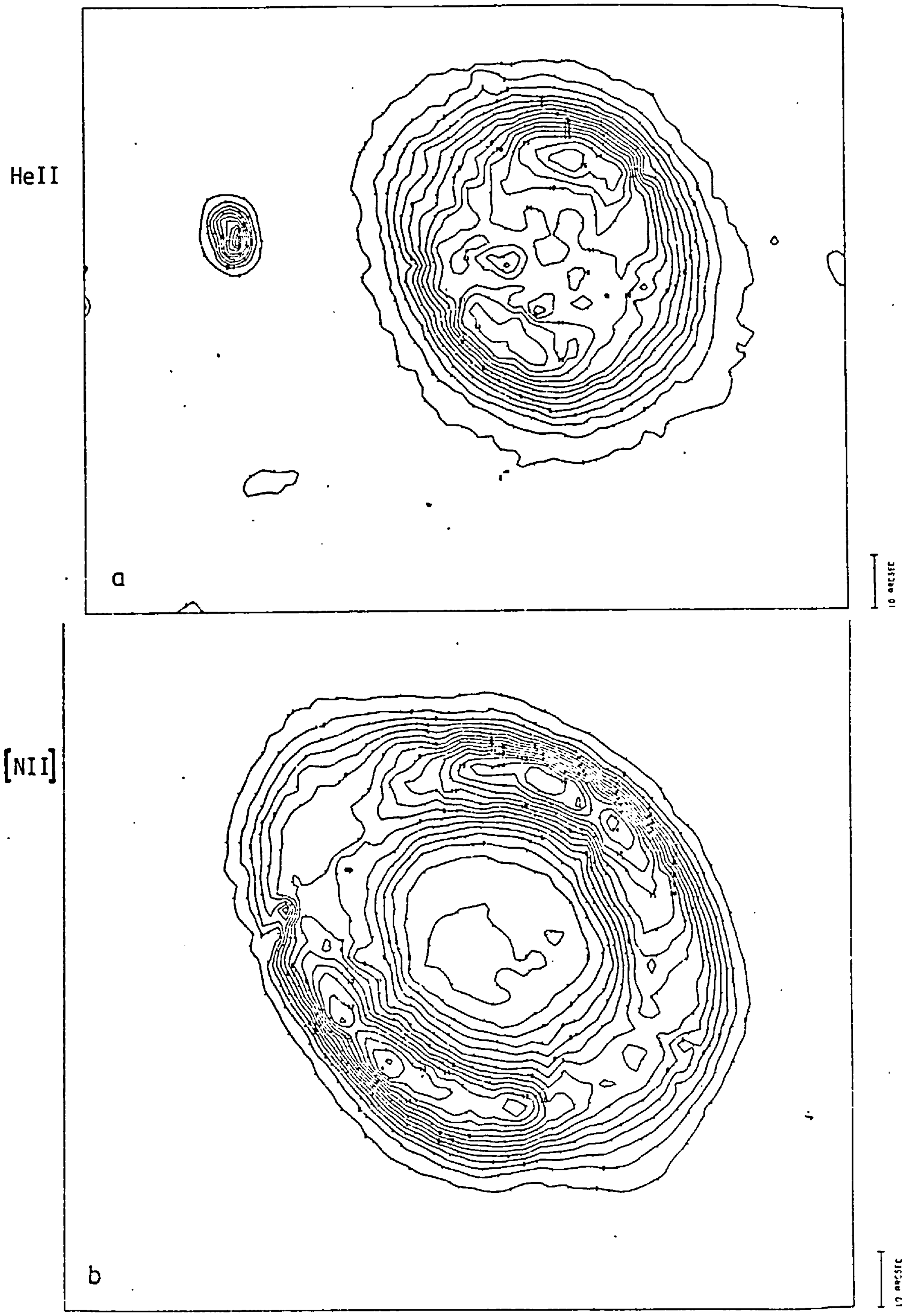

Figure 4.8

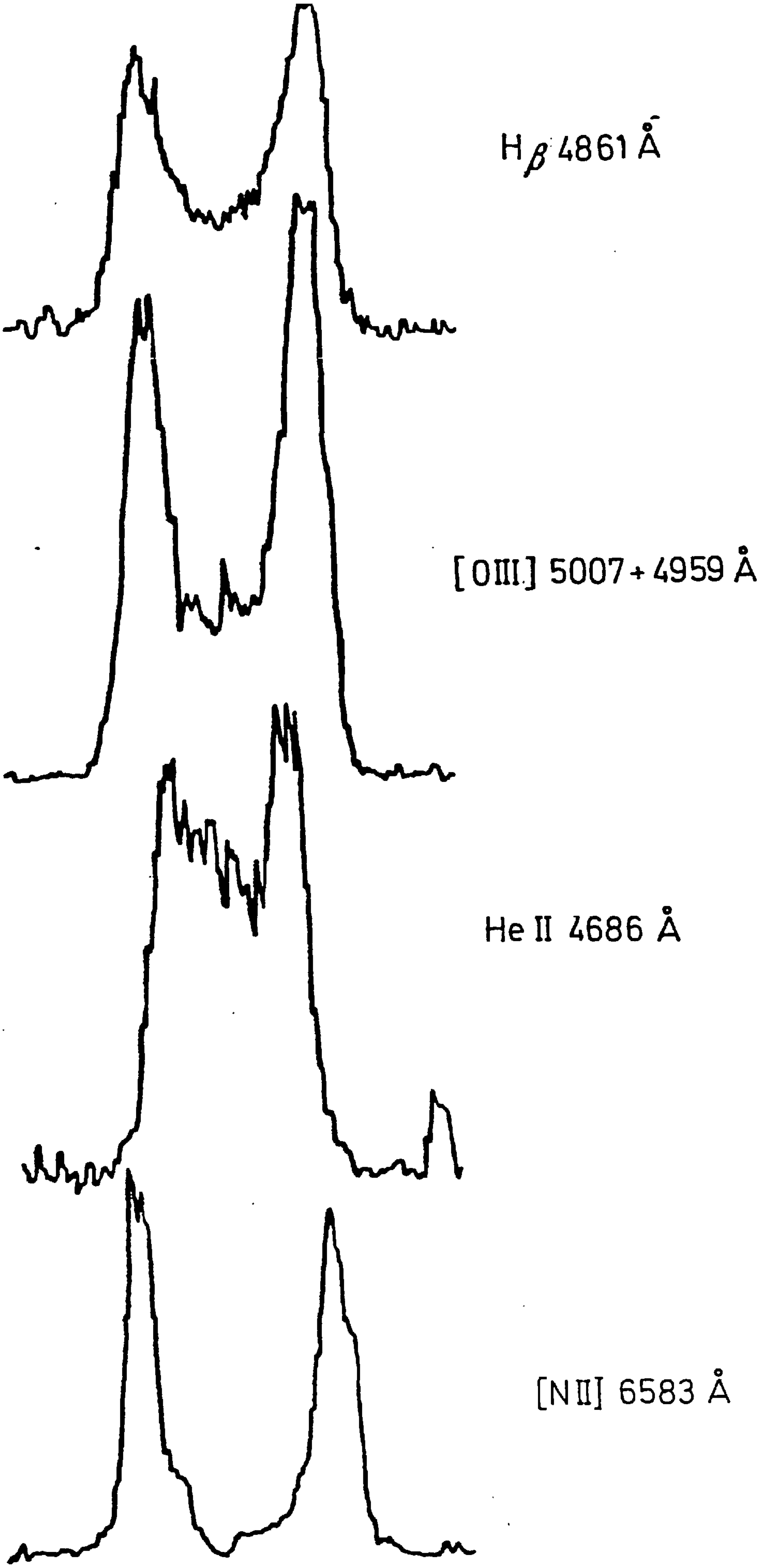

Figure 4.9 NGC 6720 Intensity scans across electronographs

| Line | [OIII] | [OI] | HI | HeII | [NeIII] | [NII] |
|---|---|---|---|---|---|---|
| Wavelength (Å) | 5007+4959 | 6300 | 4861 | 4686 | 3868 | 6583 |
| Major Axis (Arcseconds) | 106 | 115 | 101 | 89 | 100 | 115 |
| Minor Axis (Arcseconds) | 81 | 97 | 87 | 71 | 83 | 96 |
| Separation of major axis peaks (Arcseconds) | 46 | 70 | 53 | 25 | 53 | 63 |
| Separation of Minor Axis Peaks (Arcseconds) | 49 | 64 | 52 | 36 | 52 | 59 |
| Relative flux between peaks of Ring and Centre of Nebula | 3.7 | 79 | 3 | 1.7 | 6.2 | 33 |

Table 4.10

Dimensions and Relative Intensities
Measured from Electronographs

of the peak intensity in the ring. For Hβ the intensity ratio is ∿ 3:1 and for HeII it is less than 2:1. The dimensions and relative fluxes of the relative exposures are given in Table 4.10.

### 4.2.5.2 Radial Velocity Field Observations

The observations were made using a Fabry Perot Interferometer operated in the 2000th order at a resolution of 67,000 and a free spectral range of 3Å. Spectral scans were obtained with a sample interval of 0.02 - 0.03Å over a wavelength range of 2-3Å centred on the line of interest. Observations were made of the [OIII] λ5007Å line profiles at various positions on the nebula.

Figure 4.11(a) shows the positions at which the profiles were obtained, superimposed on a λ5007Å isophotal contour map of the object, reproduced from Reay and Worswick (1977). The points form a cross orientated approximately along the major and minor axes of the emission distribution, with the size of the aperture relative to the nebula represented by the size of the circle. Figure 4.11(b) shows the line profiles obtained at each of these positions. Wavelength decreases to the right. For the purposes of this presentation the raw data has been smoothed by convolving it with an Airy function - the theoretical profile of the interferometer - of width 0.11Å, reducing the effective resolving power to 45,000. The scan at bottom right has

Figure 4.11(a)

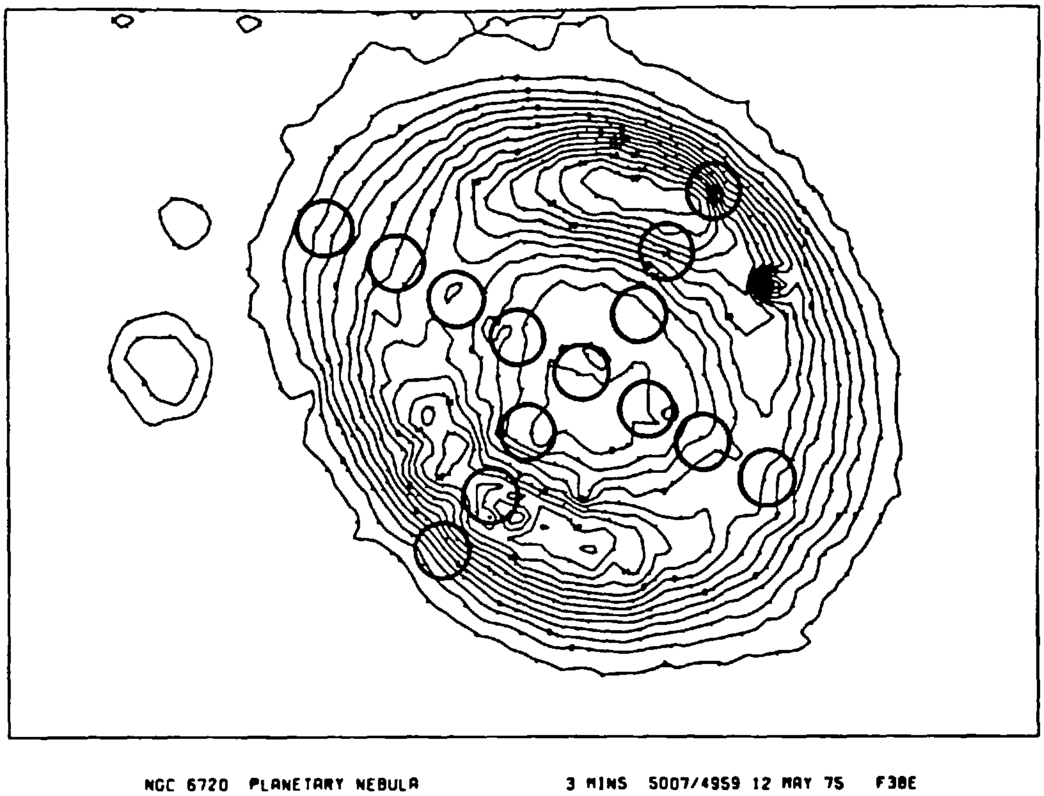

Figure 4.11(b)

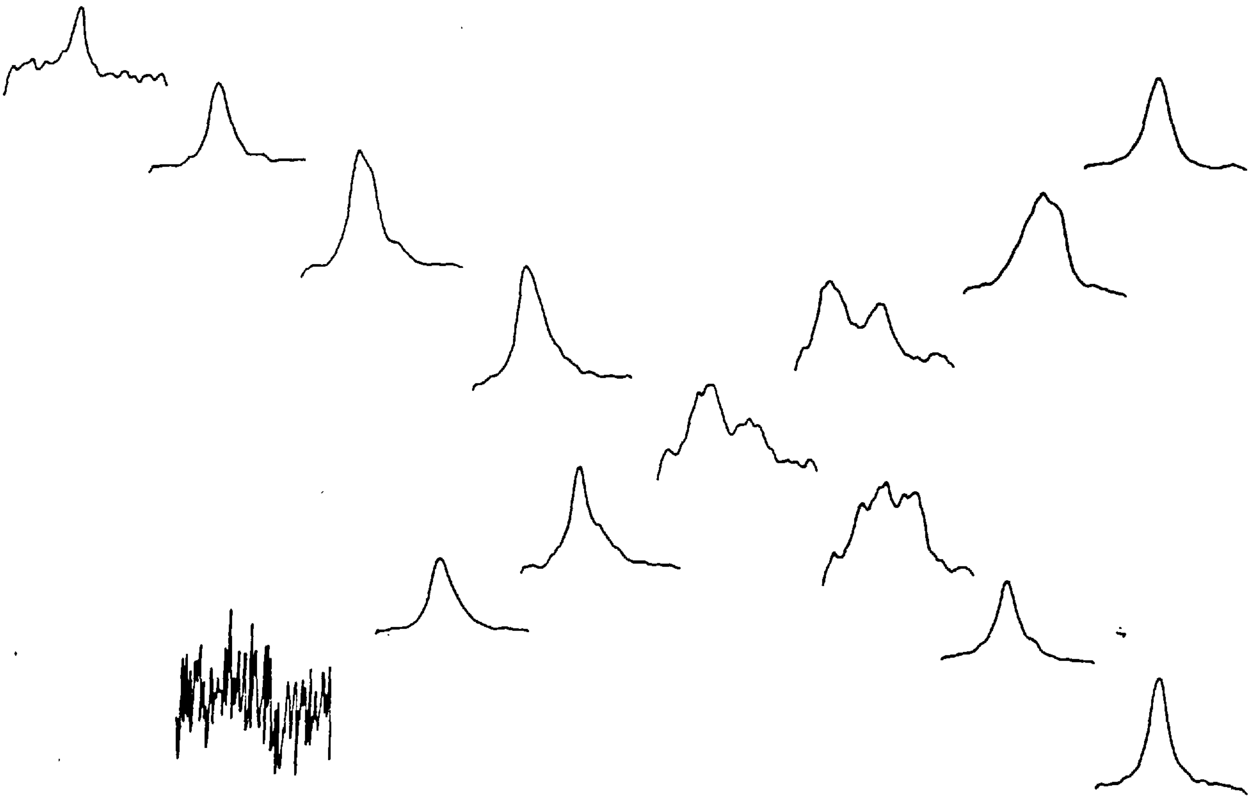

not been processed in this way as it is just noise.

Figure 4.12 shows the velocity measured from the fitted component of the emission profiles plotted against position along the major and minor axes of the nebula. For the inner regions, where the profile is split into two components, the mean velocity of the two has been plotted.

The line splitting of 50 ± 3km $sec^{-1}$ near the nebula centre quickly falls off with increasing radius and thereafter the unresolved line profile narrows as the edge of the nebula is approached. Wilson (1950) found a line splitting of 60 km $sec^{-1}$ for [Ne III] but this is consistent with the size of the [Ne III] image, it being greater than that of [OIII] (Reay and Worswick, 1977). The absence of two components from some of the profiles in the inner regions indicates local deficiencies in the front and rear surfaces of the shell which are not readily apparent from the electronographs, but show up as rapid changes in the inner contour levels of the maps shown in Figure 4.7.

From Figure 4.12 it can be seen that the mean radial velocity is constant at all positions along the major and minor axes. There seems to be no evidence for any 'tilt' of the spectral lines that is observed in some planetaries

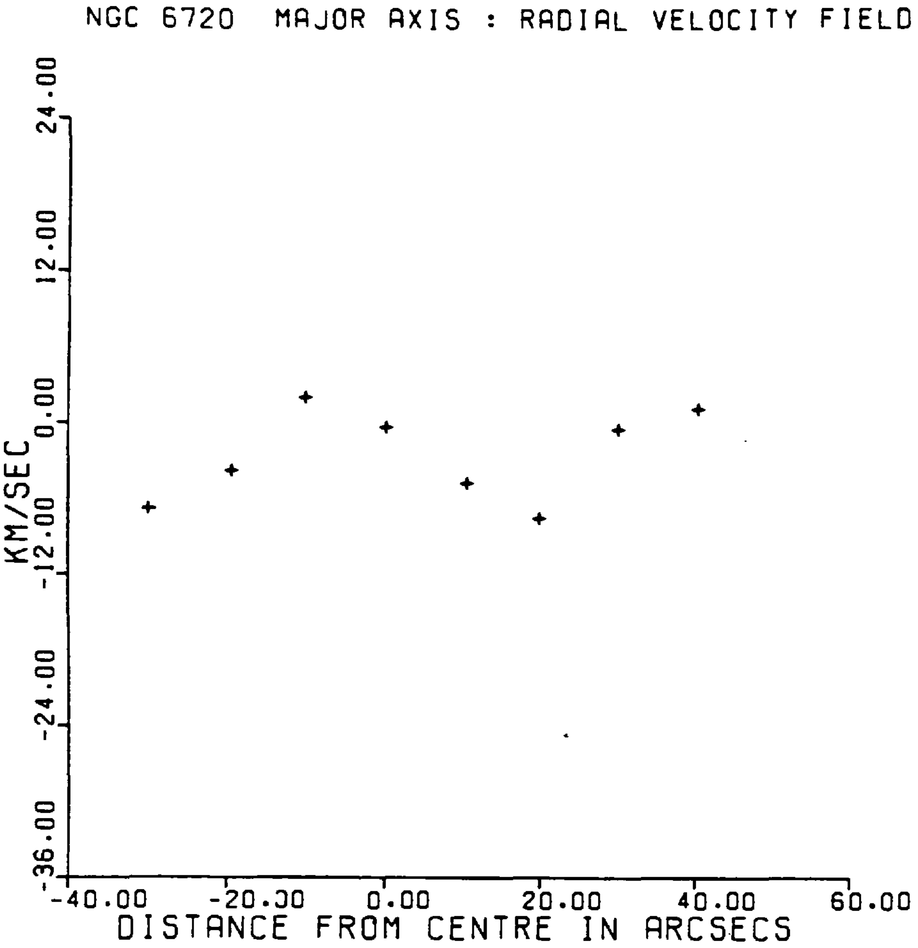
NGC 6720 MAJOR AXIS : RADIAL VELOCITY FIELD
24.00
12.00
0.00
-12.00
-24.00
-36.00
KM/SEC
-40.00
-20.00
0.00
20.00
40.00
60.00
DISTANCE FROM CENTRE IN ARCSECS

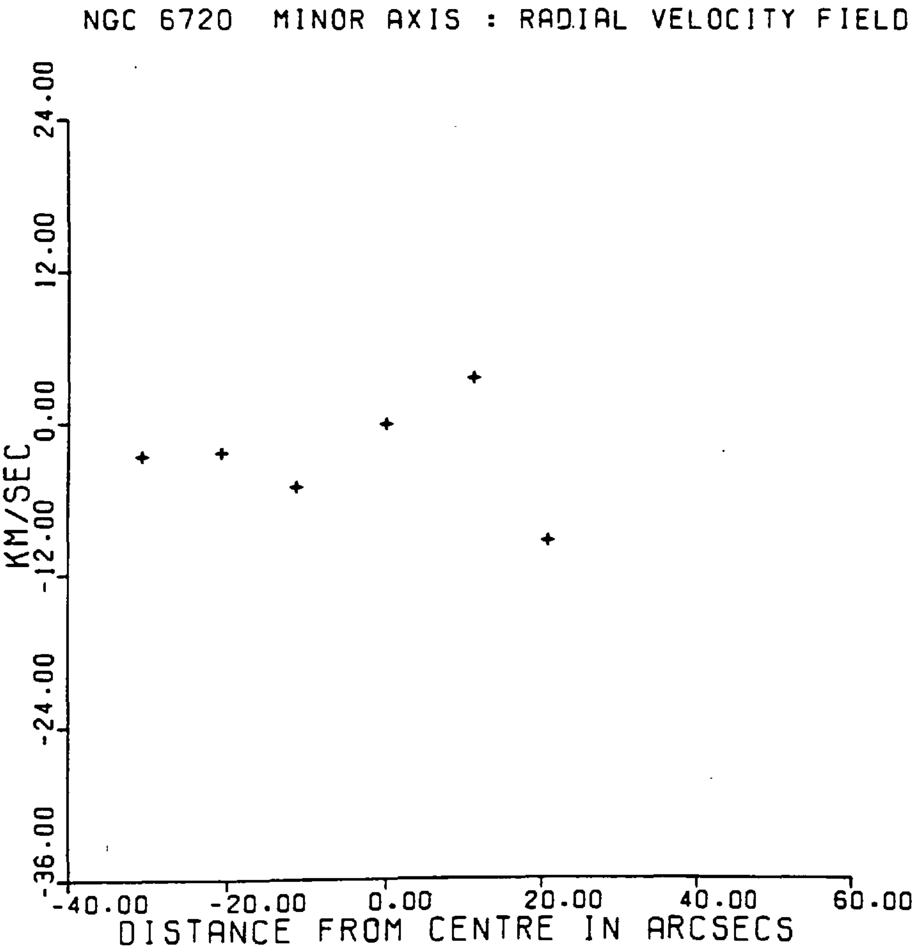
NGC 6720 MINOR AXIS : RADIAL VELOCITY FIELD
24.00
12.00
0.00
-12.00
-24.00
-36.00
KM/SEC
-40.00
-20.00
0.00
20.00
40.00
60.00
DISTANCE FROM CENTRE IN ARCSECS

FIGURE 4.12

(Weedman 1968) which would indicate that the axis of symmetry was not in the plane of the sky. In the following discussion, it is assumed that the λ4861Å Hβ emulsion distribution is representative of the general distribution of the nebular material.

### 4.2.6 The Form of the Nebular Envelope

On the basis of the data presented in the previous sections it is possible to draw several general conclusions regarding the structure of the nebular envelope:

Firstly, it seems clear that the envelope is spheroidal in nature. The line breadths and splitting in the central regions shows the presence of gas at both the front and rear of the central star. The flux from this gas is far too great for it to be dismissed as arising from the very faint outer envelope which is known to surround the ring structure, and is in agreement with levels determined from electronographic data. There may also be some slight evidence that the maximum splitting occurs slightly off the centre of the nebula, although the magnitude of this effect is comparable to the guiding errors, and it should therefore be treated with scepticism.

Secondly, a consideration of the mean radial velocity changes across the nebula (figure 4.12) shows that the mean radial velocities at opposite ends of the major and minor axes are the same, and equal to the mean radial velocity of the nebula. These positions were determined by taking the positions of best fits made using a Gaussian fitting program, described in section 3.4.4.3. In some cases it was not clear whether one or two components were present. In these cases only the major component has been plotted, but the error is, by the nature of the irregularity, small.

The model put forward by Hua and Louise (1970), Louise (1974), Ostebrock (1960) and Minkowski and Osterbrock (1960) of a toroid, inclined at an angle of $45^{o}$ to the line of sight, could explain the line splitting if the toroid was expanding radially and the opposite ends of the minor axis of the toroid overlapped along the line of sight. However, the mean radial velocity at opposite ends of the minor axis should then be different by exactly the same amount as the splitting observed at the centre. This is plainly not the case, and so the predictions of this model are at variance with the radial velocity data and the model must be discarded .

The model of Proisy (1974) (Figure 4.6) would predict a velocity gradient along the major axis, which is tilted at an angle of $30^{\circ}$ - $50^{\circ}$ to the line of sight. This is not apparent from Fig 4.12 and so this model is also in conflict with the observational data.

Thirdly, the electronographic data give a ratio of ring to central intensity for the Hβλ4861Å contour map of ∿3:1. This can be adequately explained in terms of a closed spheroidal shell model, which will be discussed later. If this were a prolate spheroid then, unless the major axis is at an angle of $\pi/2$ to the line of sight, a gradual change in radial velocity with position would be observed, this effect being most noticeable by comparing velocities at opposite ends of the axis (Weedman, 1968). Similarly, if this shell were an oblate spheroid, a velocity change along the minor axis would be expected.

Clearly there is little evidence for a velocity assymmetry along either axis, and there is thus no basis on which to distinguish between the oblate or prolate model.

### 4.2.7 Proposed Model

Phillips and Reay (1977) have proposed various model envelopes for NGC 6720. A section of one of these, oblate spheroidal in form, based on a model B ejection (see Appendix) is shown in figure 4.13(a). In this case the density C varies as $1/(r_I(\beta)r^2)$ where $r_I(\beta)$ is the internal radius of the shell at an angle $\beta$ relative to the stellar equatorial plane. Figure 4.13(b) shows a contour map, generated from this model, compared with the Hβ isophotal contour map for NGC 6720. A seeing disc of 3 arc secs was assumed, and the minor axis of the gas distribution was assumed to be at $^{\Pi}/_{2}$ to the line of sight, this being consistent with the radial velocity measurements presented in figure 4.12. The model is clearly an adequate representation, reproducing well the general shape of the ring structure and the observed intensity variations of the Hβ and [OIII] electronographs (Figure 4.7).

The extension of this model to reproduce the appearance of the nebula in lines from ions of low ionization potential, such as NII, OII, OI, is much more difficult. For these ions the ratio of the ring to centre intensities are of the order of 30:1. This can be reproduced by making the shell very thin, but in this situation the ring becomes unrealistically sharp (see Section A.2). However, there is

Figure 4.13

Model cross section

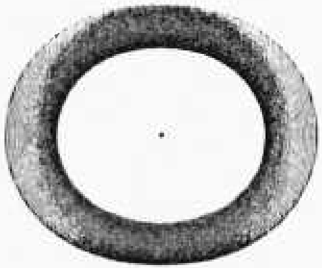

a

OIII Contour map

Model Contour map

b

evidence that these ions of low ionization potential arise from low temperature filaments and condensations (Boeshaar, 1974) and the shadowed regions behind them (Capriotti 1973) and as such they do not represent the overall structure of the nebula, mut merely reflect the degree of 'clumping' of the material present in the outer regions. This can be seen on a print of the electronograph taken in the light of [OI] λ6300Å which shows clearly the presence of sheet-like filaments. The observed ring to centre intensity ratio will obviously depend sensitively on whether these sheets form continuous shells and on the number of such shells or partial shells.

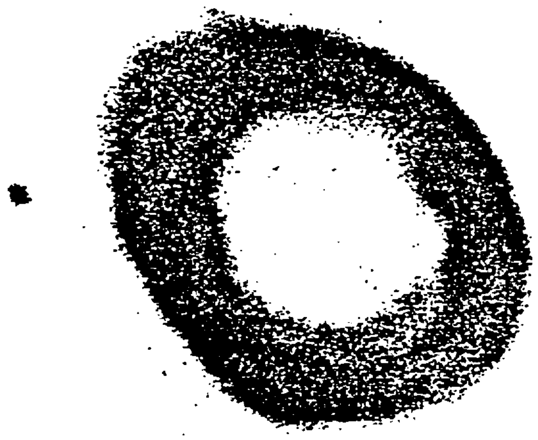

Figure 4.14 NGC 6720 [OI] 6300Å

## 4.3 NGC 7027

### 4.3.1 Description

NGC 7027 must certainly be the most observed of all planetary nebulae. It's irregular shape and high excitation has prompted many investigations of its structure, spectra and internal motions.

Photographic (Minkowski, 1968) and electonographic studies (Hicks, Phillips and Reay 1976) through narrow band pass filters centred on the hydrogen recombination lines in the optical region have shown that the ionized hydrogen distribution appears highly irregular. Since the large majority of planetary nebulae have at least some degree of symmetry it is reasonable to assume that this irregular appearance may be due, at least in part, to some obscuration lying along the line of sight. Support for this hypothesis was supplied by Miller and Mathews (1972) who found different amounts of reddening at three selected positions within the nebula.

Infra-red observations at 10$\mu$ by Gillett, Low and Stein (1967) revealed an unexpectedly large continuum level. This was interpreted as probably being due to thermal emission from dust internal to the nebula, being heated by absorption of optical UV radiation, particularly Ly$\alpha$.

These observations prompted the mapping of this object both in the radio continuum and in the infra-red.

In the radio observations have been made at 5 Ghz and 15 Ghz by Scott 1973, 1975 (Figure 4.15) and at 2.7 and 8.1 Ghz by Balick et al (1973). The 5 Ghz map of Scott (1973) shows a very regular bipolar structure of comparable size to the photographic data of Minkowski (1968).

The radio continuum at this frequency is composed mainly of free-free emission, ie electrons interacting with the Coulomb field of charged particles. Since hydrogen is by far the most abundant ion, the 5 GHz radio map is a reasonable representation of the ionized hydrogen distribution. At this frequency the dust will be transparent, as it is extremely small compared to the wavelength of the radiowaves ($\sim$6 cms).

In the infra-red Becklin et al (1973) have mapped this object at $10\mu$ (Figure 4.15) using a $1.\hat{8}''$ resolution element. Their results show a close similarity to the radio maps of Scott in that each shows an oval ring with a deep, central depression and no evidence for any surrounding low-brightness envelope. The bipolarity is markedly similar in both cases.

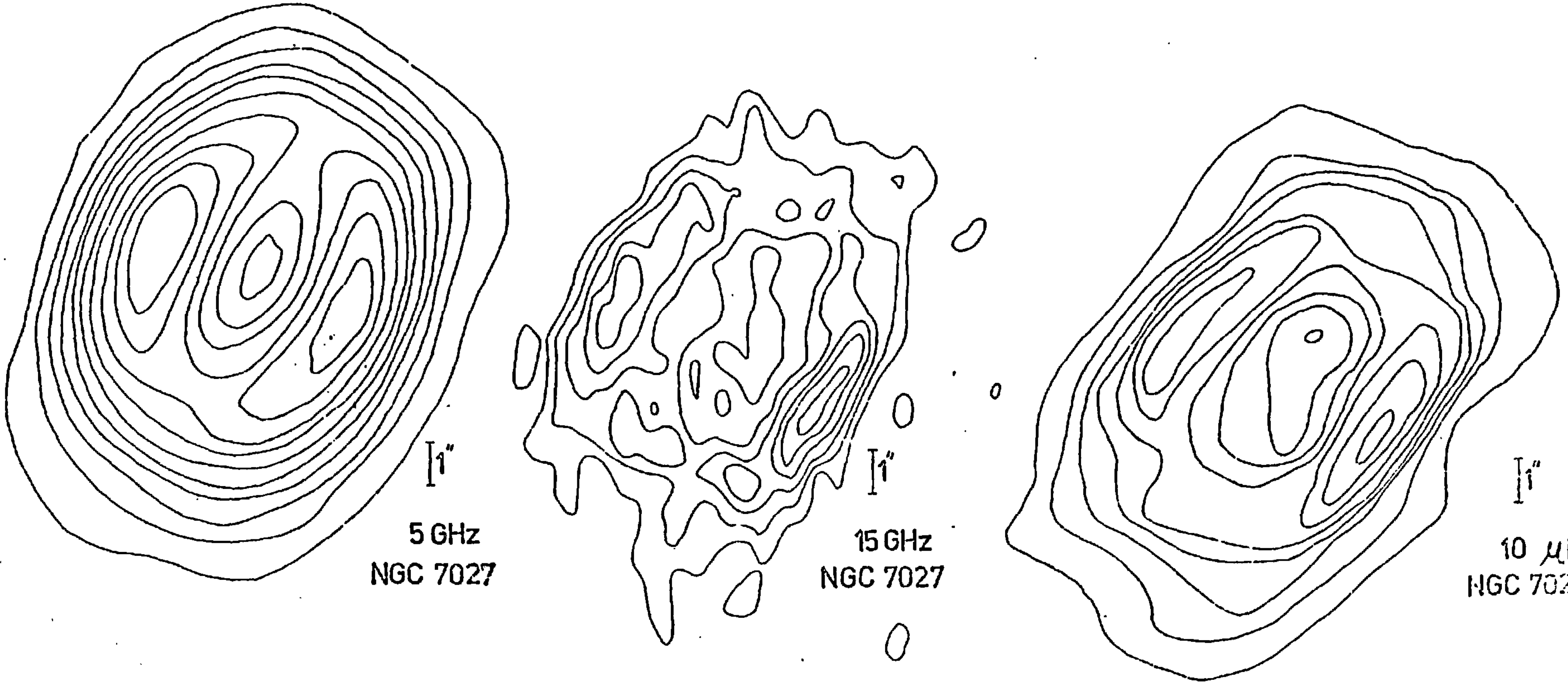

Figure 4.15

A comparison of this data with optical data taken in the light of Hα or Hβ (Minkowski (1968), Reay and Worswick (1977)) (Figure 4.16) indicates that there may be a particularly thick cloud of obscuring dust in front of the south west corner of the nebula, and variable, patchy extinction in front of the rest of the source. The nature of this dust, if indeed it is dust, is open to speculation although it has been suggested it may be composed of graphite or silicates.

The similarity of the 10μm and the 5 GHz maps indicate that the hot dust responsible for the 10μm emission excess, must be intimately mixed in with the gas.

Thus two separate regimes of extinction are present: hot dust uniformly and intimately mixed with the ionized gas, cold dust, external to, and partially obscuring, the optical image of the nebula.

The location of this external dust along the line of sight is quite uncertain, indeed it may itself be composed of several separate clouds. The lack of any apparent extinction over the 10μ map implies that the dust particles must be a good deal smaller than 10μ in order that they be effectively transparent. Possibly part of the external extinction may come from a circumnebular dust cloud whose nature and identity is obscured by some line of sight effect.

Figure 4.16

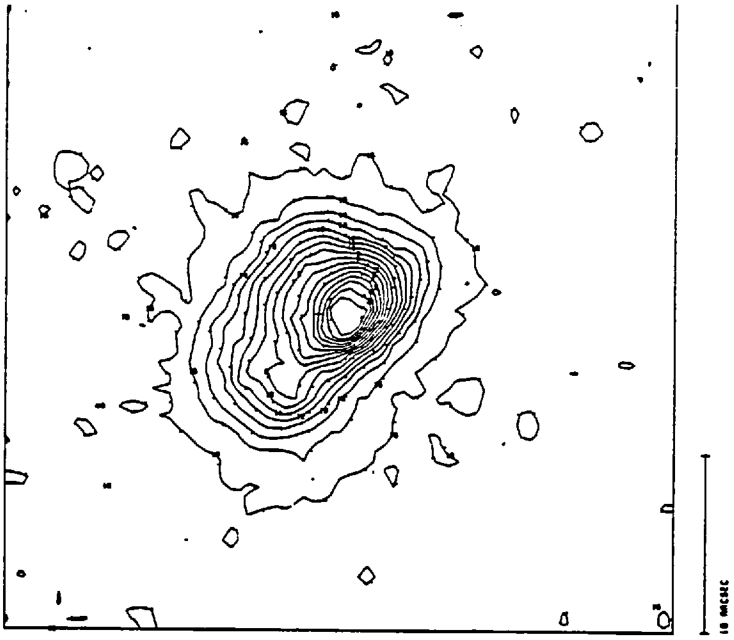

[OI] 6300 Å

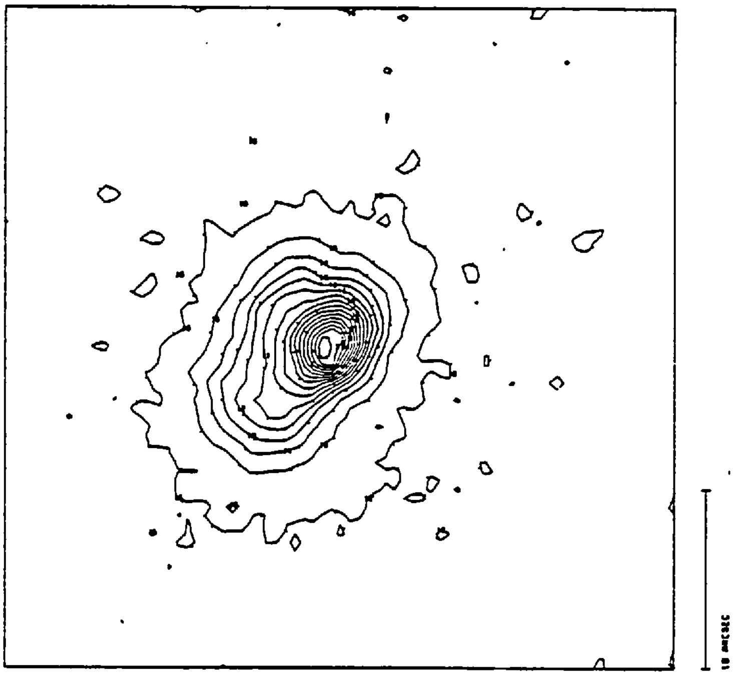

[O III] 5007 Å

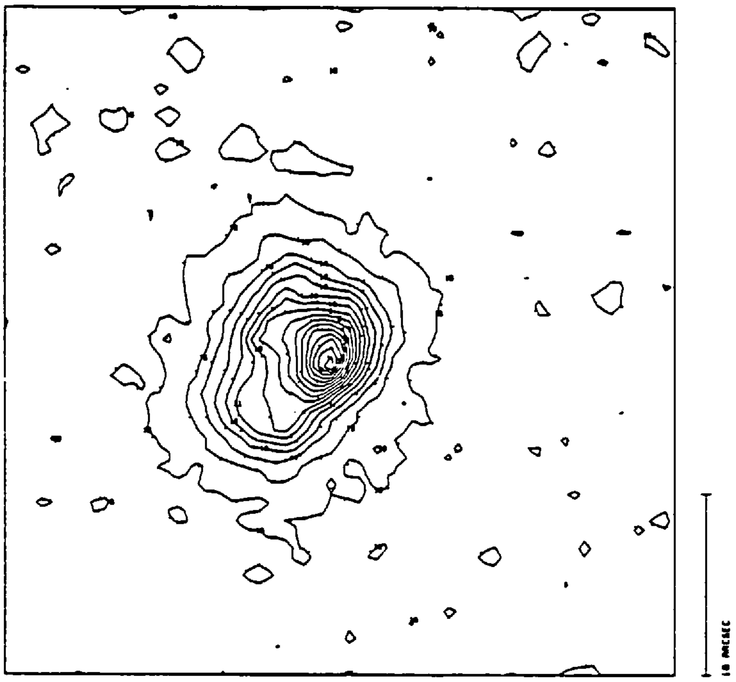

H 6563 Å

Figure 4.17

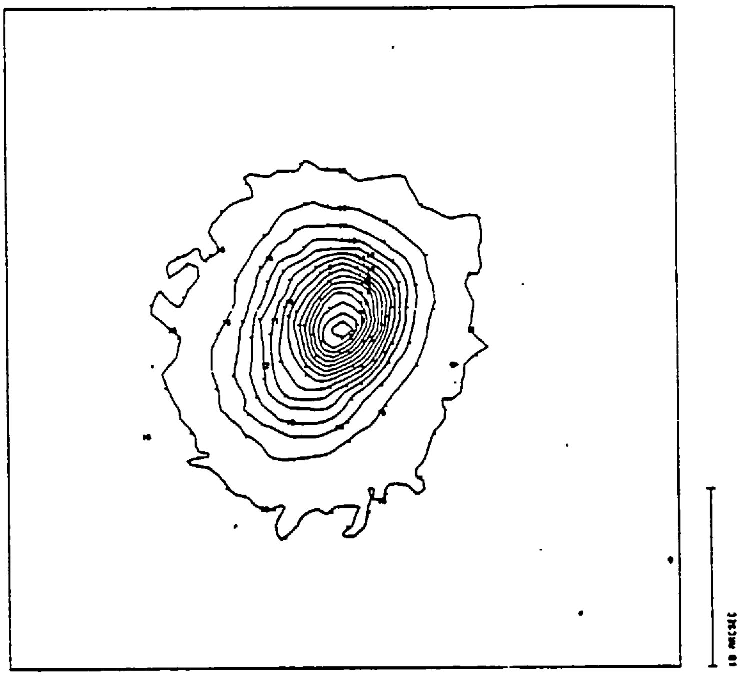

HE II
4686 A

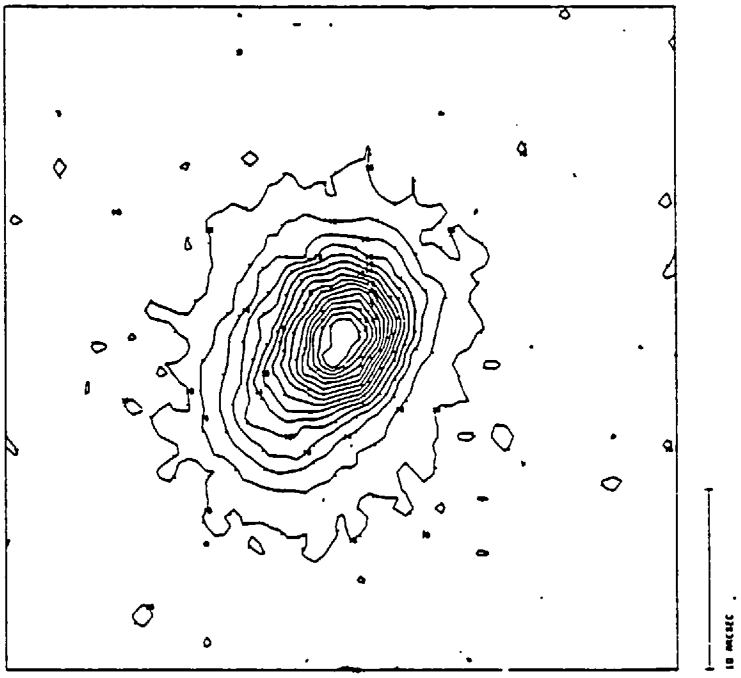

[NE III]
3868 A

Comparisons between the maps obtained in the radio and infrared with the optical maps are complicated by the uncertainties in the absolute positions of the optical data. Generally it is assumed that the optical 'hotspot' is coincident with the western bipolarity of the radio map. In this case the eastern radio component coincides with a lower brightness optical feature to the east of the major component whilst the relative minimum occuring in the centre of the radio emission is not apparent on the optical image.

Osterbrock (1974) attempted to investigate the amount and distribution of the dust internal to the nebula by means of observations of the Hydrogen recombination line profiles. As described in Chapter 1 the expansion velocity of a planetary nebula is known to split the nebular emission lines into two components, the red shifted component arising from the far side of the nebula, and the blue shifted component arising from the near side (Wilson 1950).

By comparing profiles of the Balmer lines which extend over a wide range in wavelength but which have emission coefficients that are very nearly proportional to one another, no matter what the temperature or degree of ionization, one can attempt to measure the effects of differential extinction due to any dust that may be between the near and far sides of the nebula.

However, because of the low mass of the hydrogen atom, the Balmer lines are thermally broadened to such an extent that any line splitting or structure is completely swamped. Hicks, Phillips and Reay (1976) have made observations of the less thermally broadened [OIII] λ5007Å line profile. Their results showed a line splitting of 27 km sec$^{-1}$ at the nebular centre, with the red shifted component consistently of lower intensity than the blue shifted component. This was interpreted as either a non uniform density or temperature structure in the envelope or as internal extinction amounting to approximately 0.34 magnitudes at the nebular centre.

In the next section the results of a more extensive study of the [OIII] line profiles, the visible spectrum and the optical image in the light of various ions are presented, followed by a discussion of the implications of these results for the structure of the nebula and the amount and location of the internal extinction.

## 4.3.2 Observations

The observations fall into two main sections:

1) Electronographic data concerning the appearance of the nebula in the light of various different ions, representing a wide range of ionization potentials. The lines were isolated using narrow band pass interference filters.

2) Spectrographic data obtained using a Fabry Perot Interferometer operating at a resolution of about 67,000. The shape of the 5007Å [OIII] line profile and its variation across the nebula was studied closely in order that dynamical and morphological information might be obtained. Essentially, this technique maps the radial velocity field of the object.

### 4.3.2.1. Electronographic Data

A selection of the electronographs obtained are presented in Figs 4.16, 4.17. These cover a fairly wide range of ionization potentials. Their most striking common characteristic is the similarity in the size, shape and structure of the image. For example the [OI] image is very similar to the [OIII] image whose ionization potential is 35.1 eV.

The HeII λ4686Å image (IP 24.4 eV) has the same general shape as the [OIII] λ5007Å image although the intensity fluctuations within the image seem less dramatic. Equally the [NeIII] λ3868Å image (41.1 eV) is very similar to that of He II λ4686Å. The Hα λ6563Å (I.P. = 13.6 eV) image displays the same qualitative characteristics as that of [OIII] λ5007Å, although the latter may be slightly larger. It should be remembered, however, that there is a tendency for image size to increase with exposure.

The lack of easily identifiable features in the image, such as bipolarity, complicates the task of assessing whether any trend exists relating the increase of the overall image size with decrease in ionization potential, such as would be found in a stratified nebula.

One approach is to measure the area contained within a contour level set at a small fraction, eg 1%, of the range between the peak surface brightness found in the image, and the background level. This will represent the outermost regions of the nebula, and, as it is a fraction of the range in surface brightness, will not be subject to a variation in size with variations in exposure. Table 4.18 gives the area contained within this 1% contour, which is the outermost level set on the maps shown in figures 4.16 and 4.17.

### 4.3.2.2 Radial Velocity Data

The spectral line profiles obtained at various positions across the optical image of NGC 7027 are shown in Fig 4.19(b). They are arranged in a grid of spacing $2.5\hat{''}$ R.A. and $3\hat{''}$ Dec and were obtained using a $5\hat{''}$ aperture in the outer regions and a $3.3\hat{''}$ aperture in the central regions. The profile at the radio centre was obtained using an aperture of $1.6\hat{''}$ diameter, in order that an accurate assessment of the expansion velocity might be made. Each scan has been normalized such that the variation in the intensity shown from scan to scan is representative of the variation in intensity of the optical image. Wavelength increases to the left.

## Table 4.18

Area inside contour level set at 1% of peak surface brightness.

| ION | Area (square") | Ionisation Potential (e$^{V}$) |
|---|---|---|
| [O I] 6300Å | 226.3 | |
| [OIII] 5007Å | 217.6 | 35.1 |
| H$\alpha$ 6563 Å | 200.3 | 13.6eV |
| HeII 4686 Å | 249.5 | 24.4 |
| [NeIII] 3868 | 251.4 | 41.1 |

The spatial relationship between these profiles and the 5 Ghz Radio map of Scott (1973) is shown in Figure 4.19(a) where the size of the circles represent the size of the entrance aperture.

Clearly the splitting of 33 km $sec^{-1}$ observed near the radio centre decreases towards the edges of the nebula where the two peaks merge into one single line.

A Gaussian fitting program of the type described in Chapter 3 has been used to fit Gaussians to these line profiles. One modification was made to the program, requiring that, in the case where two components existed, the halfwidths of the two Gaussians, although variable, had to be equal. Table 4.20 lists the parameters of the Gaussian fits in a grid in the same layout as the line profiles. From this it can be seen that the halfwidths of the Gaussians tend to increase as the distance from the centre of the nebula increases due to the larger spread in velocity along the line of sight (See section 2.3.2).

Figure 4.21 shows a plot of the mean positions of the Gaussian profiles against the interferometer step position from data taken along a line almost parallel to the major axis of the 5 Ghz radio map. Where two

Figure 4.19(a)

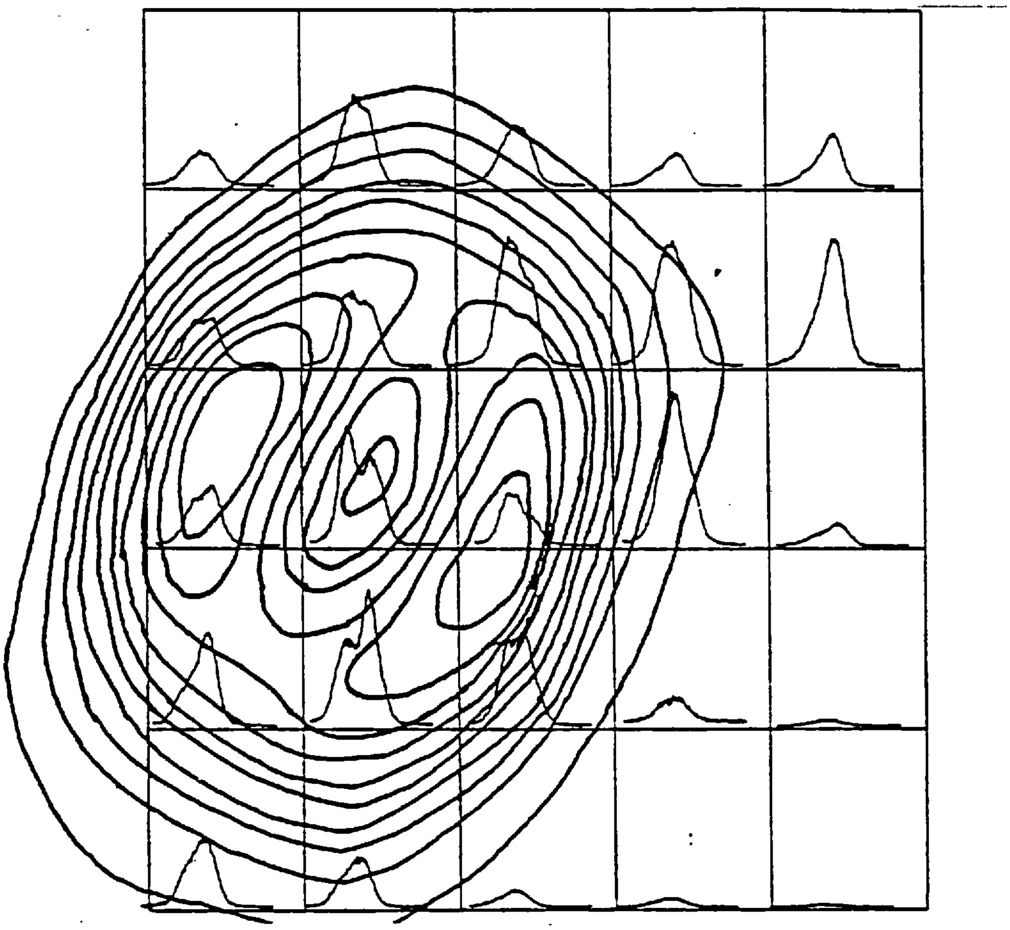

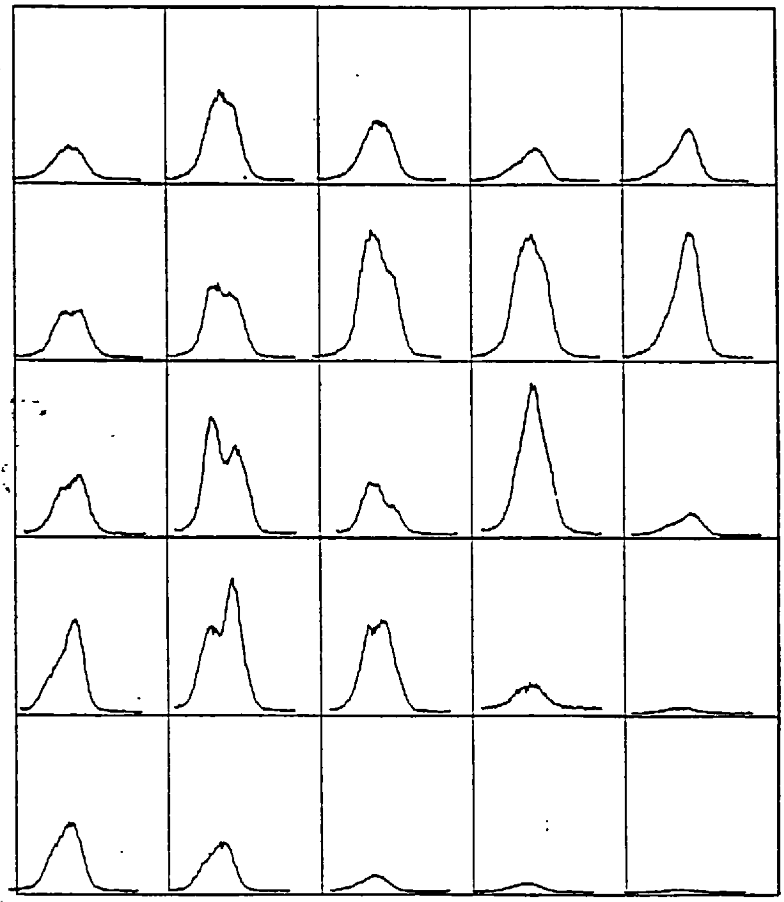

Figure 4.19(b)

Table 4.20

| | | | | | |
|---|---|---|---|---|---|
| $^{IB}/_{IR}$ | 5.06 | 1.15 | 2.28 | 2.92 | 3.81 |
| Half width | 400 | 358 | 355 | 316 | 313 |
| $P_B$ | 3731 | 3911 | 3872 | 3838 | 3832 |
| $P_R$ | 3481 | 3580 | 3586 | 3526 | 3501 |
| Mean Position | 3606 | 3745.5 | 3729 | 3682 | 3666 |
| Splitting | 250 | 331 | 286 | 312 | 331 |
| $^{IB}/_{IR}$ | 1.16 | 0.84 | 0.67 | 1.07 | 4.49 |
| Half width | 307 | 296 | 309 | 328 | 325 |
| $P_B$ | 3828 | 3877 | 3904 | 3887 | 3848 |
| $P_R$ | 3574 | 3590 | 3630 | 3646 | 3530 |
| Mean Position | 3701 | 3733 | 3767 | 3766 | 3689 |
| Splitting | 254 | 287 | 274 | 241 | 318 |
| $^{IB}/_{IR}$ | 1.60 | 0.75 | 0.68 | - | 2.56 |
| Half width | 294 | 284 | 304 | - | 314 |
| $P_B$ | 3815 | 3920 | 3904 | - | 3860 |
| $P_R$ | 3555 | 3582 | 3625 | - | 3540 |
| Mean Position | 3685 | 3751 | 3764 | 3789 | 3700 |
| Splitting | 260 | 338 | 279 | - | 320 |
| $^{IB}/_{IR}$ | 2.61 | 1.59 | 1.19 | 1.61 | 0.92 |
| Half width | 280 | 294 | 330 | 355 | 423 |
| $P_B$ | 3736 | 3844 | 3841 | 3812 | 3781 |
| $P_R$ | 3438 | 3511 | 3601 | 3606 | 3636 |
| Mean Position | 3587 | 3678 | 3721 | 3709 | 3708 |
| Splitting | 298 | 333 | 240 | 206 | 145 |
| $^{IB}/_{IR}$ | 1.94 | 2.1 | 4.16 | 2.24 | 1.17 |
| Half width | 297 | 297 | 348 | 358 | 450 |
| $P_B$ | 3713 | 3717 | 3695 | 3736 | 3667 |
| $P_R$ | 3461 | 3456 | 3402 | 3515 | 3625 |
| Mean Position | 3587 | 3586 | 3549 | 3626 | 3646 |
| Splitting | 252 | 261 | 293 | 221 | 42 |

Calibration: 1.64 mÅ per step

components exist in a line profile, the mean position has been used. The vertical error bar represents guiding errors whilst the horizontal bar represents wavelength drift in the F.P. This shows a tendency for the mean spectral line position to change uniformly along the major axis of the radio nebula. Data for the minor axis is less reliable as there is no symmetry of the profile positions along this axis, ie it runs between various scans and there are only three data points. However a plot has been produced and it is shown in Figure 4.22.

Where a profile consists of two components the relative heights of these profiles varies considerably over the nebula. The symmetry of the radio emission observed by Scott (1973) and the I.R. emission observed by Becklin et al (1973) implies that the variations in these profiles ought to be symmetrical. This is however rather difficult to assess. A rough idea of the symmetry of the variations in heights of the componenets may be obtained by looking at the mean value of the ratio $^{I_B}/_{I_R}$ for the scan of the radio centre and the eight scans immediately surrounding it. This gives a mean value of $^{I_B}/_{I_R} = 1.23 \pm 0.63$. Clearly the effect is slight and the errors are large. The value depends sensitively on the spatial positioning of the line profiles with respect to the radio centre, and

NGC 7027 Major Axis Radial Velocity

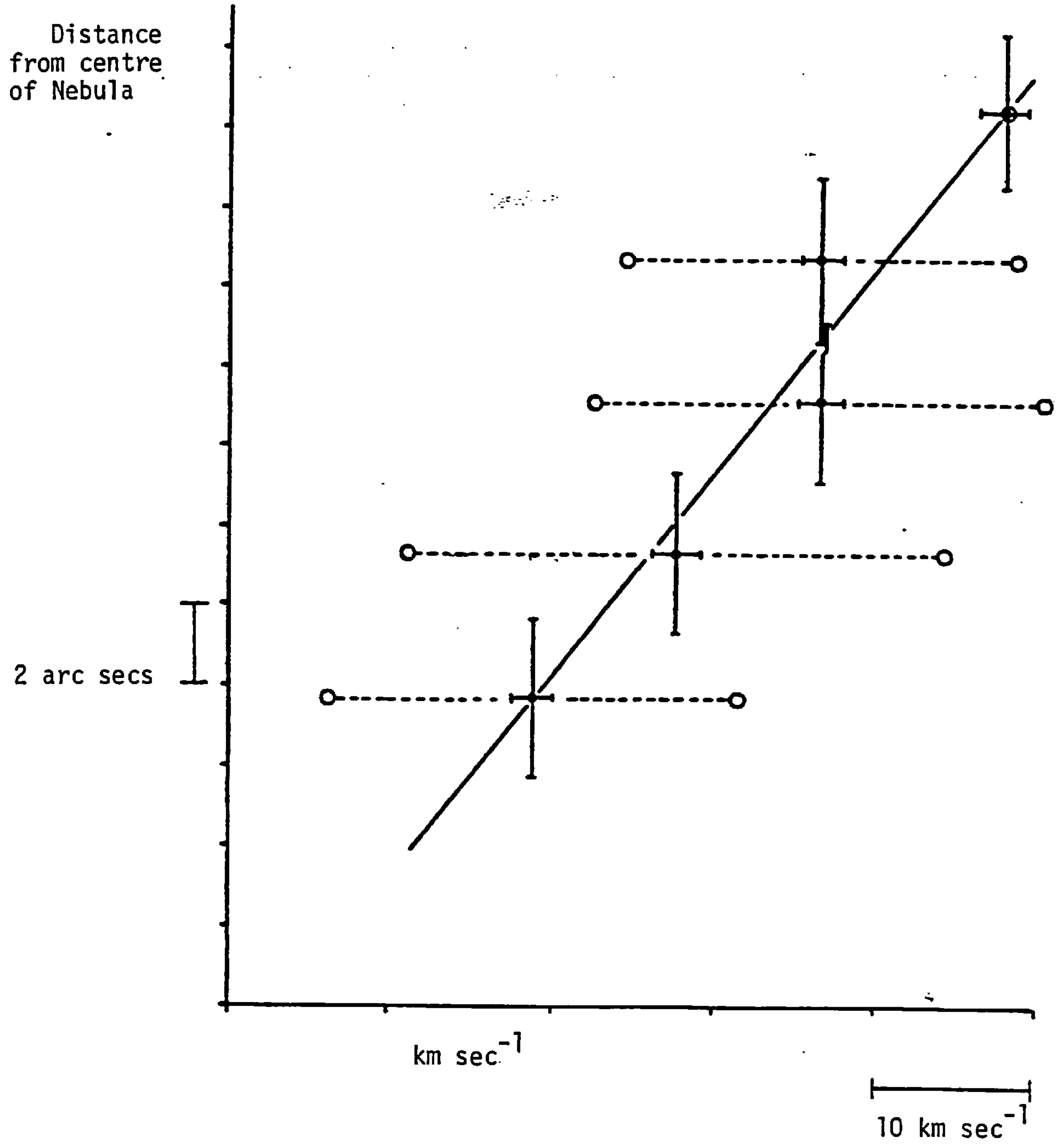

Figure 4.21

NGC 7027 Minor Axis Radial Velocity

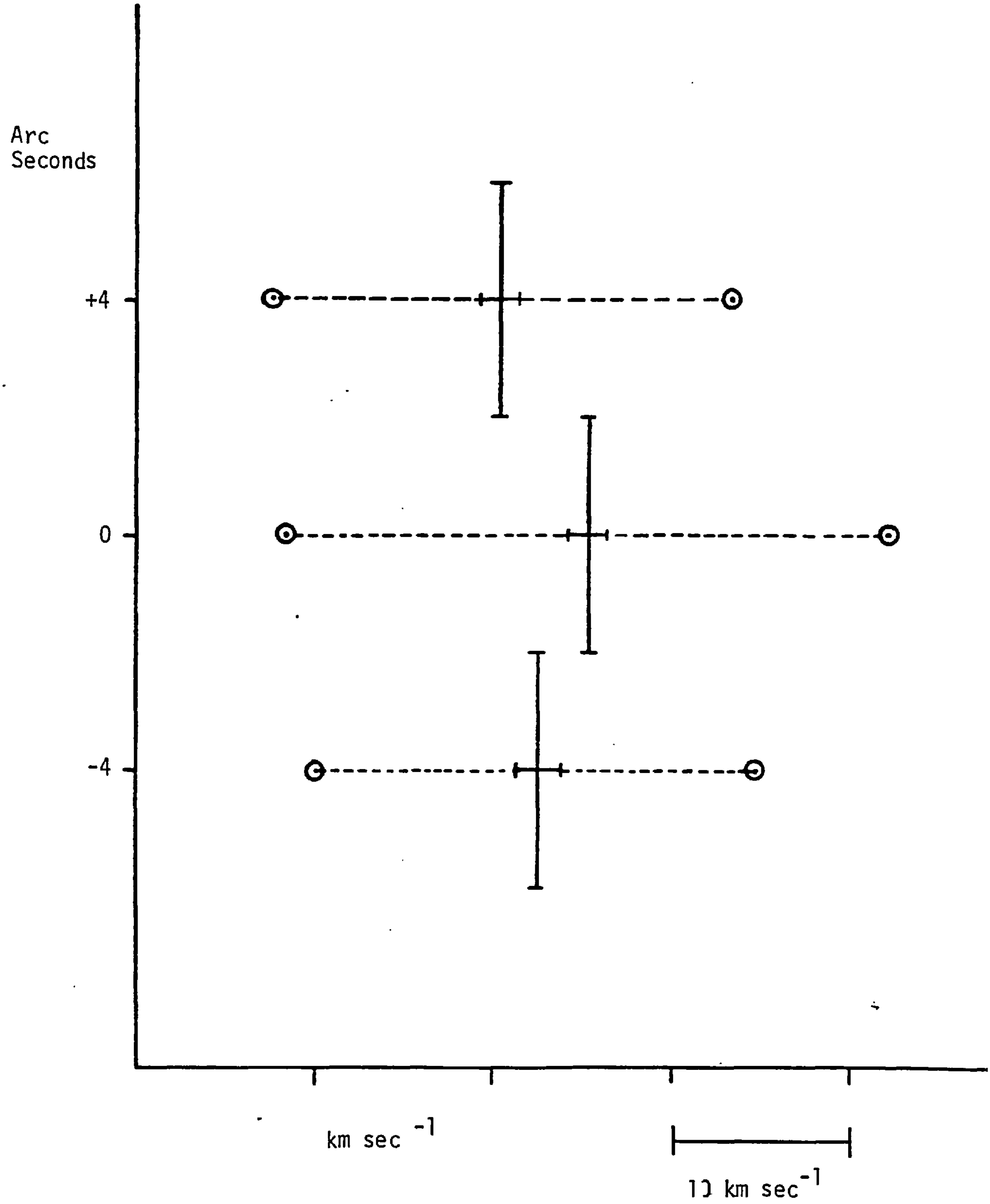

Figure 4.22

also on the interpretation of the profiles as consisting of two distinct components. Large errors may be incurred by fitting two profiles when the splitting is small and the profile only slightly assymmetric. When the average is taken over all the profiles a value of $^{I}B/_{I_R}$ of 1.6 ± 0.8 is found ignoring scans where two components seem unlikely.

### 4.3.3 Discussion

On the basis of these observations it is possible to draw several general conclusions concerning the nature of the nebular envelope.

a) The anomalously large size of the [Ne III] λ3868 emitting region compared with Hα in relation to its ionization potential, implies that the nebula may in fact be radiation bounded rather than density-bounded. Theoretical models computed for stellar temperatures of $10^{5\circ}$k with a black-body input radiation field show that [Ne III] can maintain a relatively high abundance into the HII → HI transition region (Flower 1969). The existence of neutral material surrounding the nebula has been investigated by Thompson and Colvin (1970) who searched for indications of absorption at 21 cms in the thermal radio emission. They found no evidence for any significant absorption but were able to give an approximate estimate of the mass of neutral material of less than 0.23 M⊙. This compares with the mass of the ionized gas in the nebula which has been estimated as $\sim$ 0.25 M⊙ by Wynn-Williams (1970) on the basis of observations of the 5 Ghz free-free continuum flux. The existence of an expanding extended sphere or shell of gas surrounding NGC 7027 of about $38\hat{''}$ RA x $62\hat{''}$ Dec has been reported by Mufson et al (1975) on the basis of measurements of the $^{12}$CO emission at 115 Ghz. The mass associated with this CO emission is estimated to be $\sim$ 1.4M⊙ although this is sensitive to the distance adopted for the nebula, being proportional to $R^3$. The ratio of this mass to the mass of the ionized gas is large and increases if the nebula is assumed closer, whilst the absolute value of the mass of the neutral material increases if the nebula is assumed further away.

Current stellar evolution theory suggests that stars in the range 1 → 4 M⊙ are the progenitors of planetary nebulae so total ejecta of up to 3 M⊙ seem a possibility. However the inability of Thompson and Colven to detect the presence of any neutral hydrogen absorption suggests that this cloud may be hydrogen deficient. The possibility that the cloud may be a chance superposition along the line of sight is discounted by the excellent agreement in position and velocity of the CO emission when compared to the nebula.

b) It seems possible to interpret the observed variations in the line profiles in terms of a closed shell. The observed symmetry of the 5 Ghz map of Scott (1973), the 10μ map of Becklin et al (1973) and the 15 Ghz map of Scott (1976) implies some kind of shell like structure. Scott (1973) argued that this could be interpreted in terms of a cylindrical structure, tilted at 30° to the line of sight, although this was discounted by Hicks et al (1976) on the basis of line profile observations.

The observations reported here allow the dismissal of Scott's model, as it implies a constant velocity splitting of the line profile along the major axis, which is not found (Table 4.20).

The observed tendency for the mean position of the spectral line to change uniformly along the major axis of the nebula (Fig 4.21) allows the interpretation of the velocity structure in terms of a prolate spheroid tilted to the line of sight. The gradient K' of the graph shown in Fig 4.21 is 1.9 km $\sec^{-1}$ arc $\sec^{-1}$.

Assuming that the velocity of expansion V of the nebula is directly proportional to the radius R and taking the observed expansion of 33 km sec $^{-1}$ and the distance from the centre of the radio nebula to the centre of the bipolarity, where the peak of the emission occurs, of 2.25 arc seconds, we find that V = kR where k = 7.3 km sec$^{-1}$ arc sec$^{-1}$.

It is possible to relate k to k' by means of a simple model (Fig 4.23).

From Figure 4.23 we see that

$$V' = kR \cos \theta = k'd \qquad (4.1)$$

and $$d = R \sin \theta \qquad (4.2)$$

hence $$\frac{k}{k'} = \tan \theta \qquad (4.3)$$

Thus $$\theta = \tan^{-1} \frac{k}{k'} \qquad (4.4)$$

Substitution of the observed values of k and k' give a value for $\theta$ of $\sim 75^{\circ}$ indicating that the major axis of the nebula is tilted at an angle of $15^{\circ}$ from the perpendicular to the line of sight, the NE end expanding towards us and thw SW end receding from us.

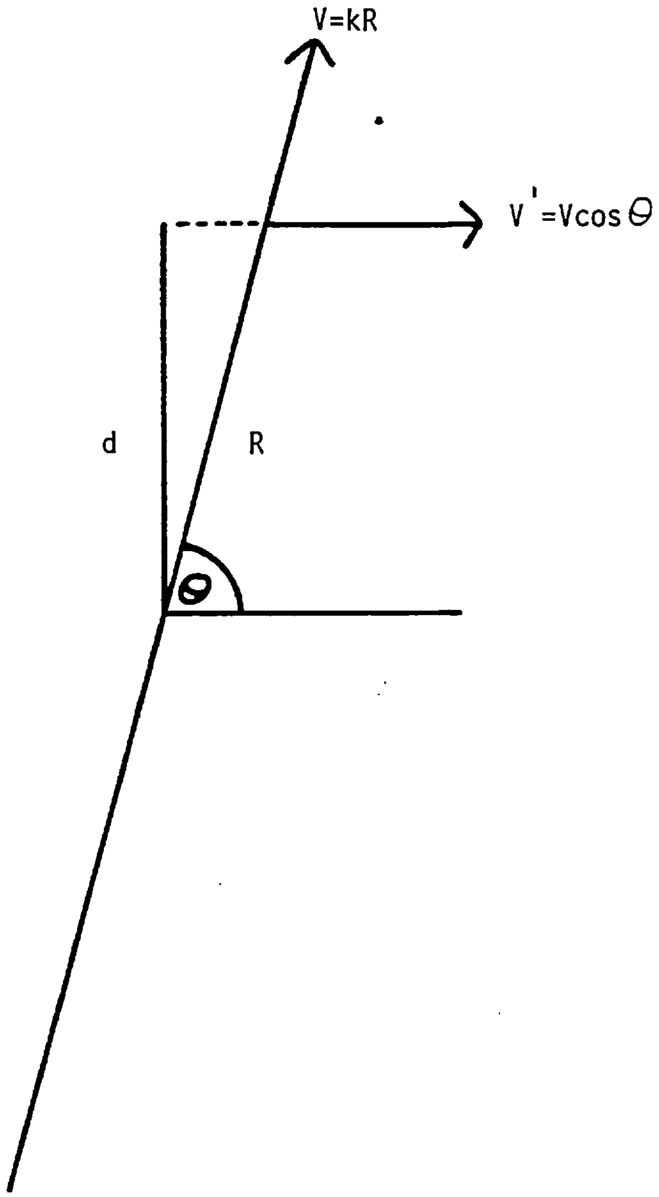

Figure 4.23 Tilt Model

This interpretation of the nebula is supported by the observation that the halfwidths of the fitted profiles increases towards the edges of the nebula, as the range of velocities across the entrance aperture increases in a manner similar to that described in Section 2.3.2.

Furthermore if the density in the nebula, $\rho$, is assumed to vary inversely with radius R as $R^{\alpha}$, where $\alpha$ is positive, then the central regions of the nebula, being closer to the central star, will be more dense than the outer regions. This is supported in part by the observations of Kaler et al who postulate the existence of a dense central region, where the electron density could be as high as $10^{7} cm^{-3}$.

Electronographic data obtained on the [S II] λ6717,6731 lines indicate little variation in the ratio $\lambda 6731/_{6717}$ which is density sensitive. The ratio map is shown in Figure 4.24. These lines arise mainly in the outer, lower excitation regions, indicating fairly constant density in this area.

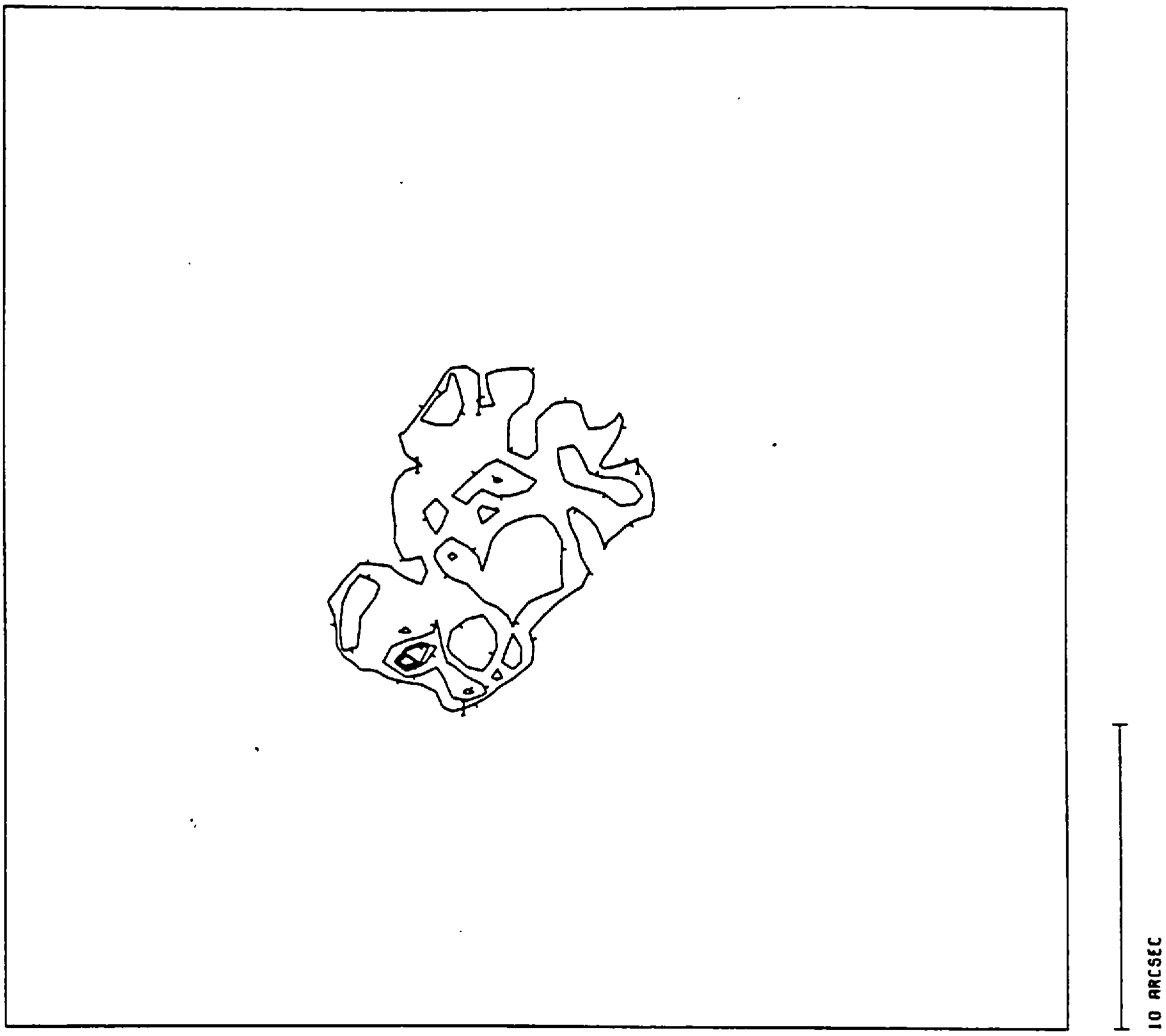

NGC 7027 SII RATIO 6731/6717

2 SIGMA LIMIT OX=10 OY=15

PLOT OF COMPLETE SCAN WITH A BLOCKING FACTOR OF TWO

CONTOURS ARE SMOOTHED

Figure 4.24

c) Having established the symmetrical form of the nebular envelope, the significance of the average ratio of $^{I_B}/_{I_R}$ may be discussed.

The value for $^{I_B}/_{I_R}$ of 1.23 ± 0.63 quoted in the last section indicates a tendency for the red-shifted profile to be attenuated with respect to the blue-shifted profile. This is probably due to the dust which is mixed in with the gas. The amount of extinction present may be estimated on the basis of a simple model representing the two sides of the shell.

It is assumed that the intensity of the emission per unit volume, Io, is constant, and that the absorption per unit distance K is constant.

The optical depth $\zeta$ is given by

$$\zeta = \int k dx = kx \qquad (4.5)$$

Thus the residual intensity I which is left after attenuation over a distance x is given by:

$$I = I_o e^{-kx} \qquad (4.6)$$

Referring to figure 4.25 consider the emission arising from a point $-(x_o + a)$

At $x = o$ the residual intensity is given by:

$$I = \left[I_o e^{-kx}\right]_{x=-(x_o+a)}^{x=x_o} = I_o e^{-ka} \qquad (4.7)$$

At $x = +\infty$ the residual intensity is given by

$$I = (I_o e^{-ka}) \left[e^{-kx}\right]_{x=x_o}^{x=x_o+a} = I_o e^{-2ka} = I_R \qquad (4.8)$$

We may compare this with the residual emission intensity arising from a point at $x = x_o$, at $x = +\infty$

$$I = \left[I_o e^{-kx}\right]_{x=x_o}^{x=x_o+a} = I_o e^{-ka} \qquad (4.9)$$

Thus $I_B/I_R = e^{ka}$ (4.10)

Clearly any emission arising between $x = (-x_o)$ and $x = (x_o + a)$ will be attentuated by a factor $e^{ka}$ with respect to emission arising between $x = x_o$ and $x = x_o + a$.

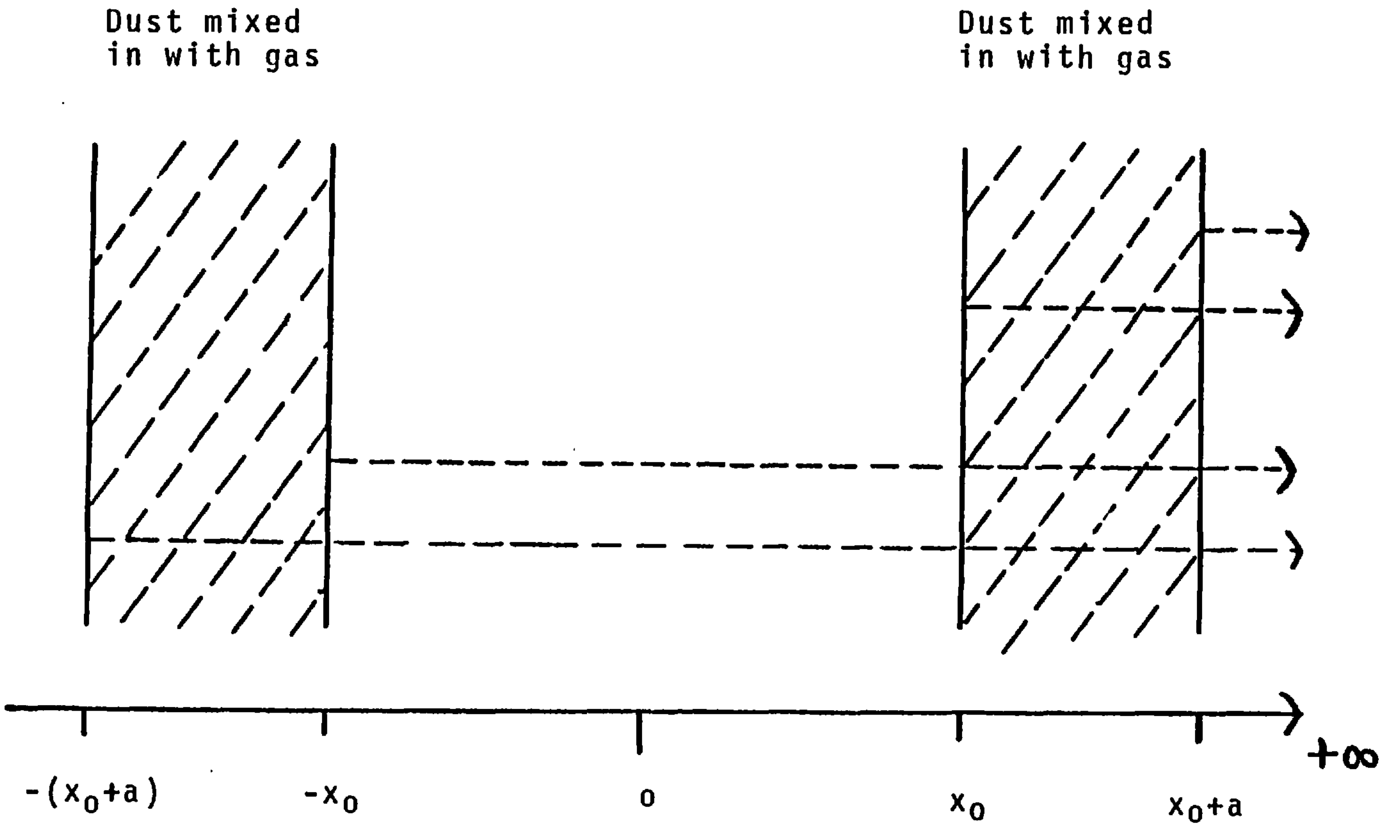

Figure 4.25 Dust Model

Thus:

$$ka = \log_e \frac{I_B}{I_R} = 0.21 \begin{smallmatrix} + 0.41 \\ - 0.72 \end{smallmatrix}$$

An accurate value for a, the shell thickness, is unavailable, although Scott (1973) was able to set an upper limit of $1.5\hat{''}$. To convert this to a distance one requires the distance of the nebula.

Using $a = 1.5\hat{''}$

$$k = 0.14 \text{ per arc second}$$

Using the distance determined by Cahn and Kaler (1971) of 1.3 kpc we find

$$k = 0.72.10^{-17}\text{cm}^{-1}$$

More recently Torres, Peimbert and Peimbert (1977) have derived a distance of ∿ 0.6 kpc, implying a value of

$$k = 1.53.10^{-17}\text{cm}^{-1}$$

This may therefore be regarded as an upper limit on the value of k.

### 4.3.4 Conclusions

NGC 7027 appears to be prolate spheroidal in form, expanding at a velocity of 33 km/sec with its major axes tilted at about 15° from being perpendicular to the line of sight. Asymmetries in the line profiles allow the derivation of an upper limit for the absorption coefficient of

$$k_{max} = 1.5.10^{-17}cm^{-1}$$

with a more probable value of $\sim 0.72.10^{-17}cm^{-1}$ although these values are sensitive to the distance of the nebula.

The anomalously large size of the NeIII ionized region indicates that the nebula is probably radiation bounded, suggesting that the variable external extinction is due, at least in part, to material immediately surrounding the nebula, rather than being due to a chance superposition along the line of sight.

# CHAPTER 5: THE USE OF A FABRY PEROT INTERFEROMETER WITH MULTI-POINT DETECTORS

## 5.1 Introduction

A practical limitation to the spatial resolution attainable when mapping an object using a single point detector is set by the accuracy with which the aperture can be relocated on the object. When using a multi element detector information is obtained at all points simultaneously and the spatial resolution is set by the size of the array-element or pixell, or by the guiding errors, or by the seeing, whichever is the greater. Ideally the size of the pixell should be comparable to the size of the seeing disc. In this situation the spatial relationship of any two points on the nebula is fixed only by the geometry of the detector.

In the first part of this chapter a new technique is proposed for studying the three dimensional variations in electron temperature and density, using a Fabry-Perot Interferometer coupled to a multi-element array detector. This is followed by a detailed discussion concerning the use of an F.P. in this mode. The various detectors which are readily available are considered in terms of their suitability for this work. The data processing techniques required to correct the various field distortions introduced by the F.P. are then described. Finally the various methods which may be used to analyze data acquired in this way are outlined. The implications of these techniques for the data acquisition process are considered.

## 5.2 Three Dimensional Mapping of Electron Temperature and Density.

It is well known that the ratio of various emission lines which arise in planetary nebulae are sensitive to variations in electron temperature $T_e$ and number density $N_e$. (Seaton, 1960). The mapping of these variations in Te and Ne across an object, by ratioing contour maps taken of these lines, is rapidly becoming an established technique (Reay and Worswick 1978). However these contour maps are obtained by taking exposures through interference filters of 5-10Å bandwidth. This is too low a resolution to actually resolve the line profiles, and so the maps obtained are a summation of all points along the line of sight. In this sense the maps obtained are only two-dimensional.

It is also well known that the emission line profiles obtained from planetary nebulae are broadened and split due to the Doppler shift imposed by the expanding nebular envelope. It has also been established that the expansion velocity at any point in the shell is a function of the radial distance from the centre (Weedman, 1968).

It is possible, therefore, to use the Doppler shift of the profile to map out the variations in emission in a third dimension: along the line of sight.

So far the Fabry Perot Interferometer described earlier has only been used with a single point detector. This means that the emission line profiles from different parts of the nebula must be obtained sequentially, the telescope being offset to provide a map across the object. This procedure is subject to large setting errors, especially on small objects, and in many cases the spatial relationship between observations taken on different nights is unclear.

The advantages of using a two dimensional array detector lie mainly in the multiplexing advantage of obtaining data on many points simultaneously but also in the reliability of the spatial relationship of the various points.

It appears possible then to build up a three dimensional array of data which corresponds to the three dimensional variation in nebular emission by scanning the F.P.I. and taking several exposures..

By acquiring data on a pair of the temperature or density sensitive lines and ratio-ing them at the same points in velocity space, the variations in $N_e$ or $T_e$ in three dimensions may be derived.

There are, however, limitations to the extent of the nebula which may be mapped, depending upon where the lines in question originate.

In general, the temperature sensitive ratio of the [OIII] lines $\frac{\lambda(4959 + 5007)}{\lambda\ 4363}$ may be used to probe the ionized hydrogen distribution. When studying the outer regions of a nebula, and the distribution of density condensations in the envelope, the best lines to use are those of the low ionization potential ions such as $N^+ . \frac{\lambda(6548+6583)}{\lambda 5755}$ which is temperature sensitive or

$$O^+ \ \frac{\lambda 3729}{\lambda 3726} \quad \text{and} \quad S^+ \ \frac{\lambda 6716}{\lambda 6731}$$

which are density sensitive.

Lines arising from ions such as ClIII, ArIV and KV are also density sensitive but in practice are too faint to be of use.

### 5.2.1 Ratioing

In order to produce a ratio map which is accurately calibrated in Te or Ne there are several processes which must be performed on the data:

#### 5.2.1.1 Flat-field calibration

This involves the removal of systematic fluctuations in detector sensitivity across the field. The size of the fluctuations, due mainly to photocathode variations, differs from tube to tube. If the exposures are located on the same area of the photocathode, which is true for instance of a channel plate photomultiplier tube, but not necessarily for the electronographic camera, then the variations in sensitivity will automatically be corrected during the ratioing process, provided that the exposures are close enough in wavelength that the variations will be the same, and also that the background level has been accurately determined and removed.

The need to correct each exposure for sensititivy variations is a weighty argument against the suitability of use of the electronographic camera for this work.

#### 5.2.1.2 Spatial Matching

It is obviously necessary to match the two arrays spatially before ratioing. Clearly, when the detector is fixed with respect to the photocathode, if the telescope remains tracking on the object, there will be no problem in overlaying exposures spatially.
Again, however, in the spectracon the electronographic emulsion, which is the detector, is not fixed with respect to the photocathode. Each exposure is taken on a different part of the film. Variations in the position of the film may be as much as several millimetres, which is, typically, the diameter of the object being observed.

The spatial relationship may be defined using field stars, provided they are sufficiently bright. This, however, is unlikely due to the very narrow bandwidth of the filter. It is possible to put fiducial marks on the film via photocathode non uniformities, or by using a suitable registration mask.

### 5.2.1.3 Spectral Matching

When ratioing two lines of different wavelengths it is essential that they are ratioed at the same points in velocity space.

In order to determine the relation between scans of different wavelengths we need to know the gap t. Thus at $\lambda_1$ the order $n_1$ is given by:

$$n_1 \lambda_1 = 2t$$

Clearly if the order is to be determined sufficiently accurately that no degradation of resolution results from the ratioing process then t must be determined to better than ½N of an order where N is the finesse.

This implies an accuracy of $\frac{\lambda}{4N}$ in the value of t.

The absolute wavelengths of the lines being observed are known very accurately in advance. However any relative motion between the observer and the object will Doppler-shift these lines. The accuracy with which this Doppler-shift is known also affects the determination of the relative positions of the lines in velocity space.

Consider two lines of wavelength $\lambda_1$ and $\lambda_2$. The acceptable error $\delta\upsilon$ in the relative velocity may be determined in the following way. The Doppler-shift in the lines $\delta\lambda_1$ and $\delta\lambda_2$ are given by the non-relativistic Doppler equation:

$$\delta\lambda_1 = \lambda_1 \frac{\delta\upsilon}{c} \quad ; \quad \delta\lambda_2 = \frac{\lambda_2 \delta\upsilon}{c} \qquad (5.1)$$

The inter-order spacing $\Delta\lambda$ at $\lambda_1$ and $\lambda_2$ is given by

$$\Delta\lambda_1 = \frac{\lambda_1^2}{2t} \quad ; \quad \Delta\lambda_2 = \frac{\lambda_2^2}{2t} \qquad (5.2)$$

The error is introduced because $\delta\lambda_1$ is a different fraction of $\Delta\lambda_1$ than $\delta\lambda_2$ of $\Delta\lambda_2$ producing a relative phase shift between the profiles.

If we limit this error to being less than ½N of an order (where N is the finesse) - a typical scan increment - then we obtain the inequality

$$\frac{\delta\lambda_2}{\Delta\lambda_2} - \frac{\delta\lambda_1}{\Delta\lambda_1} < \frac{1}{2N} \qquad (5.3)$$

where $\lambda_2 > \lambda_1$

Substituting from 5.1 and 5.2

$$\frac{2t}{\lambda_2}\frac{\delta\upsilon}{C} - \frac{2t}{\lambda_1}\frac{\delta\upsilon}{C} < \frac{1}{2N} \qquad (5.4)$$

hence

$$\frac{\delta\upsilon}{C} < \frac{1}{4Nt} \cdot \frac{\lambda_2\lambda_1}{\lambda_1-\lambda_2} \qquad (5.5)$$

This means that in the worst case ratioing the $\lambda5007$ and $\lambda4363$ lines of doubly ionized oxygen, with $t = 500\mu$ and $N = 30$, then $\delta\upsilon/_C < {}^1/30{,}000$ ie $\delta\upsilon < 10$ km/sec. Clearly as $\lambda_2 - \lambda_1$ becomes less, or t is reduced, the restriction on $\delta\upsilon$ is relaxed. For the case of the lines of singly ionized oxygen at $\lambda3729$ and $\lambda3727$, at $t = 500\mu$, $N = 30$, $\delta\upsilon \simeq 3{,}476$ km/sec.

For the most severe cases it may be necessary to obtain absolute relative velocity data using a grating spectrograph.

It is not necessary to correct the data for the variation in the wavelength calibration which occurs due to working in different orders. This is because we wish to perform the ratio in velocity space not wavelength space. Thus if the interferometer is stepped in gap t by an increment dt we find:-

$$\frac{d\lambda}{dt} = \frac{2\mu}{n} = \frac{\lambda}{t} \qquad \therefore d\lambda = \frac{\lambda}{t}\,dt \qquad (5.6)$$

but $d\lambda = \frac{\lambda d\upsilon}{c}$

$$\therefore \frac{\lambda d\upsilon}{c} = \frac{\lambda}{t}\,dt \qquad (5.7)$$

hence $\frac{d\upsilon}{dt} = \frac{c}{t} = \text{constant}$ (5.8)

So the velocity increment is independent of wavelength.

### 5.2.1.4 Background Assessment and Removal

In order that the background may be assessed and removed measurements of it are made at various points around the object. It is possible to remove either a uniform level or a varying background from the data. After subtraction the data outside the boundary of the nebula consists of a lot of small numbers corresponding to the noise on the background.

### 5.2.1.5 Background Noise

If the data is now ratioed the residual noise around the edge of the nebula will lead to large random fluctuations in the new array. This may be avoided by setting the ratio to zero wherever the signal in either array falls below a certain number of standard deviations of the background level. Thus a sharp boundary is formed around the edge of the nebula, outside which the data drops to zero. This can lead to anomalous edge effects, particularly if the spatial relationship of the maps is incorrect, or slightly in error.

### 5.2.1.6 Calibration of $N_e$ and $T_e$

The calibration of the resulting map in terms of absolute $N_e$ and $T_e$ may be performed in two ways:

A knowledge of the filter and FP transmission, extinction, photocathode sensitivity and exposure times would allow a direct computation of the absolute values. Alternatively results obtained from other observations of certain areas might be used to calculate the value at one point and then extrapolated to find the values over the rest of the object.

### 5.2.1.7 Summary

It appears perfectly feasible then to extend the present technique of two-dimensional mapping to three dimensions using the Doppler shifted line profile to map out variations in emission along the line of sight. Clearly many calibration problems exist, not least among them those of determining the absolute value of $N_e$ or $T_e$. Initially it is proposed to conduct preliminary tests into the viability of the method using the spectracon electronographic camera, in spite of its unsuitability, largely because it is at present the most accessible. A more attractive alternative is the multi-anode channel plate photomultiplier tube, which has much fewer pixells, but the advantage that there is no micro-densitometry or registration of the detector necessary. The advantages and disadvantages of the various detectors available are discussed later in this chapter.

## 5.3 The Fabry Perot as a Tunable Filter

The use of a Fabry Perot Interferometer as a variable gap, narrow band, interference filter was first proposed by Heavens, Ring and Smith (1957) and Smith and Heavens (1957). Courtes (1958) has obtained photographs through a filter of this nature, and mapped a component of velocity in a nebula of 20" diameter, whilst Reay, Ring and Scaddan (1974) have described an air spaced, optically contacted, piezo scanned F.P. working at low order as a tunable filter of 10Å bandpass for use in the photometry of red-shifted galaxies.

Essentially the variation in transmitted intensity is given by the Airy function:

$$I = \frac{I_o}{1+{}^{4N^2}/_{\Pi^2}\ \sin^2\left(\frac{2\Pi\mu t}{\lambda}\cos\theta\right)}$$

Fig 5.1 shows the variation of ${}^{I}/_{I_o}$ with off axis angle $\theta$ at constant $\lambda$ for various values of n, assuming N = 30.

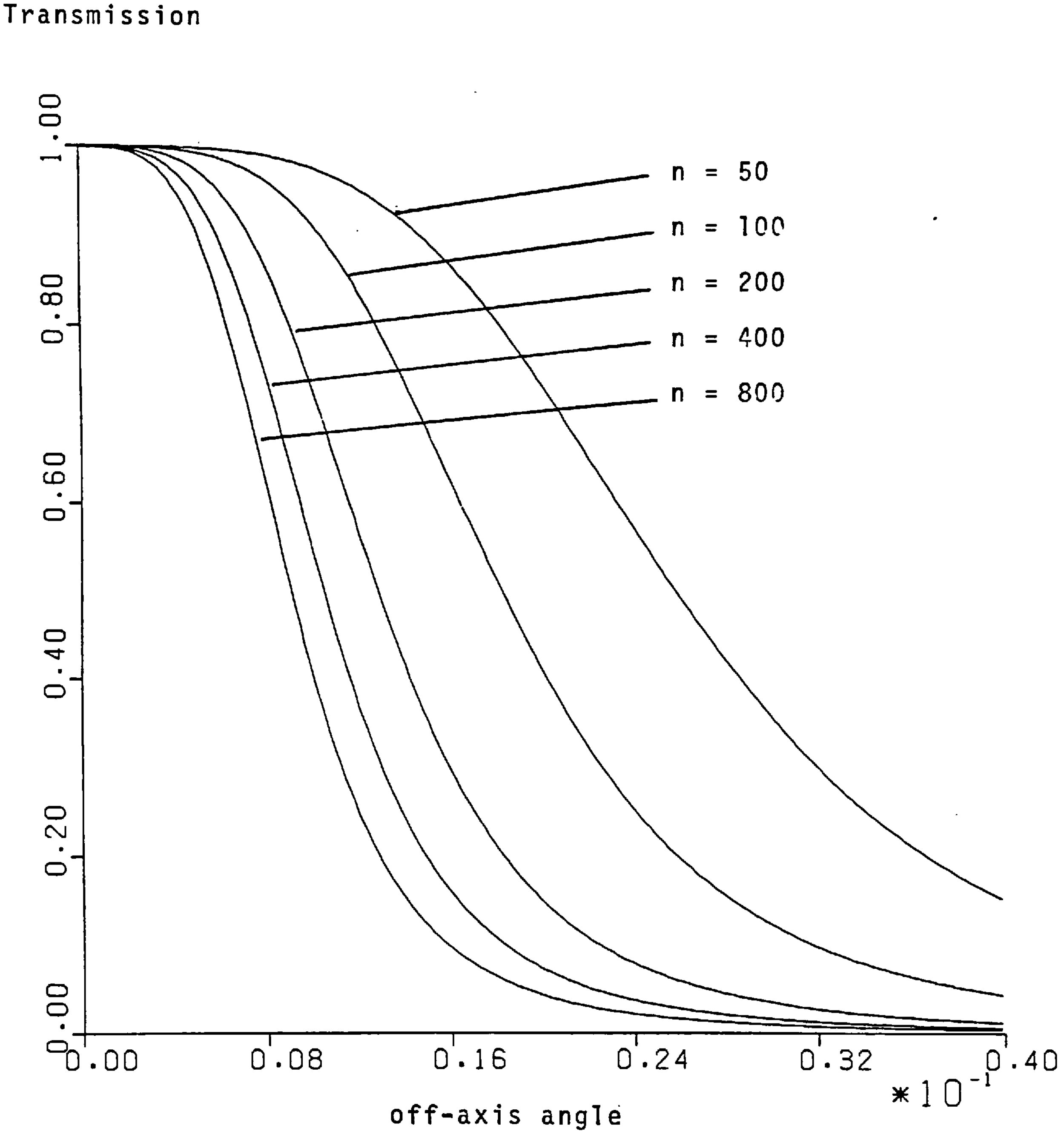

Figure 5.1. Variation in transmission as a function of off-axis angle (finesse 35)

A plot of the percentage intensity variations from centre to the edge of the field is given as a function of X, where X is the ratio of the off-axis angle to the Jacquinot criterion angle. (Fig 5.2).

Clearly even well within the Jacquinot criterion there are large fluctuations in intensity across the field, so large than under no circumstances could it be called flat.

For different points in the field the value of t at which maximum transmission of monochromatic light occurs is dependent on the off axis angle described by equation 2.15. This introduces a phase-shift in wavelength space, between profiles obtained at different points on the ring pattern. We may calculate this phase shift in the following way. At constant gap the angular separation of the first fringe from the central order is given by:

$$\Delta\theta = \cos^{-1}\left(\frac{n-1}{n}\right) \qquad (5.9)$$

Where n is the central order.

$\Delta\theta$ is the off-axis angular separation

The change in gap required to increase the order by 1 is given by

$$\Delta t = \frac{t_o}{n+1} \qquad (5.10)$$

Where $t_o$ is the original gap

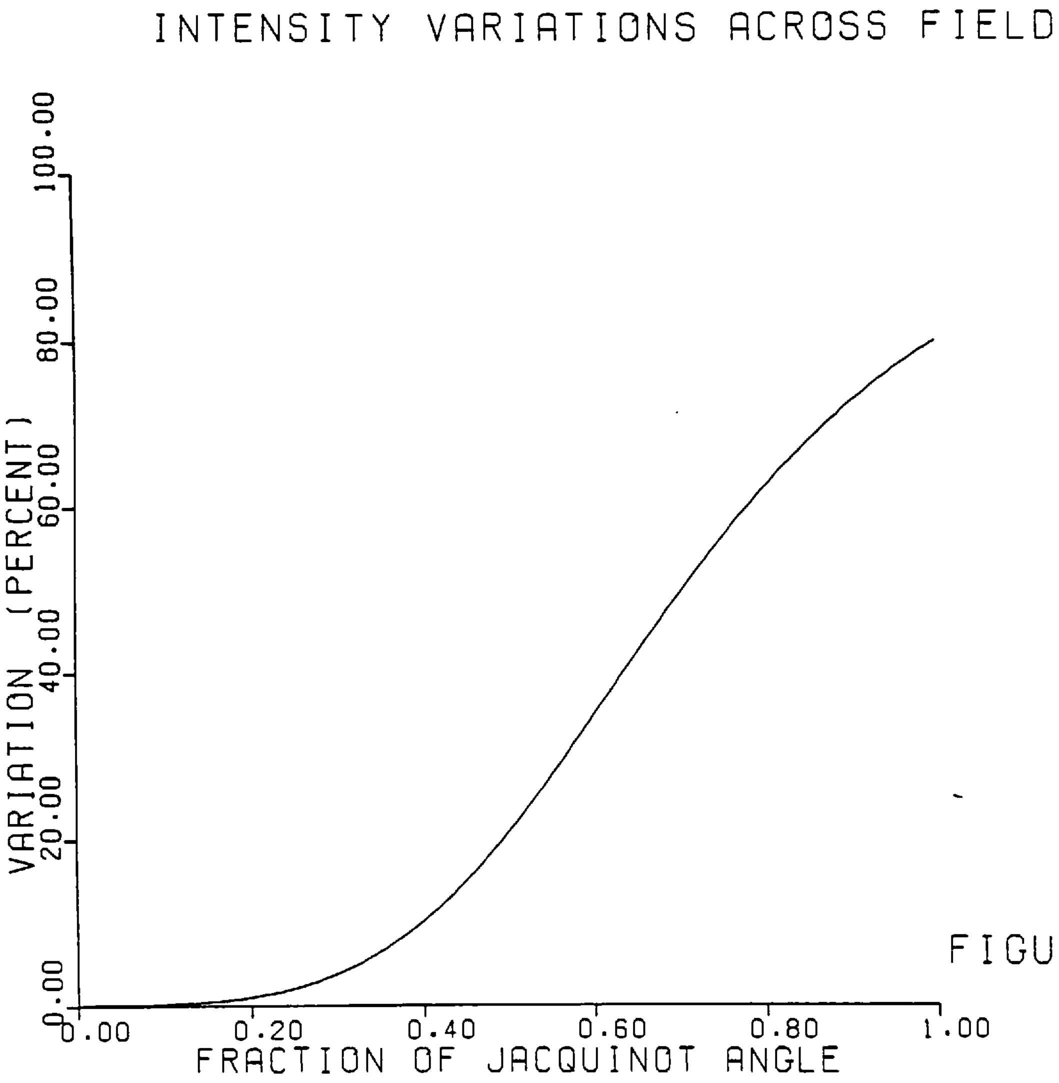
INTENSITY VARIATIONS ACROSS FIELD
VARIATION (PERCENT)
0.00
20.00
40.00
60.00
80.00
100.00
0.00
0.20
0.40
0.60
0.80
1.00
FRACTION OF JACQUINOT ANGLE

FIGURE 5.2

At an off-axis angle θ the value of t at which a maximum will occur, assuming maximum transmission on-axis at gap $t_o$, is given by:

$$t = \frac{t_o}{\cos\theta} \qquad (5.11)$$

Thus $$\frac{t-t_o}{\Delta t} = \frac{t_o}{\Delta t}\left(\frac{1}{\cos\theta} - 1\right) \simeq n\left(\frac{1}{\cos\theta} - 1\right) \qquad (5.12)$$

Figure 5.3 shows $(t-t_o)/\Delta t$ plotted as a function of θ, where θ is the fraction of Δθ.

In practice it should prove possible to determine and, if necessary, correct this phase shift of the profile observed from different parts of the field, by performing a calibration scan.

It is not usually possible to perform a calibration with a line of exactly the same wavelength as the one under observation. For a pixell at an angle θ the phase shift $P_1$ as a fraction of the inter-order spacing, at a wavelength $\lambda_1$, corresponding to an order $n_1$, is related to the phase shift $P_2$ at a wavelength $\lambda_2$ and order $n_2$ by:

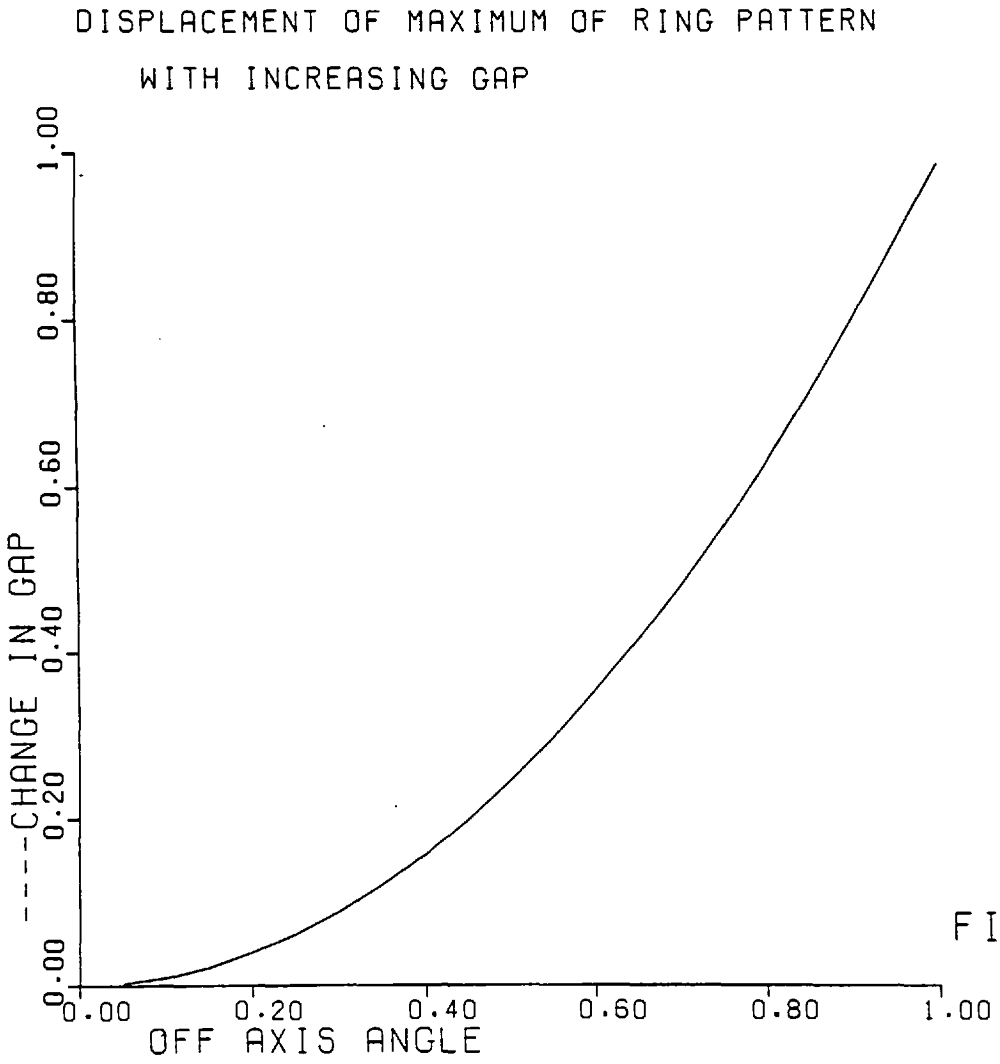
DISPLACEMENT OF MAXIMUM OF RING PATTERN
WITH INCREASING GAP
----CHANGE IN GAP
0.00
0.20
0.40
0.60
0.80
1.00
0.00
0.20
0.40
0.60
0.80
1.00
OFF AXIS ANGLE

FIGURE 5.3

$$P_2 = P_1\frac{n_2}{n_1} = P_1\frac{\lambda_1}{\lambda_2} \qquad (5.13)$$

In practice it is unlikely that the difference between the two wavelengths will correspond to an integral number of orders. This can be arranged by selecting the peak of the scan, or some other easily identifiable feature, to be transmitted at a specified F.P. position by introducing an appropriate capacitance offset.

The problems of calibration and data processing are dealt with further in section 5.4.8.

## 5.4 Multi element Detector arrays

The proliferation of two dimensional arrays of detector elements of various types and the rapid progress currently being made in the field precludes any worthwhile attempt to assess which is the 'best'. Many of these detectors utilize highly developed semi conductor technology and require sophisticated control and acquisition systems. The degree of sophistication is, obviously, dependent upon the number of pixells.

The operational characteristics of these devices range enormously. The following section is devoted to a consideration of the salient characteristics of the various detectors readily available, with reference to their suitability to operate in conjunction with an F.P.

### 5.4.1 General Considerations: Optical and Mechanical Constraints

When matching a particular detector to a Fabry Perot interferometer there are several considerations to be made: the mechanical and the optical coupling of the device to the interferometer: the storage medium, ie film, disc, magnetic tape etc, and hence the amount of interaction with the data and the necessary data processing required. We shall deal with these in turn.

1) The optical constraints are imposed by the requirement that the resolution element of the detector should be matched to both the seeing disc of the telescope and the instrumental halfwidth of the F.P. due to the dispersion across the field.

The first constraint demands at least two pixells per seeing disc for optimum sampling. The second constraint is less rigid: Only if the detector element subtends an angle comparable with half the full angular halfwidth of the largest diameter ring will there be any significant degradation in spectral resolution. The variation in the angular width of the instrumental profile may be found by differentiation of equation 2.2 $\omega$.r.t.$\theta$

$$\frac{d\lambda}{d\theta} = -\lambda_o \sin\theta \tag{5.14}$$

Thus if the pixell is matched to be less than the halfwidth of the outermost ring, then there will be little change in the spectral resolution.

The only mechanical constraint is one which limits the physical size of each pixell to be large enough to be within the optical quality of the lenses, and small enough that no substantial magnification of the image is required. A practical limit to the latter would be a factor of about 5 and to the former a minimum size of about 10μ.

### 5.4.2 Data Acquisition

Clearly systems which give direct 'real-time' digital read out of the acquired data have an advantage in that any phase corrections required to the wavelength transmitted across the field can be applied immediately, enabling the data to be displayed and its quality assessed as it arrives. Data handling and storage problems may occur however when large numbers of pixells are used.

The contour maps shown in the last chapter are drawn from a grid of 60 x 60 elements. Thus to obtain maps of comparable resolution with $\sim$ 100 spectral elements per pixell implies a storage capacity of $\sim 3.6.10^5$ locations. Approximately five or six scans of this size could be accommodated on a normal disk cartridge of the type used in mini computers, and one or two scans on a 'floppy' disk cartridge.

### 5.4.3 Photosil Detector

This device, built by Dr J.V. Jelley of Harwell in conjunction with Electon Vision Company, San Diego, USA, is essentially a modification of the Digicon (Beaver and McIwain, 1971).

Photo electrons emitted from a photo cathode are accelerated to 13-15 kV and electrostatically focussed onto an array of back biassed silicon photodiodes.

The pulse height distribution shows that the photon peak is very well separated from the noise, which allows good discrimination against the noise - typically 0.01 thermal dark counts per diode per second.

The gain is a linear function of the accelerating potential, after a threshold voltage, imposed by surface barrier losses, is overcome.

Giant pulses are produced by ions liberated from the surface of the diodes and being accelerated into the photocathode, generating large numbers of high energy electrons. These have such a slow leading edge that they only set one discriminator level and are counted as photons. This problem was overcome by means of a giant pulse rejection unit, which delays each pulse for a certain length of time before checking to see if both discriminator levels have been set. This detector has a large dynamic range due to the short response and decay times of the silicon diodes.

The Quadrant Photosil Detector, or QPD, was developed for use as an autoguider and has four pixells, each 300μ square, with a 10μ gap between them.

The fabrication of detectors with up to 36 pixells arranged in the form of a square has been discussed and is, in theory, possible. However the contacts to the diodes are made to the front surface and begin to occupy a significant fraction of the sensitive area. Furthermore, the shape of the pixells becomes distorted due to these contacts.

A QPD was lent to us by Dr Jelley for testing. Comparisons of this device with an EMI 6256S Photomultiplier tube showed abnormally low counting rates. Subsequent tests on the quantum efficiency by Mr R W Airey gave a very low value. This was interpreted as being due to the poisoning of the photocathode by these ions. Work is now in progress to eliminate these effects.

### 5.4.4 Multiple-Anode Channel Plate Photomultiplier Tube

By using micro-channel array plates as the electron multiplier in a photomultiplier tube, it is possible to preserve the image information, presented to the photocathode, through to a multiple anode array placed immediately behind the channel plate. This arrangement is known as 'proximity' focussing.

Arrays of 10 x 10 anodes in a format 12mm square giving pixells of 1.2mm square have been fabricated and used by Timothy (1976). Gains in excess of $10^6$ have been achieved. The output pulses are typically between $2.10^5$ and $4.10^7$ electrons and are 2 nano secs wide which corresponds to currents between 16μA and 320μA. These are readily detectable using low-noise amplifiers.

The dynamic range of this device is limited by the inability of the micro-channel plate to restore the electrons to its walls, in order that cascade may take place. This is due to its very high resistance ($\sim 10^9 \Omega$). For the device described above it is currently possible to maintain a linear response up to about $10^4$ counts per sec per piscell. After this the gain of the channel plate falls below the discriminator threshold which is set by the need to reject crosstalk between adjacent pixells.

The dark counts for this device are very small for two main reasons:

1) As each pixell is only looking at a very small part of the photocathode the thermal noise is small.

2) The phenomenon of ion feedback, due to collisional ionization of neutral gas molecules inside the microchannels by the passage of a cascade, has been virtually eliminated by curving the microchannels. Dark counts from the channel plate have been measured, as equivalent to $3.10^{-2}$ counts $\sec^{-1}$ $\text{pixell}^{-1}$ for the device described at an operating voltage of 2.3kV.

This device has a number of distinct advantages:

a) It is an extremely compact device, being smaller than a cube of side 3 cms.

b) It has a relatively low operating voltage - around 2.5 kV.

c) It has a high quantum efficiency (∿15%) very low dark count (∿ 1 count $sec^{-1}$ $pixell^{-1}$)

d) No cooling of the device is required.

Its practical limitations lie in the maximum number of pixells that may be used and its dynamic range. Current technology is capable of forming around 500 discrete anodes in a tube of this type, the major difficulty being the number of connections required to the base. Methods of extracting positional information using overlaid wire grids, which show the electron cloud presented between several lines, enabling its position to be determined by ratioing techniques, are now being developed (Audier and Boutot, 1975, Timothy and Bybae, 1975). Another technique being studied is the resistive anode. This is a continuous resistive anode placed in proximity focus to the channel plate multiplier. The 'transit' time of the electron cloud from its position of incidence on the anode to each edge enables its position to be determined. (Lampton and Paresca 1974).

The price paid by these techniques is a reduction in the maximum system count rate due to the coincidence - resolving time of the electronics.

### 5.4.5 Two dimensional Image Photon Counting System

This device, developed by Dr A Boksenberg and his associates, consists of well developed, commercially available image intensifier and TV camera tube components.

Essentially a 4 stage cascade image intensifier with an S-20 photocathode and a gain of $10^7$ is coupled by a relay lens to a Plumbicon TV camera. The image intensifier amplifies each photon above the noise level of the Plumbicon camera. The device is essentially photon counting and has potentially 540 x 1024 piscells. However the lack of sufficient external memory has prevented the use of more than 64 x 1024 pixells to date.

The long decay time of the phosphor screens coupling the image intensifiers (½msec for decay to 10% of original signal for P11 phosphors) limits the dynamic range of the system to about 100 counts $sec^{-1}$ $pixell^{-1}$ for a statistical coincidence of 10%.

A feature of the system is a pattern processor which identifies the central position of each event and enables events to be recorded with equal weight, without system noise and with a large increase in spatial resolution. The use of a high and low brightness discrimination threshold enables bright noise scintillations and amplifier noise to be rejected making the system essentially photon counting.

### 5.4.6 Silicon Target Type Detectors

A silicon target is composed of a single crystal silicon disc on one side of which is formed a large number of small electrical diodes of about 10μ diameter. These targets are generally operated in two distinct modes making use of their sensitivity to both photons and electrons.

#### 5.4.6.1 The Silicon Target (S-T) Tube

If the silicon target is used directly in the focal plane of an optical system it will be sensitive to photons from below 3700Å to above 12,000Å. Each photon absorbed by the target produces one electron-hole pair, and discharges the nearest diode by one electron charge. In the readout process an electron beam recharges the disc diodes, drawing current through the target biassing circuit which is proportional to the incident signal level. Each diode will store about $10^5$ charges. The quantum efficiency of this device, operated in this mode, varies from about 80% at 5000Å to about 10% at 1μ.

However, various properties of the readout process and the preamplifier produce a 'readout noise' equal to about 600 photons (McCord and Westphal, 1972). This prevents photon counting and puts a fundamental limit on the use of the S-T to sources sufficiently bright that signals significantly greater than this can be obtained.

### 5.4.6.2 Intensified Silicon Target Tubes

The basic limitation imposed by readout noise can be overcome by amplifying the signal using an intensifier stage. This is at the expense of the dynamic range of the device.

The sensitivity of the silicon target to electrons means that an electrostatically or magnetically focussed photo-electron accelerator can be used to accelerate electrons emitted from a photo cathode into the target. Each photo electron can be made to generate about 2000 carriers and it thus becomes possible to record two dimensional images which are photon-noise limited. However the limited storage capacity of each diode severely restricts the dynamic range of the device as saturation is reached at 50 photons per diode.

Alternatively the initial gain may be supplied by an image intensifier stage fibre-optically coupled to a silicon target tube or an intensified silicon target tube.

### 5.4.7 The Electronographic Camera: The Spectracon

This device has been discussed in detail elsewhere (McGee et al 1972) and it is not necessary to repeat it here. For the purposes of this discussion however it is convenient to recall some of the salient features.

Essentially the Spectracon is a magnetically focussed electronic camera. Photons incident upon a photocathode liberate photo-electrons which are then accelerated by a potential difference of 40 kV into a nuclear emulsion situated behind a mica window of about 4 microns thickness. The distinguishing feature of the Spectracon - and more recently the McMullan tube (McMullan, 1972) - is this window, which enables the emulsion to be out in the air, where it can easily be changed, without resorting to the high vacuum technique necessary with devices such as the Lallemand camera (Lallemand, 1966).

The physical size of the recording area is limited by the size of the mica window which will withstand the pressure difference, whilst allowing good contact between the emulsion and the mica and being sufficiently thin that the photo electrons accelerated by the tube are able to pass through. For the Spectracon this size is about 10mm x 30 mm.

The primary advantages of the Spectracon over the photographic plate for small areas, are its linear relationship between exposure time and density and its higher sensitivity. Typically the overall D.Q.E. of the device is around 3%. Its dynamic range is almost 1000:1 and the limiting photometric accuracy around 2%.

After an exposure the emulsion is digitized, using a micro densitometer, and the resulting information is written onto magnetic tape. This is then processed using a computer and contours of equal density, representing equal photon fluxes are drawn.

Although the reduction of data obtained with the Spectracon is more involved than that from a device with digital output, the information storage capacity is very large. Furthermore the data reduction programs are already in existence and techniques for producing ratio maps and hence temperature and density contours are well developed.

For this reason preliminary experiments with its use as a two-dimensional detector coupled to a Fabry Perot Interferometer are now in progress.

### 5.4.8 Data Processing

For the purpose of this discussion, assume a detector with X by Y pixells. If a frame of data is taken at Z different F.P. positions then the resulting three dimensional array of numbers represents the spatial (X,Y) and spectral (Z) variations in emitted flux.

If the number of pixells (X,Y) is such that each frame cannot be considered as a true image then it is probably best to interpret the data using line profiles. Any one particular pixell, at a coordinate x, y, may be scanned through the various z values, corresponding to changing gap in the interferometer, and a line profile created which is identical to that which would have been obtained had a single-point detector been used. The necessary phase corrections may be applied to each profile and the variation in the shape of this profile interpreted in the manner described in Chapters 3 and 4.

When X.Y exceeds about 100 then the interpretation of the data using line profiles becomes unwieldy and inadequate.

If the velocity structure of the object is already well determined then it should be possible to relate a specific coordinate in the data array to a particular region of the nebula. Thus the data array can be transformed from velocity space to 'real' space. Any ratioing of data arrays obtained on different emission lines that is necessary to obtain density or temperature information (section 5.2.1) is more easily performed before the transformation, as only one such transformation is then required. If the velocity structure of the object is unknown then, by correcting the wavelength or 'phase' shift induced by the dispersion, frames of equal wavelength and hence equal velocity may be created. As a diagnostic line profiles may be reconstructed for various parts of the field. The change in the image structure with velocity should provide vital clues to the manner in which the object is expanding.

The necessity to 'phase-shift' the Z value by varying amounts across the image to correct the dispersion and construct 'monochromatic' frames of data has important implications for the way in which the data is acquired. This is discussed in the next section.

### 5.4.9 Calibration

#### 5.4.9.1 Phase Shifting

The way in which the phase shift, due to the off axis position in the field introduced by the dispersion, is removed was indicated in section 5.3. However this process is not so simple as it might first appear.

Consider a point at an angle $\theta$ off-axis. It's phase shift is given by Eqn. 5.14:

$$\Delta\lambda = -\lambda_0 \sin\theta . \Delta\theta$$

for small $\theta$ this reduces to:

$$\Delta\lambda = -\lambda_0 \{\frac{\Delta\theta}{2}\}^2 \qquad (5.15)$$

Let us assume that data points have been taken every t step corresponding to an increase in $\lambda$ of $\lambda_{INC}$.

Obviously there is no reason why $\Delta\lambda$ should equal $\lambda_{INC}$ or any multiple of it. So, in order that we can create frames of entirely monochromatic information we must interpolate between the two points straddling the value of $\lambda$ at which we wish to calculate the intensity.

There are various techniques for performing this interpolation:

We may perform a straight line interpolation such that if we have a value x counts at $\lambda_o$ and a value y counts at $\lambda_o + \Delta\lambda$ then the counts C at $\lambda_o + \lambda_{INC}$ will be given by:

$$C = x + \frac{y - x}{\Delta\lambda} \cdot \lambda_{INC} \qquad (5.16)$$

Alternatively, we may perform a polynomial fit to the whole curve, or merely the adjacent N pts, to any required accuracy and then calculate the required value from the resulting equation.

Both these methods have their advantages and disadvantages. Clearly for a large number of pixells it is impractical, although by no means impossible, to fit a polynomial to the data from each pixell. The method of straight line interpolation however requires a smaller sampling interval if the errors introduced by the interpolation are to become smaller than the photon shot noise.

The number of sample points per halfwidth required for a certain maximum interpolation error is plotted in Figure 5.4 for the case where structure exists which is narrower than the instrumental profile, ie scanning a laser line. Clearly,

INTERPOLATION ERROR VS. NO. OF POINTS PER HALFWIDTH

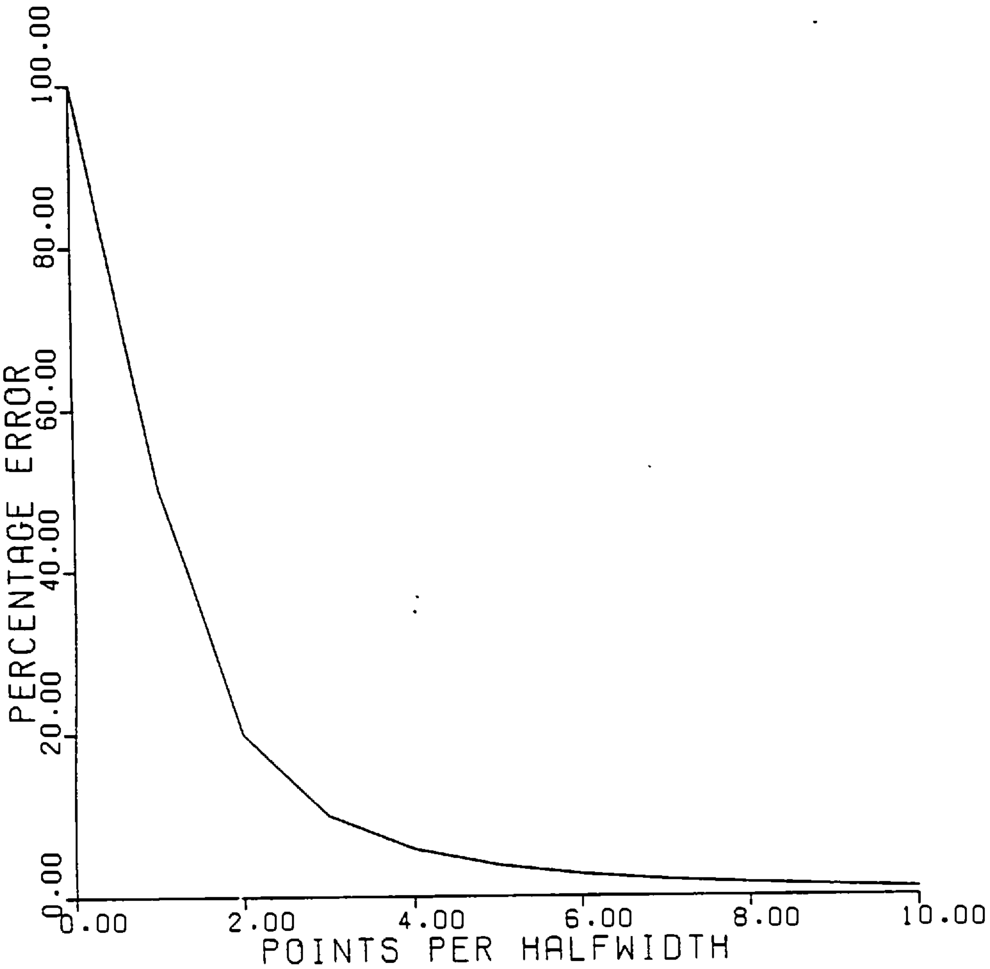

FIG. 5.4

in order that accurate photometric images can be obtained in this manner, a relatively large number of sample points are required, leading quickly to data handling problems. For 5% photometric accuracy and an effective finesse of 30, approximately 135 frames of data are required to scan a complete order.

### 5.4.9.2 Calibration of Phase Shift

In order to determine the relative phase shift introduced by the dispersion across the field it is necessary to scan a monochromatic light source, a He Ne laser for instance, and determine at which step number the F.P. transmits a maximum as a function of the position of the relevant pixell. For this purpose sufficient accuracy is required to ensure that interpolation errors dominate, and thus the number of samples per halfwidth needed is equivalent or greater than dictated by the accuracy of interpolation required.

Once the phase shift for each pixell has been determined, the values may be set up in a two dimensional 'calibration' array.

### 5.4.9.3 Spectral Response

Any fluctuations in spectral response of the premonochromating filter may be assessed by scanning a white light source. It is essential however that the band pass of the filter be less than the free spectral range of the F.P.I., otherwise a unique interpretation of the results is not possible, transmission through the filter occurring in different orders.

These fluctuations, if fairly small, may be removed by dividing the data by this calibration scan. However, this process changes the noise statistics on the data, artificially enhancing some parts of the data with respect to others, whilst not changing the signal to noise. Thus the noise is no longer Poissonian.

# CHAPTER 6: FURTHER DEVELOPMENTS

## 6.1 Introduction

In this chapter, the most recent developments in the instrumentation are described, together with proposals for extending the operational capability of the instrument.

The recent developments include the construction of a mechanically rigid etalon assembly for use at the focus, the design and construction of an imaging F.P. and extensions to the operating range of the error detection system, and the error correction system.

## 6.2 Etalon Assembly

The susceptibility to vibration and the large mechanical relaxations encountered with the etalon described in Chapter 2, limited its performance. The complications arising from the necessity to mount the etalon on vibration isolators are probably not tolerable with an imaging system. The maximum observing time attainable without attention to the F.P. was approximately three hours, after which the movement of the telescope due to tracking ($\lesssim 45^{\circ}$) induced mechanical relaxation equal to the full range of the piezo electric transducers, about 4$\mu$, at which point the system saturates and a realignment is necessary. In practice a mechanical offset was introduced, using the parallelism adjustment, at intervals of about an hour, with the servo loop closed, taking out the relaxation and thus minimising the voltage on the transducers. In this manner it is possible to continue almost indefinitely without need for realignment. Problems are caused however when setting on objects, as this requires gross changes in the attitude of the telescope and it was found necessary to align the F.P. and close the loop each time a different object was set upon.

Clearly the system as it stood was workable, but required more attention than was desirable for efficient operation and remote control.

The problems discussed are drastically reduced using the assembly shown in Figure 6.1. The design was intended to reduce or eliminate all the identifiable sources of flexure, creep and relaxation in the etalon mount.

The major difficulty in designing a rigid etalon assembly is the necessity to include piezo electric transducers and also adjustments to the parallelism of the F.P. in a rigid mechanical loop between the two faces of the F.P. plates.

Essentially, the etalon is built on a 10" square by 1" thick Dural base plate. This base plate is kinematically mounted onto a 12" diameter ring by means of 3 ball ended screws mounted in V-grooves. This ring is then used to mount the assembly to prevent any flexures in the rig being transmitted to the etalon. This configuration allows adjustment of the whole assembly perpendicular to the optical path, even whilst the servo loop is closed.

Each F.P. plate is mounted in a cell, also shown in Figure 6.1. The nylon screws used in the old mount have been replaced by a leaf spring arrangement. These are pretensioned such that the force applied to the underside of the mounting lug, through the PTFE pad (to spread the load evenly)pressing it onto the ball bearing, is sufficient to

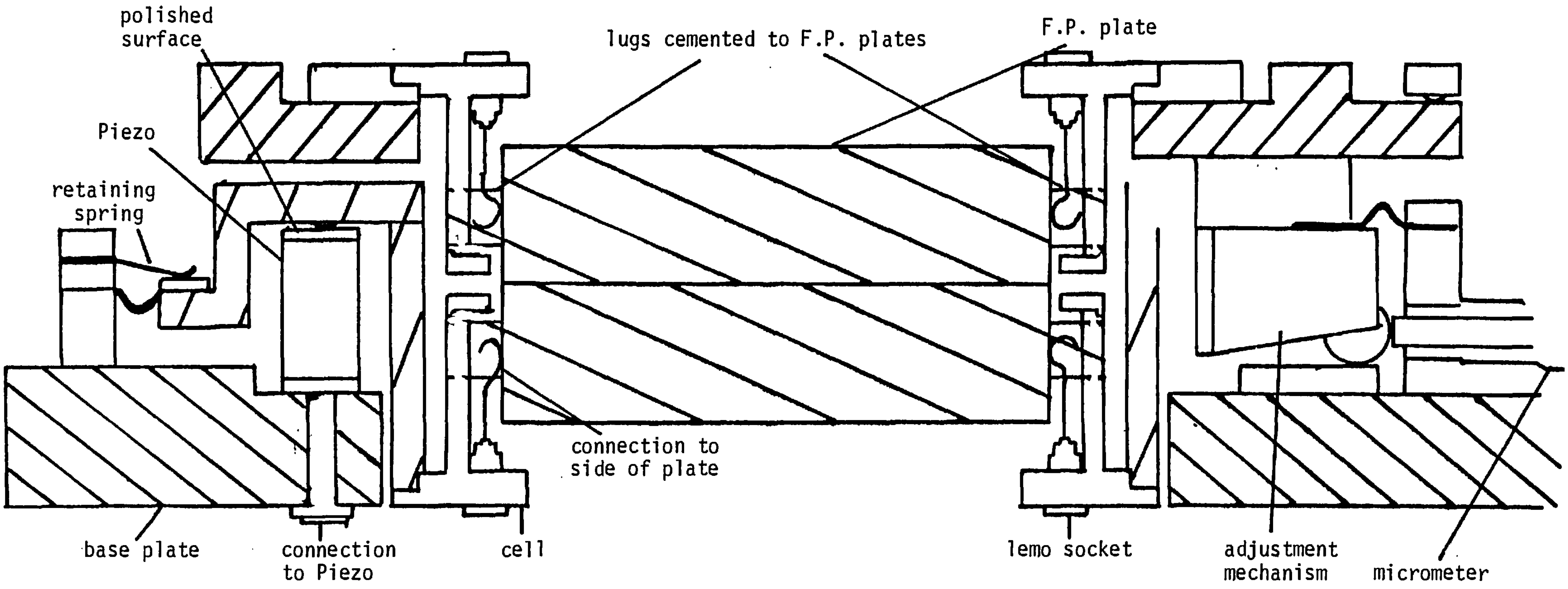

Figure 6.1 Etalon Assembly

locate the plate firmly, without inducing unnecessary strains, which might introduce bowing. The signals from the capacitor pads are routed through gold coated contacts to a screened socket located on the underside of the cell. Each cell is screwed to a carriage on the etalon assembly. The are two carriages: one providing adjustment in $\theta, \phi$ and z and another heavily sprung onto the piezo electric transducers.

### 6.2.1 Adjustment Carriage

The adjustments are made by means of three separate micrometers. These function by pushing stainless steel ball bearings into a shallow wedge (Figure 6.2). The wedge is formed from 3 pyrex glass blocks, two on top forming a V groove wedged at an angle $\sim 10^{o}$ to the third plane which is parallel to the base plate. The glass blocks were optically polished to ensure a smooth surface for the steel bolt to move on. Compression springs were used to load the ball against the micrometer head ensuring that it was forced out of the wedge when the micrometer was wound out.

This action was facilitated by lubrication with a lithium based, molybdenum disulphide loaded grease, which was found necessary to eliminate drifts in the alignments which

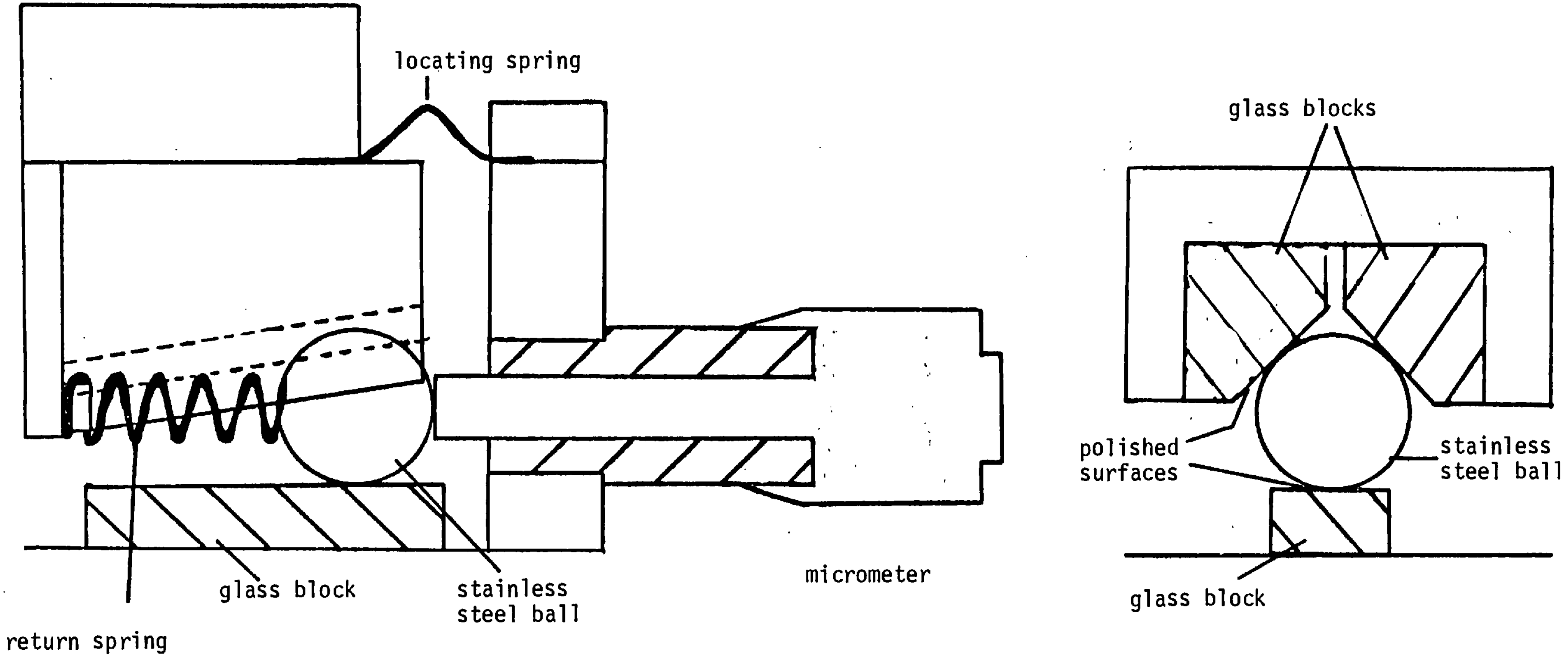

Figure 6.2 Adjustment Mechanism

immediately follow an adjustment.

This carriage was firmly spring loaded onto the balls by means of adjustable compression springs, and was anchored rotationally by 3 'swan necked' leaf springs which allowed twisting movements to take place, but not rotational ones.

The advantages of this configuration were mainly the sensitivity of adjustment possible, its rigidity and stability, and its insensitivity to lateral pressures on the micrometer head, which are insignificant, to first order. This insensitivity facilitates coupling the motor drives to the micrometers which would enable complete remote control of the instrument.

### 6.2.2 Piezo Carriage

The second carriage is heavily spring loaded onto the piezo electric transducers. The transducers are mounted off the base plate of the etalon assembly and insulated by means of a ceramic washer. A brass bush is epoxied to the interior of the cylindrical stack, allowing a 4BA screw to be used to clamp it down. This screw also forms the electrical H.T. connection to the inside of the piezo. On the top of the transducer is a polished glass disc. A ball bearing cemented into the underside of the piezo carriage rests on this glass disc. The carriage is sprung onto the three piezos, through these ball bearings, by means of three phosphor-bronze leaf springs, and is constrained rotationally by means of three swan-necked springs of the type mentioned above. In this manner no lateral forces are placed on the transducers, which are the weakest part of the assembly.

## 6.3 Imaging Interferometer Assembly

The desirability, and the advantages to be gained by using F.P.s in conjunction with multi-element array detectors were discussed in Chapter 5. In order to conduct preliminary tests of this configuration, to assess its practicability, a rig was constructed in which the etalon assembly, discussed in the previous section, was mounted, and which preserved the image quality of the telescope to better than the resolution of the detector: in this case the Spectracon electronographic camera.

To keep the length of the instrument to a minimum, and to ensure high image quality, the collimating and condensing lenses used were "off the shelf" telephoto camera lenses. Tests on these indicated reflection losses of less than 8%. The collimating lens was simply a telephoto used in reverse. A diagrammatic picture of the rig is shown in Fig 6.3. It is built from 2 15" square x 1" thick Dural plates, separated by 4 1" square x 28½" long Dural rods. A series of removable and interchangeable panels complete the box and all the interior components are mounted off these panels, allowing a variety of configurations: specifically, in certain cases the output image scale may need to be $<\frac{1}{5}$ the input scale implying a ratio of $\sim 5$.

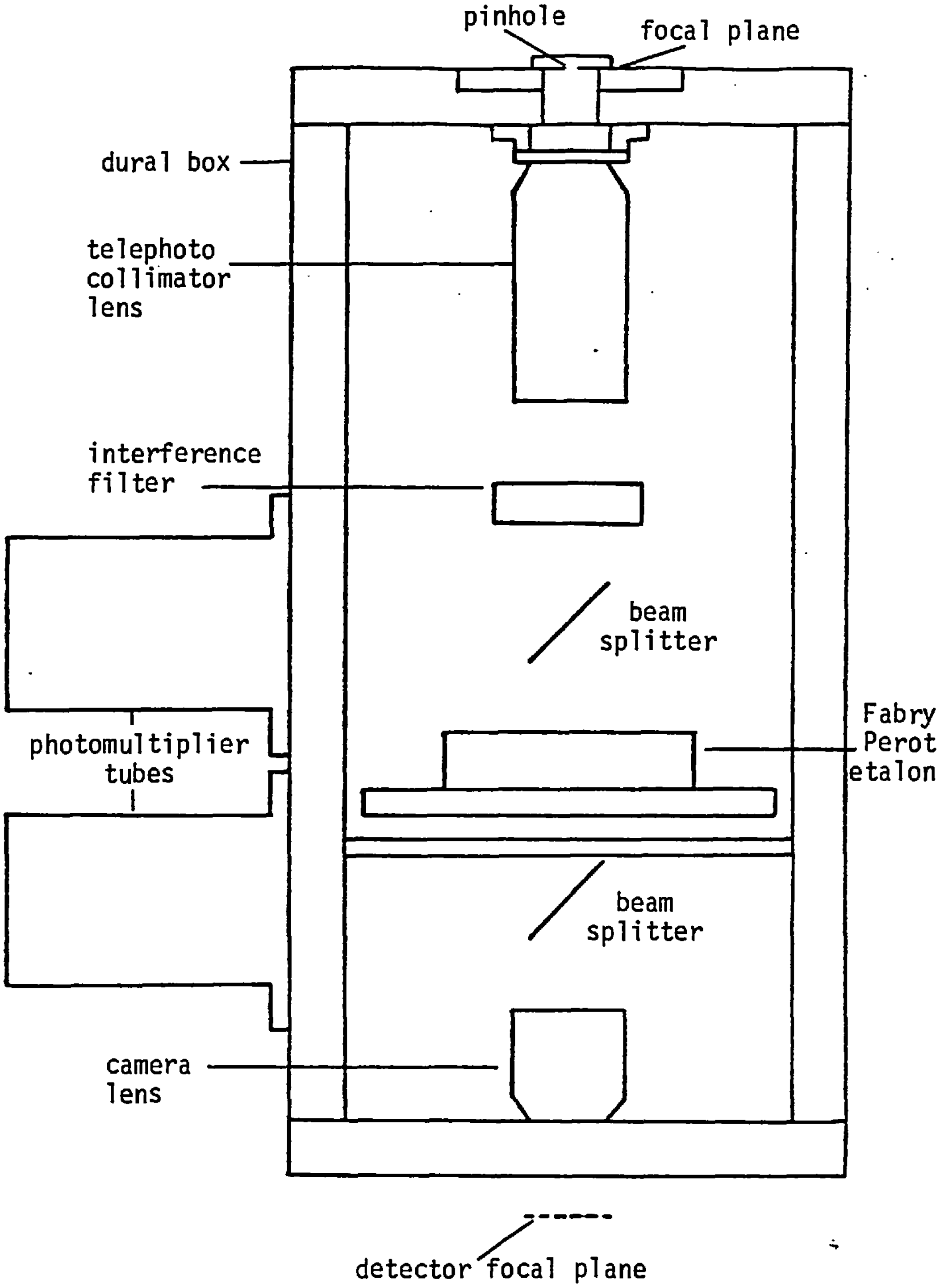

Figure 6.3 Imaging Fabry Perot Interferometer

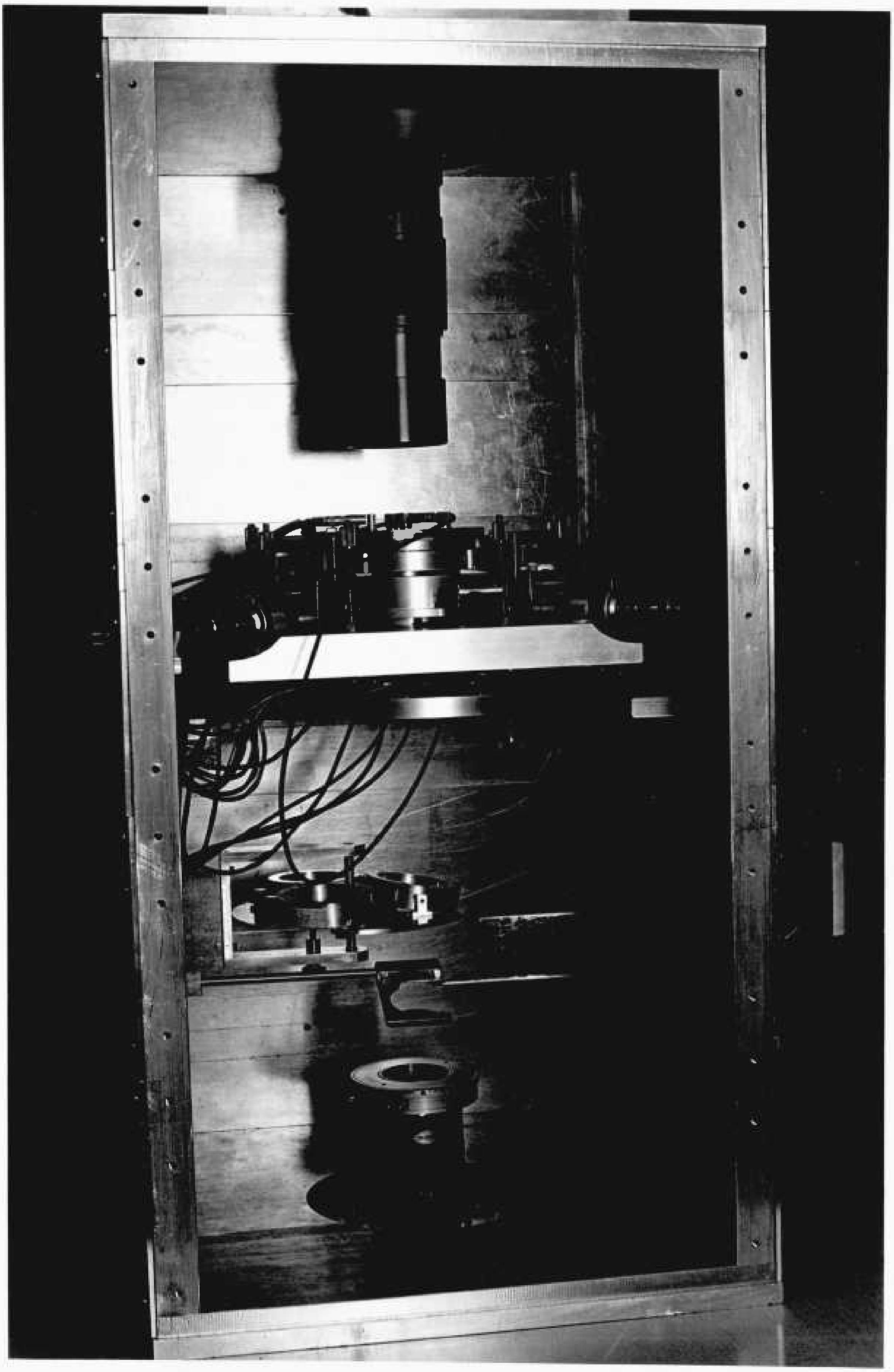

The Imaging Fabry Perot

The wide range of pixell sizes, from 10μm to 1000μm, dictates that a certain flexibility in the operational configuration be catered for.

The field stop is located in the input focal plane and consists of a wide range of pinholes of various sizes. Due to the variability and uncertainty about the positions of the principal planes of the collimators the correct field lens was chosen by experiment, using various lenses until the primary was imaged at, or close to, the etalon.

A filter wheel is mounted between the collimator and the etalon, allowing any one of 3 filters to be selected. This will eventually be replaced by a Geneva Mechanism enabling remote control of the tilt and position of the various filters.

Provision is made for two minitoring channels, one prior to the etalon and filter minitoring the constancy of the absolute flux level, and one after the etalon and filter to monitor the line profile shape and enable calibration scans to be made when using an electronographic camera which has no direct read-out of the signal.

The light is diverted by means of clip in beam-splitters or mirrors, depending on the application, and sent out at right-angles to photomultiplier tubes mounted on the outside of the rig.

Various spectral lamps are provided for alignment of the etalon, and calibration purposes. Alignment of the rig with the optical axis of the telescope, and subsequently the lenses and the F.P., is performed using a He Ne laser attached to the side of the rig and reflected off two detachable mirrors.

Guiding was performed using the offset guider box mentioned previously (2.8.4) which is attached to the front end of the rig.

## 6.4 Extensions to Capacitance Micrometry

At present the capacitance micrometer system is designed to operate at a capacitor gap of between 50µ and 100µ. Practical limitations to this range are set by the decrease in the bridge sensitivity. This is given by equations 2.38 and 2.39:

$$\frac{dc}{dt} = -\frac{KA}{t^2}$$

$$\frac{di_D}{dc} = jwV$$

Combining these:

$$\frac{di_D}{dt} = jwV. -\frac{KA}{t^2} \qquad (6.1)$$

Thus a particular change in gap dt results in a current in the detector di, which is directly proportional to the bridge drive voltage and inversely proportional to the square of the gap.

Under normal operating conditions the electrical noise in the system appears as a noise on the absolute spacing of the plates which is less than their surface flatness. However as the gap t increases the distance dt that the plates must move to servo out a particular offset $di_D$ increases. Eventually, when t is sufficiently large, the amplitude of the noise increases to the extent that it begins to degrade the finesse. It is at this point that the practical limitation to this capacitance micrometer sets in. The present arrangement permits operation up to gaps of about 200μm. There are various ways of increasing this figure and these will be discussed shortly.

It is not essential that the optical gap be the same as the capacitor gap $t_c$, although this is perhaps the most elegant configuration. By optically contacting pillars of height p around the plates, then it can be arranged that $t_o = t_c + p$. Conversely a stepped configuration may be used, so that $t_o = t_c - p$ which requires a 'composite plate'. In this manner it is possible to work at any optical gap whilst keeping $t_c$ to 50μ.

As the range of resolutions of the interferometer depends upon the range of values of the gap, it is desirable to be able to work at as large a range of values of the capacitor gap as is technically possible. The variables which determine the bridge sensitivity are given in equation 6.1.

They are V, $\omega$, A, t. At large values of t to increase $di_D/dt$ it is necessary to increase V, $\omega$ or A. $\omega$, the bridge driving frequency, has been fixed at 16 khz, which is low enough to keep the effect of stray capacitances to earth small, whilst high enough to give a reasonable bridge sensitivity and the possibility of a short time constant. V, the bridge drive voltage, is at present about 10 volts peak to peak. This may be increased to about 60 volts peak to peak for large gaps where there is no danger of shorting the capacitor pads together and putting large signals into the sensitive preamplifiers. A, the capacitor pad area, may also be increased, either by using larger plates or a larger proportion of the circumference by making them annular, rather than circular. At large gaps the size of one pad, with respect to the other, must be sufficient to ensure low sensitivity to lateral displacement of the pads. The combined effects of these measures should allow operation of the servo-system up to capacitor gaps of 500 μm and greater.

An alternative approach to increasing the flexibility of the system is to divorce the capacitor pads completely from the plates, by mounting them, for instance, on cells which hold the plates. In this case, the two cells are servoed together and the Fabry Perot plates are not, actually, in the servo-loop. The optical spacing of the plates may be varied by inserting spacers of different sizes into the cells. Careful mechanical design of the cells should ensure minimal drift between the plate and its cell. This system has the advantage that virtually any optical gap may be used with only one set of plates. Furthermore, only one set of capacitor pads are needed, mounted on the cells and smaller plates may be used. Preliminary trials of this technique are now under way (Hicks, 1978).

## 6.5 Extending the Error Correction System

Obviously the greatest range possible is required of the error correction system - in order that large mechanical offsets, induced by very large changes in temperature, or by sudden jolts, or as a result of relaxation over a long period of time, may be corrected.

The error correction system comprises the piezo electric transducers, and the high tension amplifiers which drive them.

The limiting field which may be applied to the piezoelectric material is approximately 900 $Vmm^{-1}$ for PZT-5H. (Vernitron,1978). If this field is exceeded breakdown will occur, or the material will become depolarised depending upon the alignment of the field with the axis of polarization of the material.

There are various modes in which the expansion of the piezo electric material with applied voltage may be utilized. These modes are characterized by a subscript to the parameter d describing the expansion in mm $V^{-1}$. This subscript refers to the relation between the direction of polarization, z, and the expansion of the material. For convenience, x,y,z are usually denoted by the subscripts

1,2,3 respectively. Thus $d_{33}$ denotes the expansion along the direction of polarization, whilst $d_{31}$ denotes the expansion perpendicularly. Typically for PZT-5H, $d_{33}$ = .593nm $V^{-1}$ and $d_{31}$ = -.274 $nmV^{-1}$. Presently the piezo stacks used are cylinders 25mm long, operated in the $d_{31}$ mode, up to a maximum of ± 800 volts. The wall thickness of these cylinders is ∿3mm which gives a maximum permitted field of 2,700V. The present extension is ∿ 4μm at maximum, but there is clearly room to increase this to at least 10μ, simply by increasing the E.H.T. output voltage. Further improvement can be made by using the material in the $d_{33}$ mode, which gives twice the expansion per volt. For this reason three stacks are now under construction by I.C.O.S. Ltd. The designs for these are as shown in Fig 6.4. A series of 2mm thick discs and plates are epoxied alternately together, making 11 elements in total. The polarizations of these elements are alternated as shown in the diagram, and connections made to the intersections where the square plates stand proud of the circular discs.

For mounting purposes a brass plate with a 4BA tapped hole in it is exoxied to the bottom of the stack and a polished glass disc to the top.

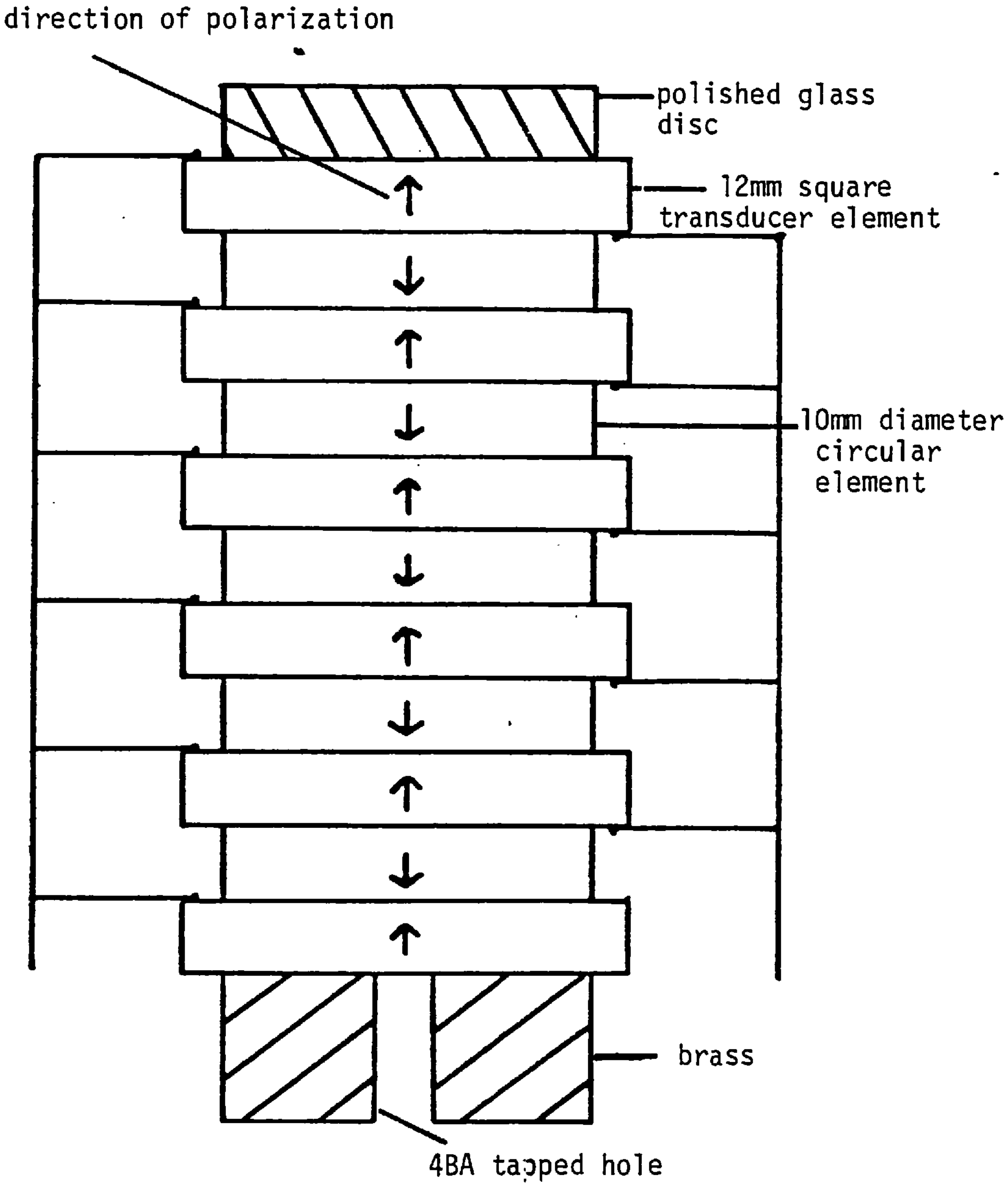

Figure 6.4 Composite Piezo Stacks

The theoretical expansion of this arrangement, at maximum field, is approximately 24 microns, giving a factor of 6 improvement on the present arrangement.

# APPENDIX: MODELLING OF THE NEBULAR ENVELOPE

## A.1 Introduction

So far, no-one has attempted to build a model of a planetary nebula to account for both the morphological and the dynamical aspects as well as the ionization structure. Several workers (Mathews, 1966; Hunter and Sofia, 1971; Pecquinot, 1977) have constructed models to explain the radiative transfer problems, but these are usually spherically symmetric, with uniform density distribution. Others have proposed models to account for the morphological aspects of the situation (Gurzadyan, 1970; Louise, 1974; Proisy, 1974; Phillips and Reay, 1977) but these, in turn, take no account of such effects as the passage of ionization fronts through the nebular material, or of the apparent differences in structure shown by different lines.

Inevitably the picture presented is incomplete. However, by using simple models there are many aspects of the situation that may immediately be clarified, such as the allowable ring to centre intensity variations for a uniform spherical shell, or the amount of dust required to produce a given suppression of part of the profile.

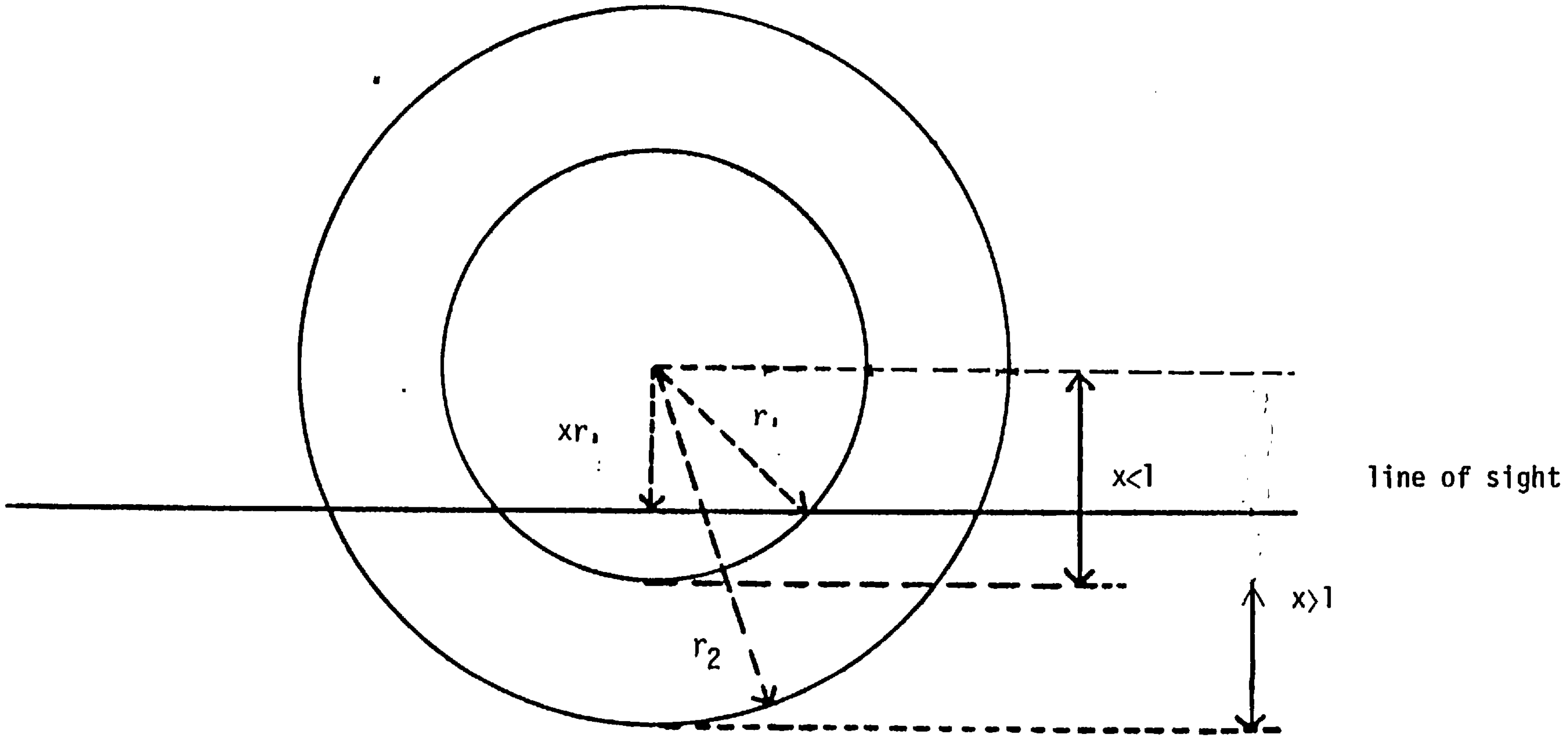

Figure A.1 Simple Shell Model

## A.2 Simple Nebular Models

The intensity variations due to line of sight effects in a spherical shell of uniform density have been calculated by Gurzadyan (1970) and later by Louise (1974). For a shell of internal radius $r_1$, external radius $r_2$ (Figure A.1) it can be shown that the emitted intensity I varies with the apparent distance from the centre of the nebula $xr_1$ in the following manner:

$$\frac{I(x)}{I(o)} = \frac{(r_2{}^2-x^2r_1{}^2)^{\frac{1}{2}} - (r_1{}^2-x^2r_1{}^2)^{\frac{1}{2}}}{r_2-r_1} \quad \text{when } x < 1 \qquad \text{(A.1)}$$

$$\frac{I(x)}{I(o)} = \frac{(r_2{}^2-x^2r_1{}^2)^{\frac{1}{2}}}{r_2-r_1} \quad \text{when } x >> 1 \qquad \text{(A.2)}$$

Clearly I(x) is maximum when x = 1, ie at the maximum line of sight distance.

Thus:

$$\frac{I(r_1)}{I(o)} = \frac{(r_2 + r_1)^{\frac{1}{2}}}{(r_2 - r_1)^{\frac{1}{2}}} = \frac{n + 1}{n - 1}^{\frac{1}{2}} \qquad \text{(A.3)}$$

where $n = r_2/r_1$

Figure A.2 shows a graph of $\frac{I\ max}{I(o)}$ against n

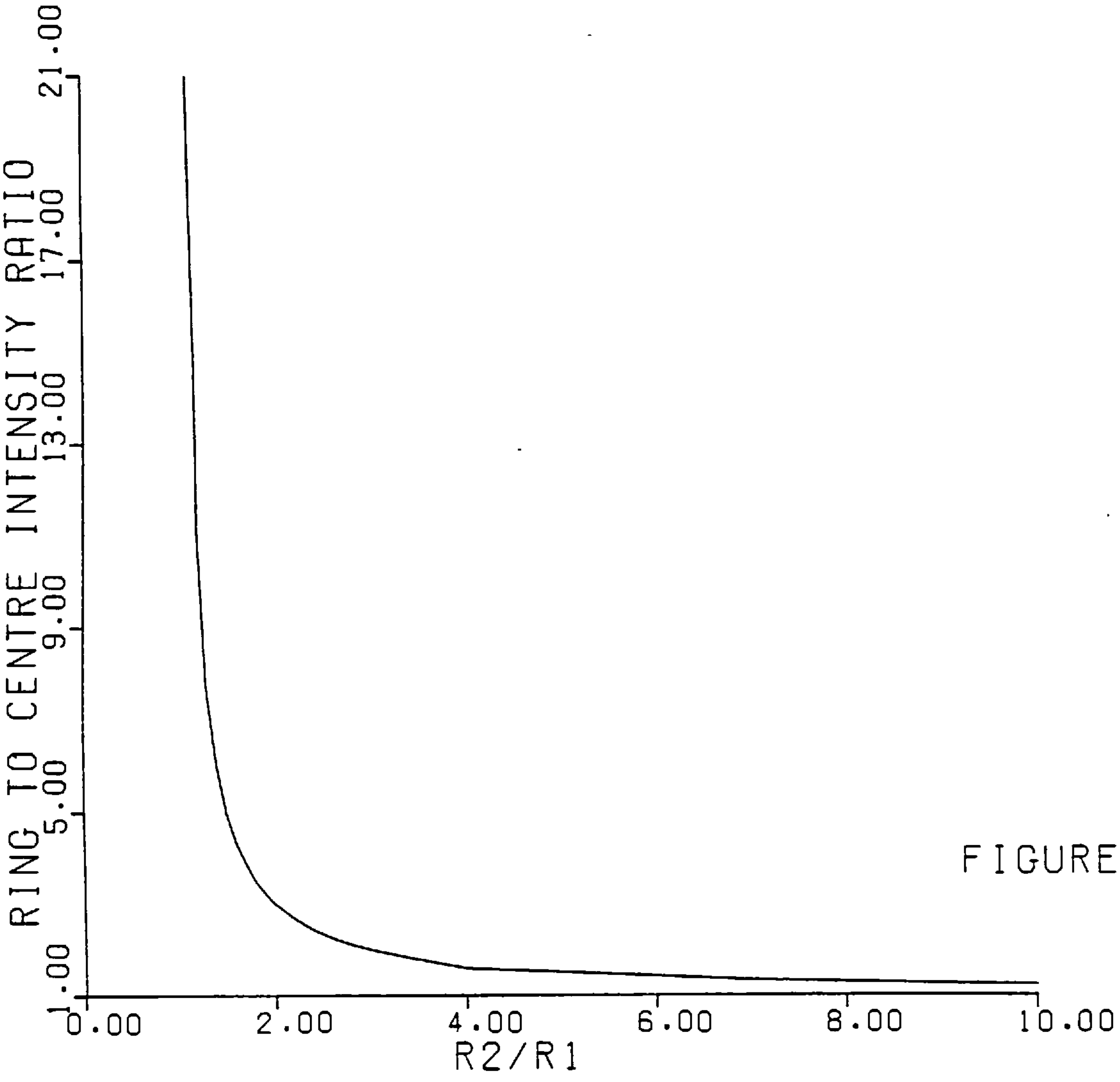

VARIATION OF PEAK RING TO CENTRAL INTENSITIES

FIGURE A.2

Clearly almost any value of Imax/I(o), the ring to centre intensity ratio, may be achieved simply by choosing the correct value of n. However as Imax/I(o) increases, so the width of the ring decreases. Thus, for this model, very large ring to centre intensity ratios are accompanied by very thin shells.

For an ellipsoidal thin-shell model it is possible to derive the variation in line splitting as a function of the distance from the centre (Figure A.3). Assuming radial expansion the velocity splitting, S, is given by:

$$S = 2V = 2kR\cos\theta \qquad (A.4)$$

Now $y = R\cos\theta$ so

$$S = 2k(b^2-b^2d^2)^{\frac{1}{2}} \qquad (A.5)$$

where $d = {}^{x}/_{a}$

The value of this type of model lies largely in the way it illustrates the effects taking place in models of much greater complexity, where the tractability of the analysis is impractical and it becomes necessary to use numerical rather than analytical methods to compute the results.

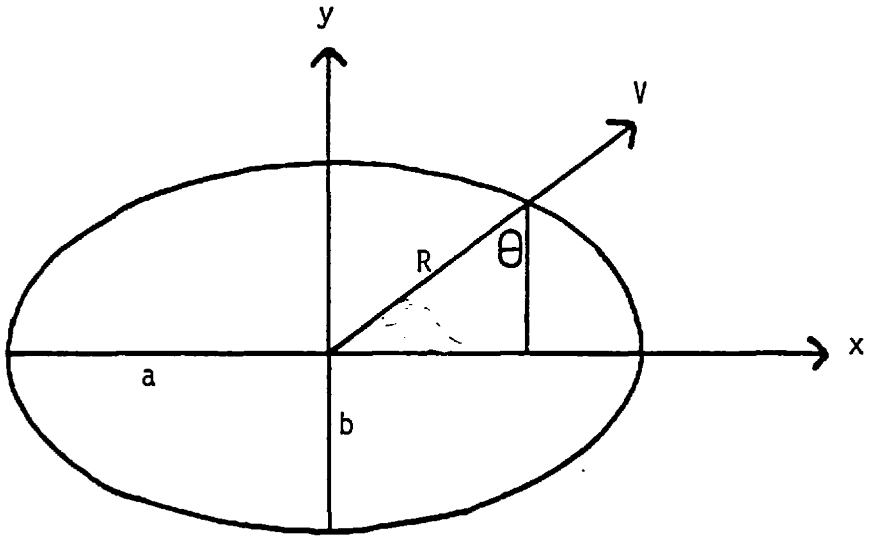

Figure A.3 Velocity Splitting for Ellipsoidal Model

In order to approximate observed nebulae using a model, some coherent theory of the evolution of the shell is required, from its formation and ejection through to its disappearance as it mixes with the interstellar medium. This theory must be capable of explaining the diversity of the observed forms of planetaries.

## A.3 Development of Nebular Shells

The mechanisms controlling the development of the nebular shells remain uncertain. Woyk (1968), Gurzadyan (1969) postulated internal magnetic fields to explain the observed structures. A tendency for the nebulae to be orientated non-randomly with respect to the galactic plane has been noted by Cudworth (1975), Melnick and Harwit (1975), and Grenin and Zvereva (1968), suggesting that the galactic magnetic field may influence the structure to some extent.

The development of shells under the influence of a continuous accelerative process was considered by Kirkpatrick (1976) who found that an initially oblate spheroidal stellar atmosphere could develop into a prolate spheroid.

Louise (1973) has discussed the combined influence of stellar rotation and gravity on a shell ejected from a spherical star. Phillips and Reay (1977) have extended this approach, considering the effects of radiation pressure, differential rotation and gravitational braking on the development of a shell ejected from an oblate star. In this model three separate ways of defining the mode of ejection were used.

1) Model A: Instantaneous ejection of the shell at a range of velocities. Density $\rho_t \; \alpha \; {}^1/_{r^2}$

2) Model B: Gradual ejection at a unique velocity $\rho_t \alpha \; {}^1/_{r^3}$

3) Model C: Instantaneous ejection at a unique velocity and constant density.

These three cases represent wide extremes, but it is not clear that any can be excluded.

The radial component of the nebular acceleration for a segment of nebular shell dr, subtending a solid angle $d\Omega$ at a distance $r(\beta)$ from the star, may be written as:

$$\left.\begin{aligned} \frac{md^2r(\beta)}{dt^2} \;=\; & -\frac{G.mM_*F(\beta)}{r^3(\beta)} \\ & + L_*d\Omega.F(\beta)(1-\exp(-\zeta(\beta))\;) \\ & - d\Omega\left[\nabla(P_G+P_R).F\right]F.dr \end{aligned}\right] \tag{A.10}$$

Where $M_*$, $L_*$ are the stellar mass and luminosity

$\beta$ is the angle between the stellar equatorial plane and the radius vector

$\zeta(\beta)$ is the optical depth of the shell

$P_G \; \alpha \; P_R$ are respectively the gas and the Lyman $\alpha$ photon pressures

The first term of the equation represents the gravitational braking, the second term the Lyman continuum radiation pressure, and the third term is responsible for the non-radial redistribution of the nebular material, although its actual contribution is not well understood.

Neglecting the last two terms it can be shown that the axial ratio of the terminal nebular shell (equatorial major axis/ equatorial minor axis) is given by:

$$\alpha^2 = \frac{1+2w^2R_*{}^2(o)}{V_o{}^2-V^2_{escape}} \qquad (A.11)$$

Where $V_{escape}$ is the polar escape velocity.

An interesting consequence of this model is a tendency for the mass to concentrate towards the minor axis. This effect becomes more pronounced as the rotational velocity of the star increases. Louise (1973) found a mass concentration towards the equatorial plane under the initial conditions that mass is uniformly emitted from a spherical star.

Using the model of Phillips and Reay a large range of nebular shapes can be generated. For $\alpha^2-1<1$ these are toroidal in form, as the mass emitted from the polar regions does not achieve escape velocity. If the differential rotation of the progenitor is taken into account then the subsequent nebular shells tend to be more elongated, but no substantial morphological changes are observed.

The nebular structures resulting from the different ejection processes considered earlier were found to be in close correspondence and, although the intensity levels vary in details, the overall shapes were insensitive to the model type.

The nebular shells generated by this model were contoured by computing the density at a number of points along the line of sight through the nebula. These densities were squared and summed to give the emission measure at that point, a matrix of such points being computed covering the nebula. This matrix was convolved with a seeing disc and contours of equal intensity were drawn. Strictly these contours are only comparable with radio maps, although they should be adequate for comparisons at Balmer wavelengths.

## A.4 Radiation Pressure

Following the evolution proposed by Härm and Schwarzschild (1975) for the central star, in the early stages its luminosity in the Lyman continuum is small and so the radiative acceleration is negligible. In the latter stages of the expansion of the nebula, when the central star has evolved to the point where the energy in the Lyman continuum is large, the nebular material is very tenuous and fully ionized, becoming increasingly transparent and tending to decrease the efficiency of the momentum transfer, until finally an asymptotic velocity is reached. It appears then that the shaping of the shell occurs mainly in the stellar gravitational field, radiative acceleration only becoming important in the later stages.

Observational studies (Weedman, 1968) and theoretical studies (Capriotti, 1973; Kahn, 1967) indicate that the nebular shell acquires its velocity of expansion over a period of time which is a significant fraction of the lifetime of the nebula.

## A.5 Synthetic Line Profiles

The model of Phillips and Reay has been used by the author to generate spectral line profiles which would be produced by a particular nebular model. The model was created in the computer on a three-dimensional grid of 100 x 100 x 100 points, the equator of the model lying in the Z-X plane and the spin-axis of the progenitor lying along the Y-axis (Figure A.4).

The dimensions and position of the entrance aperture on the model nebula was defined by the x,y coordinates of the intersection of the line of sight with the x-y plane, whilst the orientation of the nebula was described by the angles $\gamma$ and $\phi$, shown in figure A.4.

The velocity of expansion of the nebula at any point was assumed to vary in direct proportion to the radius and the corresponding Doppler shift was calculated.

At each point along the line of sight the density, and hence the intensity of the emission, and the radius and hence the expansion velocity and corresponding Doppler shift was computed. In this manner the structural line profile could be evaluated. This profile was then convolved with a Gaussian to simulate the effects of instrumental and thermal broadening.

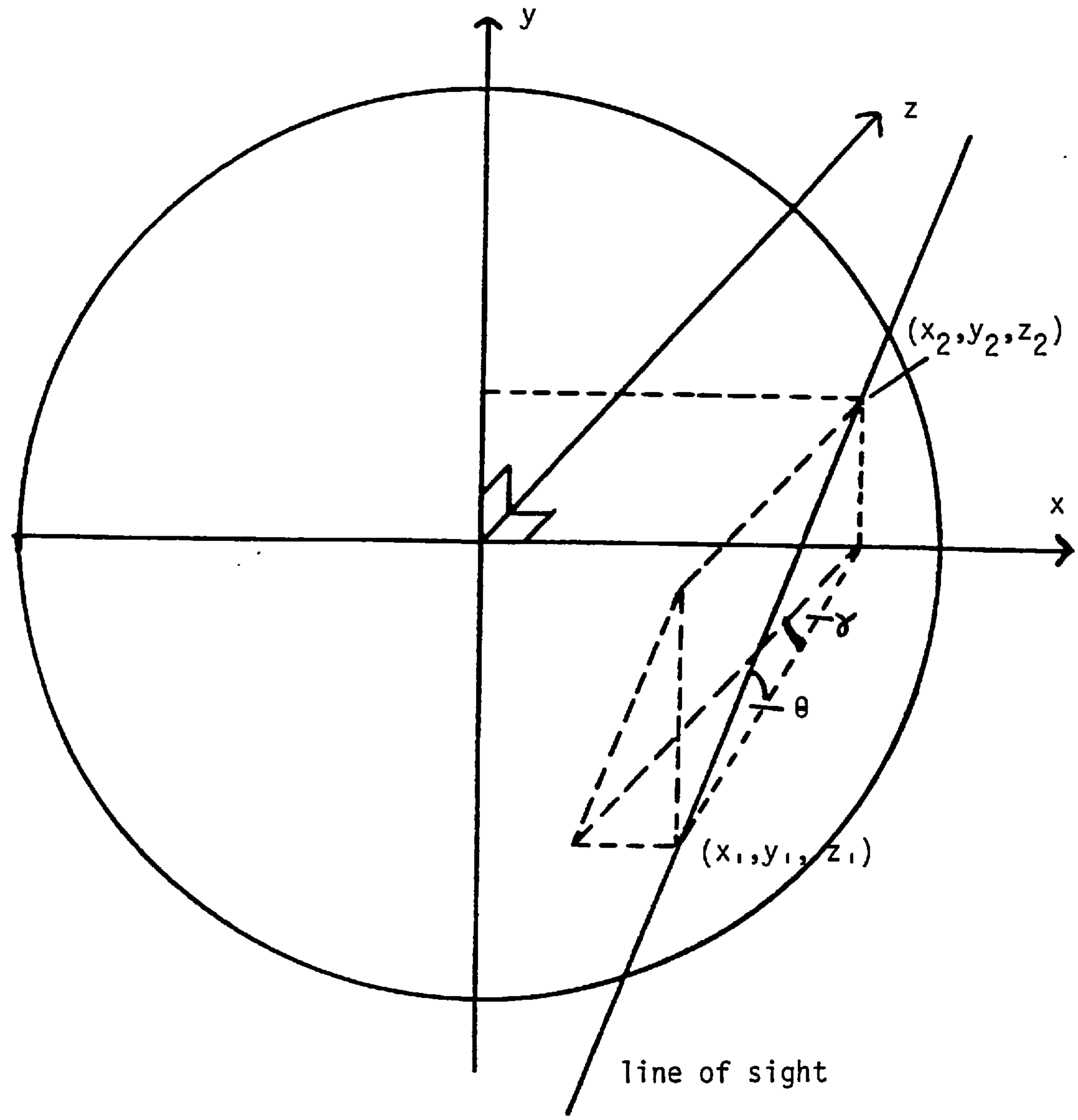

Figure A.4

A profile fairly typical of the kind produced by this program is shown in Figure A.5, both before and after this convolution. The assymmetric shape of this profile is characteristic of this model, the sharp cut offs representing the boundaries to the shell and the relative widths of the components being determined by the angle of the nebula to the line of sight. Clearly if this is an accurate representation of the actual situation, then it is not possible to interpret the observed profiles using symmetrical functions, such as Gaussians.

This work is now being extended by Mr G Robinson as part of a larger programme involving the correlation of radio, infra-red, spectroscopic and electronographic data, in the production of a realistic model.

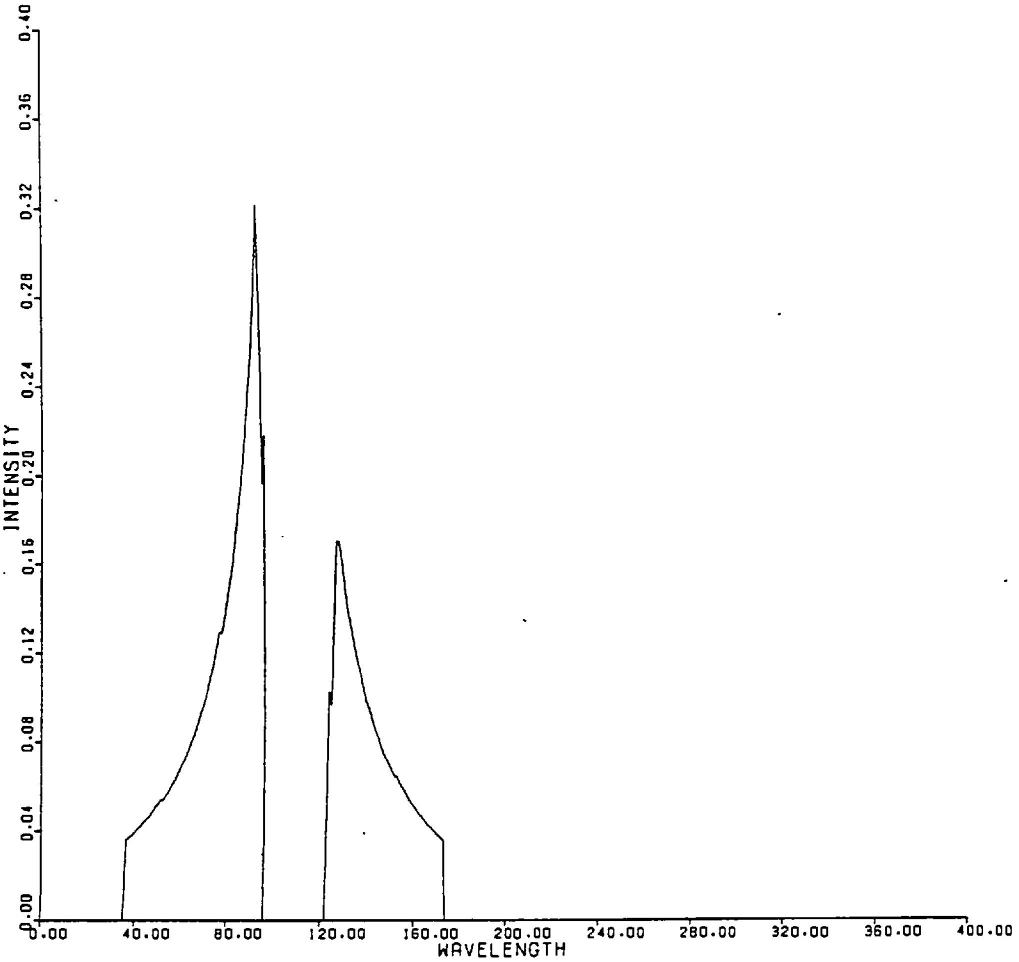
0.40
0.36
0.32
0.28
0.24
0.20
0.16
0.12
0.08
0.04
0.00
INTENSITY
0.00
40.00
80.00
120.00
160.00
200.00
240.00
280.00
320.00
360.00
400.00
WAVELENGTH

Figure A.5

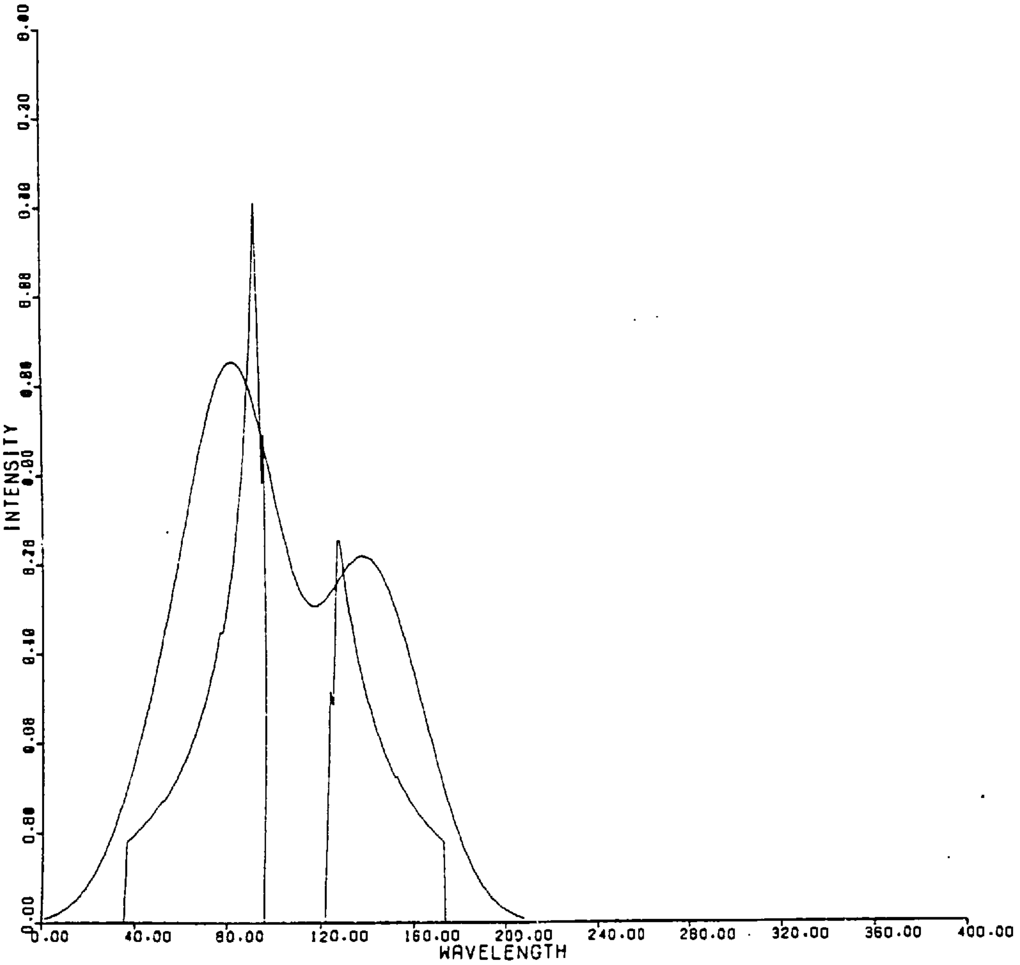
0.00
0.30
0.30
0.88
0.80
0.00
0.28
0.10
0.08
0.80
0.00
INTENSITY
0.00
40.00
80.00
120.00
160.00
200.00
240.00
280.00
320.00
360.00
400.00
WAVELENGTH

## REFERENCES

Aller, L.H., Epps, H.W., Czyzack, S.J., 1976 Ap.J., 205, 798

Aller, L.H., Walker, M.F., 1970, Ap.J., 171, 917

Audier, M., Boutot, J.P., 1975, Phillips Res. Repts. 30, 226

Balick, B., Bignell, C., Terzion, Y., 1973, Ap.J. 182 417

Bates, B., Bradley, D.J., Kohno, T., Yates, H.W., 1966, J.Sci.Instrum. 41, 514

Beaver, E.A., Mcilwain, C.E., 1971, Rev.Sci.Instrum., 42, 1321

Becklin, E.E., Neugebauer, G., Wynn-Williams, C.G., 1973 Astrophys.Letters, 15, 87.

Bell, D.A., 1960, Electron Technology, Sept 342

Bevington, P.R. 1969, Data Reduction and Error Analysis for the Physical Sciences, McGraw Hill, P. 237

Boeshaar, G.O. 1974, Ap.J. 187, 283

Bohuski, T., Smith, M.G., 1974, Ap.J., 193, 197

Bowen, I.S., 1927, Physical Review, 29, 231

Bowen, I.S, 1928, Ap.J. 67, 1

Brown, R.L., Mathews, W.G., 1970, Ap.J., 160, 939

Burgess, A., 1964, Mem. R.A.S. 69, 1

Cahn, J.H., Kaler, J.B., 1971, Ap.J. Supp 22, 319

Campbell, 1894, Astron. and Astrophys., 13, 384

Campbell, Moore, 1918, Pub.Lick.Obs. 13, 384

Capriotti, E.R., 1973, Ap.J. 179, 495

Chabbal, R., 1958, J.Phys.Rad. 19, 295

Courtes, G., Fehnenbach, C., Hughes, E., Romard, J., 1966, Appl.Opt 5. 1349

Crede, C.E., 1951, Vibration and Shock Isolation, Chapman and Hall, London.

Cudworth, K., 1975, M.N.R.A.S., 172, 57p

Curtis, H., 1918, Pub.Lick.Obs. 13,55

Dopita, M., Gibbons, A., 1975, M.N.R.A.S., 171, 73

Duncan, 1937, Ap.J., 86, 496

Eissner, W., Martins, P. de A.P., Nussbaumer, H. Saraph H.E., Seaton, M.J., 1969, M.N.R.A.S. 146, 63

Elliott, K.H., Meaburn, J., 1975, Ast. & Space Science, 35, 81

Faulkner, D.J., 1970, Ap.J., 162, 513

Feibelman, W.J., 1970, R.A.S.C. Jour., 64, 305

Finzi, A., Wolf, R., 1970, Astrophys. Letters 5, 63

Flower, D.R., 1969, M.N.R.A.S. 146, 171

Geake, J.E., Ring, J., Woolf, N.J., 1959, M.N.R.A.S., 119, 616

Gillett, F.C., Low, F.J., Stein, W.A., 1967, Ap.J. 149, L97

Grinin, V.P., Zvereva, A.M., 1968 IAU Symposium No 34 "Planetary Nebulae" p 287

Gull, T.R. 1977, IAU Symposium No 76 "Planetary Nebulae"

Gurzadyan, G.A., 1970, "Planetary Nebulae" Reidel Publishing Co, Dordrecht

Harm, R., Schwarzschild, M., 1975, Ap.J. 200, 324

Heavens, O.S., Ring, J., Smith, S.D., 1957, Spectrochimica Acta, 10, 179

Hicks, T.R., Reay, N.K., Scaddan, R.J., 1974(a), J.Sci.Inst 7, 27

Hicks, T.R., 1974(b) Ph.D. Thesis, University of London

Hicks, T.R., Phillips, J.P., Reay, N.K., 1976, M.N.R.A.S. 176, 409

Hicks, T.R., 1978, Private Communication

Hindle, P.H., Reay, N.K., 1967, J.Sci.Instrum., 44, 360

Hromov, G.S., Kohoutek, L., 1968, B.A.C., 19, 1

Hua, C.T., Louise, R., 1972, Astr.and Astrophys., 21, 193

Huggins, 1864, Phil.Trans.Rog.Soc. 154, 437

Hummer, D., 1965, Mem. R.A.S. 70, 1

Hunter, J.H., Sofia, S., 1971, M.N.R.A.S., 154, 393

Jacquinot, P., 1954, J.Opt.Soc.Am., 44, 761

Jones, R.V., Richards, J.C.S., 1973, J.Sci.Instrum. 6, 589

Kahn, R.D., 1967

Kirkpatrick, R.C., 1976, Astrophys.Letters, 17, 7

Krishna Swamy and O'Dell, 1968, Ap.J., 151, L61

Krishna Swamy and Stecker, 1969, Pub.A.S.P., 81, 873

Kutter, G.S., Sparks, W.M., 1974, Ap.J. 192, 447

Lallemand, A., 1966, A.E.E.P., 22A, 1

Lampton, M., Paresce, F., 1974, Rev.Sci.Instrum. 45, 1098

Liller, M.H., Welther, Liller, W., 1966, Ap.J., 144, 280

Liller, M.H., Liller, W., 1968, IAU Symposium No 34. "Planetary Nebulae" P 38

Lockyer, N., 1894, Phil.Trans.Roy.Soc. 186A, 73

Louise, R., 1973, Mem.Soc.Roy.Liege, 5, 465

Louise, R., 1974, Astr. and Astrophys., 30, 189

Lucy, L.B., 1967, Ast.J., 72, 813

Mathews, W.G., 1966, Ap.J., 143, 173

Mayer, M.G., 1931, Ann.D.Phys. 9, 273

McCord, T.B., Westphal, J.A., 1972, Applied Optics, 11, 552

McGee, J.D., Bacik, H., Coleman, C.I., Morgan, B.L., 1972, A.E.E.P., 33A, 13

McMullan, D., Powell, J.R., Curtis, N.A., 1972, A.E.E.P., 33A, 37

Meaburn, J., 1968, Astrophys.Space Sci., 2, 115

Meaburn, J., 1975, Astrophys.Space Sci., 36, 489.

Melnick, G., Harwit, M., 1975, M.N.R.A.S., 171, 441

Melnick, G., 1977, Private Communication

Menzel, D.H., Aller, L.H., Hebb, M.H., 1941, Ap.J. 93, 230

Menzel, D., 1946, Physica, 12, 768

Miller, J.S., Mathews, W.G., 1972, Ap.J., 172, 593

Miller, J.S., 1974, Ann.Rev.Astron and Astrophys

Minkowski, R., Osterbrock, D.E., 1960, Ap.J. 131, 537

Minkowski, R., 1968, Astr.J. 73, 842

Mufson, S.L., Lyon, J., Marionni, P.A., 1975, Ap.J., 201, L85

Munch, G., 1968, IAU Symposium No 34 "Planetary Nebulae" 259

Nyquist, 1928, Trans.Am.Inst.Elec.Eng. 47, No 2, P.617.

O'Dell, C.R., 1962, Ap.J., 135, 371

Osterbrock, D.E., 1960, Ap.J. 131. 541

Osterbrock, D.E., 1974, Pub.A.S.P. 86, 609

Osterbrock, D.E., 1974, Astrophysics of Gaseous Nebulae, p 28, W.H. Freeman, San Francisco.

Pacynski, B., Ziolkowski, J., 1968, IAU Symposium No 34 "Planetary Nebulae", 396

Pequinot, D., 1977, Preprint

Perek, L., Kohoutek, L., 1967 "Catalogue of Galactic Planetary Nebulae", Czechoslovak Academy of Sciences

Phillips, J.P., Reay, N.K., 1977, Astron. and Astrophys., 59. 91

Proisy, P.E., 1974, Astron.and Astrophys., 35, 71

Ramsay, J.V., 1962, App.Opt.1, 411

Reay, N.K., Ring, J., Scaddon, R.J., 1974, J.Sci.Inst. 7, 673

Reay, N.K., Warswick, S.P., 1977, M.N.R.A.S., 179, 317

Reay, N.K., Warswick, S.P., 1978, In Preparation

Rose, W.K., 1968, IAU Symposium No 34 "Planetary Nebulae" 390.

Roxburgh, I.W., 1967, Nature, 215, 838

Scott, P.F., 1973, M.N.R.A.S. 161. 35P

Scott, P.F., 1976, M.N.R.A.S. 175, 371

Seaton, M.J., 1960, Rep.Progress in Phys. 23, 313

Smartt, R.N., Ramsey, J.V., 1964, J.Sci.Instrum. 41, 514

Smith, S.D., Heavens, O.S., 1957, J.Sci.Instrum. 34, 492

Smith, W., Weedman, D.W., 1970, Ap.J. 160, 65

Smith, R.L., Rose, W.K., 1972, Ap.J., 176, 395

Smith, W.J., Bonn, J., Cochran, W.D., Gelfond, J., 1976 App.Opt. 15, 717

Spitzer, L., Greenstein, J., 1951, Ap.J., 114, 407

Stromgren, B., 1939, Ap.J., 89, 526

Taylor, K., 1974, Ast.and Space Science, 26, 327

Thackeray, A.P., Evans, D.S., 1950, M.N.R.A.S., 10, 429

Thompson, A.R., Colvin, R.S., 1970, Ap.J., 160, 363

Timothy, J.G., Bybee, R.L., 1975, Rev.Sci.Instrum 46, 1615

Timothy, J.G., 1976, IAU Colloquum No 40, "Applications astronomique desrecepteurs d'images a reponse lineaire" Paris

Torres-Peimbert, S., Peimbert, M., 1977, Preprint

Vernitron, Thornhill, Southampton, 1978, Private Communication

Vorontzov-Velyominov, B.A., 1934, Astron.J. (USSR) 11, 40

Weedman, D.W., 1968, Ap.J., 153, 49

Westerlund, B.E., Henize, K.G., 1967, Ap.J. Supp. XIV, 154

Williams, R.E., 1970, Ap.J., 159, 829

Wilson, O.C., 1946, Pub A.S.P., 210

Wilson, O.C., 1950, Ap.J., 111, 279

Wilson, O.C., 1958, Rev.Mod.Phys., 30, 1025

Woyk, E., 1968, IAU Symposium No 34 "Planetary Nebulae" p 275

Wright, 1918, Lick Obs.Pub., 13, 193

Wynn-Williams, C.G., 1970, Ap.J.Letters, 6, 189